

Supplementary Information

A ‘through-DNA’ mechanism for co-regulation of metal uptake and efflux

5 Udit Kumar Chakraborty[†], Youngchan Park[†], Kushal Sengupta, Won Jung, Chandra P. Joshi,
Danielle H. Francis, Peng Chen^{*}

Corresponding author: pc252@cornell.edu

10

Supplementary Information

Supplementary Methods

Supplementary Notes 1 to 11

Supplementary Figs. 1 to 36

15

Supplementary Tables 1 to 9

Supplementary References 1 to 92

Table of Contents

	1	Supplementary Methods	3
	1.1	Construction of strains and plasmids for live cell studies.....	3
5	1.2	Live cell imaging sample preparation, method and data processing for single-molecule imaging, tracking, and protein quantification experimental procedure	7
	1.3	Construction of strains, protein purification, DNA labeling, sample preparation, imaging and data analysis for in vitro smFRET studies	14
		Supplementary Notes	
10	1	Genome sequence analysis and identification of potential recognition sequences of metal efflux regulators (e.g., ZntR) at promoters that are regulated by metal uptake regulators (e.g., Zur), or vice versa, in E. coli, other bacteria, and yeast	18
	1.1	Potential partial ZntR recognition sequences around known Zur boxes in E. coli and other bacteria	18
15	1.2	Aside from the Zur-ZntR Zn uptake-efflux regulator pair, potential Zn efflux regulator recognition sequences are also found at promoters controlled by Zn uptake regulators of other families in bacteria	19
	1.3	This pattern of potential existence of partial efflux regulator recognition sequences around known uptake regulator binding box was also observed for regulator pairs involved in the homeostasis of other metals beyond Zn (for example: Fe and Ni) in bacteria.....	19
20	1.4	Oppositely, uptake regulator recognition sequence is also found around known efflux regulator binding box in bacteria.....	19
	1.5	In yeast, a similar pattern of efflux regulator recognition sequence overlapping with known uptake regulator binding motifs can be found for iron homeostasis.....	20
25	2	Functionality and intactness of sfGFP-tagged ZntR in E. coli cells	22
	2.1	Western blot shows the intactness of ZntR-sfGFP fusion proteins.....	22
	2.2	Ensemble fluorescence measurements show that the sfGFP-tagged ZntR is fluorescent.....	23
	3	Analysis of resolvable diffusion states of Zur in the cell and extraction of their effective diffusion coefficients (D) and fractional populations (A)	24
30	3.1	The resolved three diffusion states of Zur in the cell were assigned as FD, NB, or TB based on their diffusion coefficients and rationales.....	24
	3.2	The fractional populations of Zur's three diffusion states show expected dependence on cellular [Zur]	28
	3.3	Bootstrap analysis shows statistical reliability of data.....	28
35	4	Extraction of kinetic and thermodynamic parameters for Zur-DNA interactions in cells	29
	4.1	Extraction of k_{-1} , the apparent unbinding rate constant from the tight binding state	29
	4.2	Extraction and summary of additional kinetics and thermodynamic parameters.....	31
	5	ZntR_{C115S} mutant has severely diminished Zn²⁺ binding affinity (lower than 10⁻⁷ M affinity), 8 orders of magnitude weaker than wild-type ZntR (~10¹⁵ M)	33
40	6	Protein labeling design for single-molecule FRET measurements in vitro	34
	6.1	Selecting locations for fluorescent probe location on Zur based on Zur structure.....	34
	6.2	Prediction of E _{FRET} values based on Zur-DNA complex structure.....	35
	7	Procedures for Gaussian fitting to extract E_{FRET} values from the E_{FRET} histograms	38
45	8	ZntR_{apo} preferentially disrupts Zur_{Zn} binding at the dyad proximal to the Cy3 labeling position on DNA	39
	9	Summary of kinetic parameters for Zur^{Cy5}-31-bp DNA^{Cy3} interactions measured by in vitro smFRET	42
	10	A through-DNA mechanism for Zur-DNA-ZntR_{apo} interactions and kinetic derivations	42
50	10.1	Empirical kinetic equation for ZntR _{apo} -induced enhancement of Zur's facilitated unbinding and diminishment of Zur's impeded unbinding	43
	10.2	Kinetic derivation and justification of the mechanistic model for ZntR _{apo} -dependent Zur unbinding from DNA.....	44
	11	Additional data and figures	47

1 Supplementary Methods

1.1 Construction of strains and plasmids for live cell studies

For all cloning and gene editing, the PCRs were performed using the AccuPrime Pfx DNA Polymerase Kit. The primers and enzymes were purchased from the Integrated DNA Technologies and New England Biolabs, respectively. PCR amplifications and digestion products were recovered using the Wizard SV Gel and PCR Clean-Up System (Promega). Plasmid extractions were performed using the QIAprep Spin Miniprep Kit (Qiagen). All primers, plasmids, and strains used are listed in Supplementary Table 1, Table 2 and Table 3 respectively.

1.1.1 Making electrocompetent cells for plasmid transformation or linear DNA homologous recombination

Transformation of plasmids and linear DNA inserts into *Escherichia coli* BW25113 (CGSC# 7739 Keio Collection, Yale; genotype: (F- Δ (*araD-araB*)567, Δ *lacZ*4787(::rrnB-3), λ -, *rph-1*, Δ (*rhaD-rhaB*)568, *hsdR514*) cells was performed via electroporation. Electrocompetent *E. coli* cells were prepared in the SOB media [2% w/v Bacto Tryptone (Sigma-Aldrich, cat. #: T9410), 0.5 % w/v Bacto Yeast Extract (Sigma-Aldrich, cat. #: Y1625), 10 mM NaCl (Macron, 7581-12), 2.5 mM KCl (Fisher Scientific, P217-500), 10 mM MgCl₂ (Mallinckrodt, 5958-04), and 10 mM MgSO₄ (Fisher Scientific, M63-500) in nanopure sterile water] containing appropriate antibiotics [ampicillin (100 μ g/mL), chloramphenicol (25 μ g/mL), or kanamycin (30 μ g/mL); USBiological]. In case of homologous recombination, an ampicillin resistant and temperature sensitive pSLTS plasmid was also introduced in the *E. coli* cells. 20 mM L-arabinose (SigmaAldrich, cat. #: A3256), which is a reagent that can induces the expression of the *bet*, *gam*, and *exo* λ -Red enzymes encoded in pSLTS for DNA homologous recombination¹, was used for culturing. The cells were centrifuged and washed twice with cold 10% glycerol (Macron, 5092-02) in nanopure water. The linear DNA inserts or plasmids were then electroporated (2.5 kV or 1.8 kV, using MicroPulser Electroporator; cat.#: 1652100, Bio-Rad) into the prepared electrocompetent cells, and then recovered in SOC medium [SOB medium + 20 mM glucose (Sigma-Aldrich, cat. #: G7528)]. After 4 hours incubation, the cells were plated onto LB-agar containing appropriate antibiotics and further incubated for 18 hours.

Chromosomal DNA insertions and plasmid transformations were verified by colony PCR screening using the Econo Taq DNA Polymerase Kit (Lucigen) and gene sequencing. The temperature sensitive pSLTS plasmid was removed by incubation at 42 °C for 18 hours after successful homologous recombinations and verified by ampicillin selection.

1.1.2 Construction of the chromosomal Δ *zur* deletion strain

λ -Red homologous recombination was used to derive the Δ *zur* (DZ; Supplementary Table 3) strain from *Escherichia coli* BW25113. A linear DNA insert targeting the *zur* gene in the chromosome was made using primers H1H2DZurPT2SK-fp and DZurH1H2PT2SK-rp (Supplementary Table 1) together with a template containing a kanamycin resistance gene cassette containing an I-SecI recognition site, for subsequent RecA recombination, obtained from the pT2SK plasmid¹. The linear insert was introduced via electroporation into the electrocompetent BW25113 strain bearing a temperature sensitive pSLTS plasmid. The cells were recovered in 1 mL SOC medium, incubated at 30 °C and shaking at 250 rpm for 4 hours, and finally plated onto LB-agar plate containing both ampicillin (50 μ g/mL) and kanamycin (15 μ g/mL), resulting in the DZ strain (Supplementary Table 3). Deletions were further confirmed by colony PCR.

1.1.3 Construction of chromosomal *zur*^{mE} Δ *zntR* strain

λ -Red homologous recombination was used to derive the *zur*^{mE} Δ *zntR* (Zur^{mE}-DZR; Supplementary Table 3) strain from the *zur*^{mE} strain². A linear DNA insert targeting the *zntR* gene in the chromosome was made using primers H1H2DZnrPT2SK-fp and DZnrH1H2PT2SK-rp (Supplementary Table 1) together with a template containing a kanamycin resistance gene cassette containing an I-SecI recognition site, for subsequent RecA recombination, obtained from the pT2SK plasmid¹. The linear insert was introduced via

electroporation into the electrocompetent *zur^{mE}* strain bearing a temperature sensitive pSLTS plasmid. The cells were recovered in 1 mL SOC medium, incubated at 30 °C and shaking at 250 rpm for 4 hours, and finally plated onto LB-agar plate containing ampicillin (10 µg/mL), chloramphenicol (10 µg/mL) and kanamycin (15 µg/mL), resulting in the *Zur^{mE}-DZR* strain (Supplementary Table 3). Deletions were further confirmed by colony PCR.

1.1.4 Construction of chromosomal *ΔzurΔzntR* double deletion strain

The *ΔzurΔzntR* strain was derived from the DZ strain (Supplementary Table 3). First the kanamycin resistance cassette at the erstwhile *zur* locus in DZ was eliminated via RecA recombination. To induce I-SceI enzyme cleavage mediated scar-less elimination of the kanamycin resistance cassette, a sample of DZ overnight culture was diluted 1:50 in 10x PBS buffer; 200 µL was plated onto LB-agar plate containing anhydrotetracycline (aTc) (150 ng/mL; Acros Organics). To confirm the elimination of the kanamycin resistance cassette in the genome, 8 colonies from the aTc plate were tested for kanamycin sensitivity on LB-agar plate containing kanamycin (30 µg/mL). Cells from colonies that had kanamycin-sensitive phenotypes were chosen for DNA sequencing to confirm the presence of the desired genomic edit. A linear DNA insert targeting the *zntR* gene in the chromosome was made using primers H1H2DZntRPT2SK-fp and DZntRH1H2PT2SK-rp (Supplementary Table 1) together with a template containing a kanamycin resistant cassette. Subsequent steps for homologous recombination and deletion of the *zntR* gene were followed according to procedures described above. The pSLTS plasmid was removed from the strains by culturing the cells at 42 °C overnight. The strain thus obtained, DZ-DZR (Supplementary Table 3), lacked both *zur* and *zntR* genes.

1.1.5 Construction of the chromosomal *zntR_{C115S}* mutant strain

To introduce the C115S mutation into *zntR* gene in the chromosome of the *Escherichia coli* BW25113 strain, the *zntR_{C115S}* gene was first cloned out of the plasmid pBZR(C115S)-mEos3.2³ using primers H1-ZntRC115S-fp and ZntR_KAN start_rp, while the KAN gene cloned out of the pT2SK plasmid¹ was amplified using primers KAN-fp and KAN-H2 rp (Supplementary Table 1). Overlapping PCR was used to design the *zntR_{C115S}:kan* linear DNA insert using the H1-ZntRC115S-fp and KAN-H2 rp primer pairs along with the *zntR_{C115S}* and KAN genes as template to target the *zntR* gene in the chromosome. This linear insert was introduced via electroporation and following λ-Red homologous recombination procedure described above, the ZRC115S strain carrying *zntR_{C115S}* in the chromosome (Supplementary Table 3) was obtained.

1.1.6 Construction of the chromosomal *ΔzntR zinT^G*, *zntR_{C115S} zinT^G*, and *zinT^G* mutant strains

To image ZinT expression in the cell, we tagged chromosomal *zinT* gene with super-folder GFP at the C-terminal. First, a linear *sfGFP:cat* DNA insert targeting the C-terminal of the *zinT* gene was obtained by overlapping the *sfGFP* gene, cloned from the sfGFP-pBAD plasmid⁴ using primers GFP_fp and sfGFP_cam_rp, with the *cat* gene, obtained from the pUCmEos3.2:cat³ plasmid using sfGFP_cam_fp and H2zinT-sfGFP-cam-rp primer pairs (Supplementary Table 1). The H1zinT-sfGFP-cam-fp and H2zinT-sfGFP-cam-rp primer pair was used for the overlapping PCR. The obtained linear DNA was introduced into the *Escherichia coli* JW3254-5, ZRC115S, and BW25113 strains (Supplementary Table 3) via electroporation and following procedures for homologous recombination described above, we obtained the DZR-ZINTG, ZRC115S-ZINTG, and ZINTG, respectively, carrying *ΔzntR zinT^G*, *zntR_{C115S} (i.e., zntR_{apo}) zinT^G*, and *zinT^G* genomic features in the chromosome, respectively (Supplementary Table 3).

1.1.7 Construction of *zntR_{C115S}^G* and *zntR^G* in *L-arabinose* inducible pBAD plasmids

To spectrally separate Zur and ZntR in the cells, we tagged *zntR* and *zntR_{C115S}* with super-folder GFP. To make the pBAD33 (chloramphenicol resistant) plasmid expressing *zntR_{C115S}-sfGFP*, the *zntR_{C115S}* gene was first cloned out of the plasmid pBZR(C115S)-mEos3.2³ using primers Sac1-EZntR-pB33-fp and ZntR_GFP_rp. The *sfGFP* gene was cloned from the sfGFP-pBAD plasmid⁴ using primers

GFP_{fp} and sf-GFP_{rp}. We used overlapping PCR with primer pairs SacI-EZntR-pB33-fp and sf-GFP_{rp}-pst1 to tag the *zntR*_{C115S} gene with *sfGFP*. After PCR amplification using AccuprimePfx DNA Polymerase, the linear *zntR*_{C115S}-*sfGFP* product was digested with SacI-HF and PstI-HF restriction enzymes and inserted into a similarly digested pBAD33 plasmid using quick ligase enzyme to generate the p33ZRG(C115S) plasmid. Another plasmid p24ZRG(C115S) was constructed using the pBAD24 vector backbone bearing the same gene insert for differential antibiotic selections. Next the *zntR* gene was copied out of the pBZntR-mEos3.2 plasmid³ using primers SacI-EZntR-pB33-fp and ZntR_GFP_{rp}. The linear *zntR*-*sfGFP* product was again obtained by overlapping PCR using primers zntRsfGFP_SacI_Gib_{fp} and zntRsfGFP_SacI_Gib_{rp} and was digested with SacI-HF enzyme and inserted into a digested pBAD33 plasmid using Gibson Assembly Mastermix (New England Biolabs) to generate the p33ZRG plasmid. The plasmids p24ZRG(C115S), p33ZRG(C115S) and p33ZRG (Supplementary Table 2) were then each transformed into *E. coli* 10G chemically competent cells for propagation and miniprep. The constructs were subsequently confirmed by colony PCR and DNA sequencing.

Another version of the Zur^{mE}-DZR strain, where the *zur-mEos3.2* gene was encoded in a plasmid rather than in the chromosome, was also constructed, DZ-DZR-pZmE, via the electroporation of the pZur_{mE} plasmid into the DZ-DZR strain. Electroporation of the plasmid pApoZur_{mE} in the DZ-DZR strain led to the construction of a DZ-DZR-pZmEC88S strain. Subsequently, the p33ZRG(C115S) plasmid was transformed into the DZ-DZR, DZ-DZR-pZmE and DZ-DZR-pZmEC88S strains resulting in the DZ-DZR-pZRG(C115S), DZ-DZR-pZmE-pZRG(C115S) and DZ-DZR-pZmEC88S-pZRG(C115S) strains. The p33ZRG plasmid was transformed into DZ-DZR-pZmE, resulting in the DZ-DZR-pZmE-ZRG strain. The p24ZRG(C115S) plasmid was transformed into Zur^{mE}-DZR, resulting in the DZR-Zur^{mE}-pZRG(C115S) strain (Supplementary Table 3).

Supplementary Table 1 | List of primers used in this study.

Primer Name	Sequence (5'-3')
1. SacI EZntR-pB33-fp	AATTCGAGCTCAGGAGGAATTCACCATGTATCGCATTGGTGAGCT
2. PstI EZntR-pB33-rp	TGCTGCAGTTATTATCATCATCATCTTTATAATCAGGACGACAACCACTCTTAACGCC
3. EcoRI – EzntR-fp	GGA GGAATT CACCATGTATCGCATTGGTGAGCT
4. ZntR_GFP _{rp}	TCCTCGCCCTTGCTCACCATACAACCACTCTTAACGCCAC
5. GFP _{fp}	ATGGTGAGCAAGGGCGAGGA
6. sf-GFP _{rp}	CTTGACAGCTCGTCCATGCC
7. sf-GFP _{rp} -pst1	GCATGCCTGCAGTTACTTGTACAGCTCGTCCA
8. zntRsfGFP_SacI_Gib _{fp}	TGGGCTAGCGAATTCGAGCTAGGAGGAATTCACCATGTATC
9. zntRsfGFP_SacI_Gib _{rp}	GGATCCCCGGGTACCGAGCTTTACTTGTACAGCTCGTC
10. H1H2DZntRPT2SK-fp	ATCAACGATAACTAGTGGAGTATGTTTTTTTGCCTGGCAATCTCAAGAGTGGCAGC
11. DZntRH1H2PT2SK- rp	AGTGTAATCCTGCCAGTGCAAAAAAACATACTCCACTAGTTTACGCCCCGCCTGC
12. H1H2DZurPT2SK- fp	CTAACCCCCACTTTGAGGTGCCCGGAGGGCGTACATCCTATCTCAAGAGTGGCAGC
13. DZurH1H2PT2SK- rp	GACGTGTACAAGGATGTACGCCCTCCGGGCACCTCAAAGTTTACGCCCCGCCTGC
14. znuC220 _{up}	CAGAAGCTGTATCTCGACACC
15. znuC297 _{dn}	TTCTTTATGTGTACCAGGGCG
16. pET_T7 _{fp}	TACGACTCACTATAGGGG
17. pET _{down} _{rp}	CCAAGGGGTTATGCTAGT
18. C17S _{fd}	GCAGGCTGAAAAAATCAGCGCGCAGCGTAATGTGC
19. C17S _{rc}	GCACATTACGCTGCGCGCTGATTTTTTTCAGCCTGC
20. C152S _{rc}	ACTGTTCAAGGATGACGACTCGCTTCCAATTCTACA
21. C152S _{fd}	TGTAGAAGTGGAAAGCGAGTCGTCATCCTGAACAGT
22. C113S _{fd}	CGCAGTGAAAGAAGAGAGTGCAGAAGGGCGTGGAAAG
23. C113S _{rc}	CTTCCACGCCCTTCTGCACTCTCTTCTTCTCACTGCG
24. C158S _{fd}	TCGTCATCCTGAACAGAGCCAGCATGATCACTCTG

25. C158S_rc	CAGAGTGATCATGCTGGCTCTGTTTCAGGATGACGA
26. EZurD49A-fp	ATGATCTGCTTGCTTTACTGCGCG
27. EZurD49A-rp	CGCGCAGTAAAGCAAGCAGATCAT
28. NdeI EZntR_fp_pET3a(5)	ATATACATATGTATCGCATTGGTGAGCTGGC
29. BamHI EZntR_rp_pET3a(5)	CAGCCGGATCCTTATTTATCATCATCATCTTTATAATCAGGACGACAACCACTCTTAACG
30. H1-ZntRC115S-fp	ACAAAATCAACGATAACTAGTGGAGTATGTATGTATCGCATTGG
31. ZntR_KAN start_rp	ACCGCTGCCACTCTTGAGATTCAACAACCACTCTT
32. KAN-fp	ATCTCAAGAGTGGCAGCGGTTCTGTTAAGTAACTGAACCC
33. KAN-H2 rp	AGTGTAACTCCTGCCAGTGCAAAAAATTACGCCCCGCC
34. sfGFP_cam_rp	CTTCGAAGCAGCTCCAGCCTACACTTACTTGTACAGCTCGTCCATGCC
35. sfGFP_cam_fp	GGCATGGACGAGCTGTACAAGTAAGTGTAGGCTGGAGCTGCTTCGAAG
36. H1zinT-sfGFP-cam-fp	GTTGAGTAGCGAAGAAGTGGTCGAGGAAATGATGTCTCATATGGTGAGCAAGGGCGAGGA
37. H2zinT-sfGFP-cam-rp	AACTTACTAAAGCGGCATCGAGGCGTTATCATGAGAATACCATATGAATATCCTCCTTAG
38. qPCR-zinT-fp	CAAACCTGGCTGTTGCTTTAGG
39. qPCR-zinT-rp	TCTGTAAAGGGTTTGCCGTG
40. qPCR-HKG-16srRNA-fp	GTAAATACCTTTGCTCATTGA
41. qPCR-HKG-16srRNA-rp	ACCAGGGTATCTAATCCTGTT

Supplementary Table 2 | List of plasmids used or constructed in this study.

Plasmid Name	Gene Insert	Resistance	Source
1. pSLTS	bet, gam, exo recombinase enzymes, ISceI enzyme	Amp	¹ (Addgene plasmid 59386)
2. pT2SK	kanamycin cassette, I-SceI cleavage site	Kan	¹ (Addgene plasmid 59383)
3. sfGFP-pBAD	Superfolder Green fluorescent protein	Amp	⁴
4. pBAD24	L-arabinose inducible, Base Plasmid	Amp	⁵
5. pBAD33	L-arabinose inducible, Base Plasmid	Cam	⁵
6. pBZntR-mEos3.2	zntR-mEos3.2-FLAG	Amp	³
7. pBZR(C115S)-mEos3.2	zntR-C115S-mEos3.2-FLAG	Amp	³
8. pApoZur_mE	zur-C88S- mEos3.2-FLAG	Amp	²
9. pZur_mE	zur-mEos3.2-FLAG	Amp	²
10. p24ZRG(C115S)	zntR-C115S-sfGFP	Amp	This Study
11. p33ZRG(C115S)	zntR-C115S-sfGFP	Cam	This Study
12. p33ZRG	zntR-sfGFP	Cam	This Study
13. pET3a	T7 (IPTG inducible)	Amp	Novagen
14. pZntRapo	ZntR(C115S)	Amp	³
15. pZurC113	Zur (C17S, C152S, C158S)	Amp	This Study
16. pZurC113D49A	Zur (C17S, C152S, C158S, D49A)	Amp	This Study
17. pZurC158	Zur (C17S, C113S, C152S)	Amp	This Study
18. pUCmEos3.2:cat	mEos3.2-cat	Amp, Cam	³

Supplementary Table 3 | List of strains constructed in this study.

Strains	Plasmids	Chromosomal modification	Source
1. BW25113	none	Base Strain	Keio collection
2. JW3254-5	none	<i>ΔzntR</i>	Keio collection
3. ZRM3.2	none	<i>zntR-mEos3.2</i>	³
4. DZ	none	<i>Δzur</i>	This study
5. Zur ^{mE} -DZR	none	<i>zur-mEos3.2-FLAG, ΔzntR</i>	This study
6. DZR-Zur ^{mE} -pZRG(C115S)	p24ZRG(C115S)	<i>zur-mEos3.2-FLAG, ΔzntR</i>	This study
7. DZ-DZR	none	<i>Δzur, ΔzntR</i>	This study
8. DZ-DZR-pZmE	pZur_mE	<i>Δzur, ΔzntR</i>	This study
9. DZ-DZR-pZmEC88S	pApoZur_mE	<i>Δzur, ΔzntR</i>	This study
10. DZ-DZR-pZRG(C115S)	p33ZRG(C115S)	<i>Δzur, ΔzntR</i>	This study

11.	DZ-DZR-pZmE-pZRG(C115S)	pZur_mE, p33ZRG(C115S)	<i>Δzur, ΔzntR</i>	This study
12.	DZ-DZR-pZmEC88S-pZRG(C115S)	pApoZur_mE, p33ZRG(C115S)	<i>Δzur, ΔzntR</i>	This study
13.	DZ-DZR-pZmE-ZRG	pZur_mE, p33ZRG	<i>Δzur, ΔzntR</i>	This study
14.	ZRC115S	none	<i>zntR(C115S)</i>	This study
15.	ZRC115S-ZINTG	none	<i>zntR-C115S, zinT-sfGFP</i>	This study
16.	DZR-ZINTG	none	<i>ΔzntR, zinT-sfGFP</i>	This study
17.	ZINTG	none	<i>zinT-sfGFP</i>	This study

Supplementary Table 4 | Abbreviations used in this study.

Abbreviation	Full form
SMT	Single-molecule tracking
SCQPC	Single cell quantification of protein concentration
WT	Wild Type
Zur	Zinc Uptake Regulator
ZntR	Zinc Transport Regulator
mE	mEos 3.2 protein
sfGFP or G	Super-folder Green Fluorescent Protein
Amp	Ampicillin
Kan	Kanamycin
Cam or Cat	Chloramphenicol
PDF	Probability Distribution Function
CDF	Cumulative Distribution Function
FD	Freely Diffusing
NB	Non-specific Binding
TB	Tight Binding
PWDD	Pair-wise Distance Distribution
iqPALM	Image-base quantitative photo-activated localization microscopy
smFRET	Single-molecule Förster Resonance Energy Transfer
PALM	Photo-Activated Localization Microscopy

1.2 *Live cell imaging sample preparation, method and data processing for single-molecule imaging, tracking, and protein quantification experimental procedure*

1.2.1 *Sample preparation for live cell imaging:*

A single *E. coli* cell colony was inoculated into and grown in LB medium for 18 h at 37 °C. This overnight culture was diluted 1:100 in M9 medium³ supplemented with amino acids (GIBCO, cat. #: 11130051), vitamins (GIBCO, cat. #: 11120052), and 0.4% glycerol, and further grown to OD600 of 0.3. L-arabinose was added to induce plasmid expression for 0 - 20 mins when applicable. For Zn stress, ZnSO₄ was added into the media to a final concentration of 20 μM or 100 μM. 2 mL of the cell culture was pelleted via centrifugation and washed thrice with the same M9 media (supplemented with 0.4% glucose instead of glycerol), and was further incubated at 37 °C for 1 hour to help maturation of the fluorescent protein tags. The cells were then collected by centrifugation and added onto an agarose gel pad between a coverslip (Thermo Scientific Cat. #: 20848) pre-dispersed with 100 nm gold nanoparticles (Ted Pella, Inc., Cat. #: 15708-9) and a glass slide (VWR Lot #: 48300-37), and sealed with epoxy-glue.

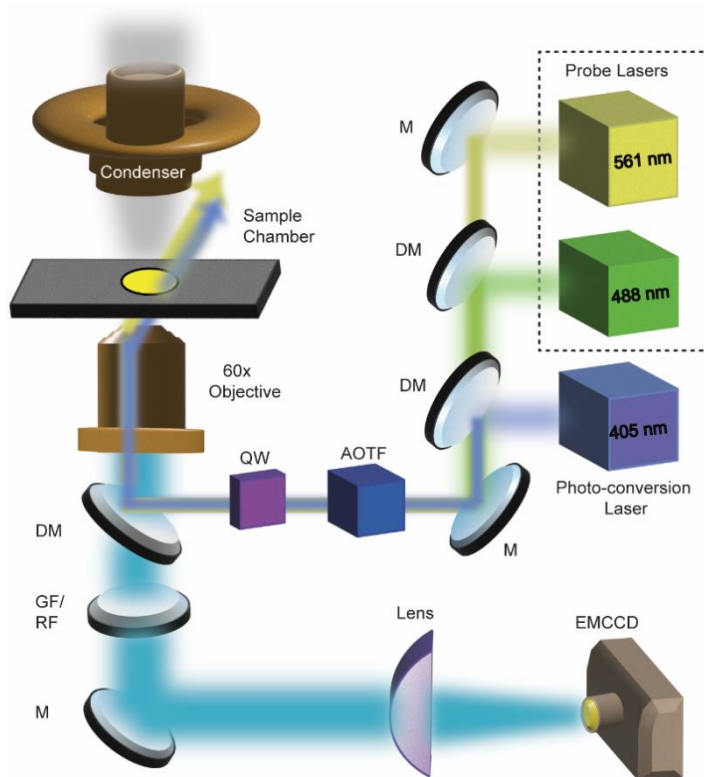
1.2.2 *Single-molecule tracking (SMT) and single cell quantification of protein concentration (SCQPC):*

SMT via stroboscopic imaging and SCQPC were performed as described previously, using a homebuilt PALM microscope based on Olympus IX71 (Supplementary Fig. 1)^{2,3}. For SMT, a short (20 ms) and low power (1-100 W/cm²) 405-nm laser illumination was used to photoconvert a single mEos3.2 tagged protein from its native green fluorescent form to the red fluorescent form. 30 pulses of a 561-nm

laser exposure (21 kW/cm²), with 4 ms pulse duration and time-lapse $T_{fl} = 40$ ms was used to excite this red fluorescence. The EMCCD exposure was synchronized with the 561-nm laser pulses, and this stroboscopic imaging allowed us to obtain diffraction limited images of both stationary and mobile single molecules. This process was repeated for 500 cycles for each cell to obtain a tracking movie.

After the SMT cycles, we perform the SCQPC part. Here the cells were illuminated with 405-nm laser (100 W/cm²) for 2 mins to photoconvert all the remaining green mEos3.2 to their red form, the emission of which was excited by 561-nm laser illumination at the same power density for 2000 frames to obtain the whole cell fluorescence intensity of mEos3.2 and photobleach them. This step was repeated for a total of 3 cycles to ensure all mEos3.2 tagged proteins were photoconverted, imaged, and photobleached.

After all the fluorescence of the mEos3.2 in the cell was photobleached following the steps above, the total green fluorescence of the remaining sfGFP-tagged-ZntR was excited by a 488-nm laser (7 kW/cm²), for 1000 frames to obtain the whole cell intensity.



Supplementary Fig. 1 | Schematics of PALM microscope setup. a, PALM microscope setup for in vivo single molecule tracking and stroboscopic imaging. (M: Mirror; DM: Dichroic Mirror; GF/RF: Green Filter/ Red Filter; AOTF: Acoustic Optical Tunable Filter; QW: Quarter Waveplate; 60× TIRF oil immersion objective (Olympus PlanApo N 60× oil 1.45); Lens (10.2 cm focal length, as part of the Olympus IX71 left port). Figure created with Adobe Illustrator.

1.2.3 Determination of total cellular Zur and ZntR copy numbers

To obtain the total Zur copy number N_{cell} in each cell, the whole cell mEos3.2 red emission obtained in the SCQPC step, was divided by the average intensity of a single mEos3.2 molecule in that cell obtained from the SMT steps^{2,3}. The total copy number was estimated using the following Eq. S1:

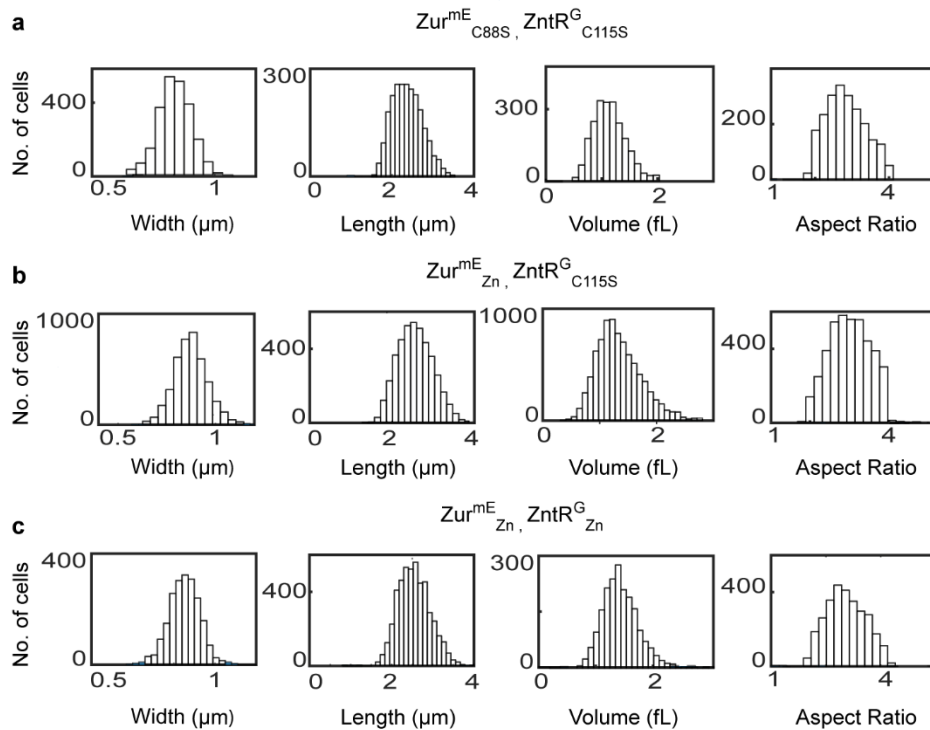
$$N_{cell} = \frac{N_{SMT} + N_{SCQPC}}{PE_{mEos3.2} * OS_{Zur}} \quad \text{Eq. S1}$$

where, N_{SMT} and N_{SCQPC} , are the copy numbers obtained from the SMT and SCQPC, respectively. $\text{PE}_{\text{mEos3.2}}$ is the photoconversion efficiency of mEos3.2 protein ($=0.42$)^{6,7} and OS_{Zur} is the oligomerization state of Zur (homodimer, $\text{OS}_{\text{Zur}} = 2$).

To determine the single-molecule intensity of mEos3.2 from the SMT step, a custom-written MATLAB software called iQPALM (Image-based Quantitative Photo-Activated Localization Microscopy) (Supplementary Table 4)³ and Figshare software⁸ was used to process the fluorescence images to determine the centroid location of the candidate red single mEos3.2 fluorescence spots. The cell boundary was first determined using the bright field optical transmission image by mapping out pixels around the cell that showed the largest pixel intensity contrast³. Furthermore, cells with length of $2.7 \pm 0.9 \mu\text{m}$ were selected to decrease the possibility of picking dividing cells, which potentially contain more than one copy of chromosome (Supplementary Fig. 2, 2nd column). The cell boundaries in the region of interest (ROI) were then superimposed onto the corresponding fluorescence image to select candidates of single-molecule fluorescence within the cell boundaries, which were then determined by fitting the fluorescence spots with a two-dimensional Gaussian point spread function (PSF) in Eq. S2, as was described previously^{2,3}.

$$I(x, y) = A \exp \left[-\frac{(x - x_o)^2}{2\sigma_x^2} - \frac{(y - y_o)^2}{2\sigma_y^2} \right] + B \quad \text{Eq. S2}$$

where, $I(x,y)$ is the fluorescence intensity at position (x,y) , and A , B , (x_o, y_o) , and (σ_x, σ_y) are the amplitude, background, centroid position, and standard deviations of the Gaussian function.



Supplementary Fig. 2 | Exemplary distribution of cell width, length, volume, and aspect ratio. **a**, DZ-DZR-pZmEC88S-pZRG C115S strain expressing $\text{Zur}^{\text{mE}}_{\text{C88S}}$ and $\text{ZntR}^{\text{G}}_{\text{apo}}$ (i.e., $\text{ZntR}^{\text{G}}_{\text{C115S}}$) in 1978 cells, **b**, DZ-DZR-pZmE-pZRG C115S strain expressing Zur^{mE} and $\text{ZntR}^{\text{G}}_{\text{apo}}$ in 4267 cells, and **c**, DZ-DZR-pZmE-pZRG strain expressing Zur^{mE} and ZntR^{G} in 2039 cells. The bin sizes are $0.04 \mu\text{m}$ (Width), $0.13 \mu\text{m}$ (Length), 0.1 fL (Volume) and 0.2 (Aspect Ratio). The histograms comprise only cells that were included in subsequent analysis. Source data are provided as a Source Data file.

To estimate the total ZntR copy number, we need to obtain the single sfGFP intensity. Since sfGFP is not a photoconvertible or photoactivatable fluorescent protein, the single sfGFP intensity was determined

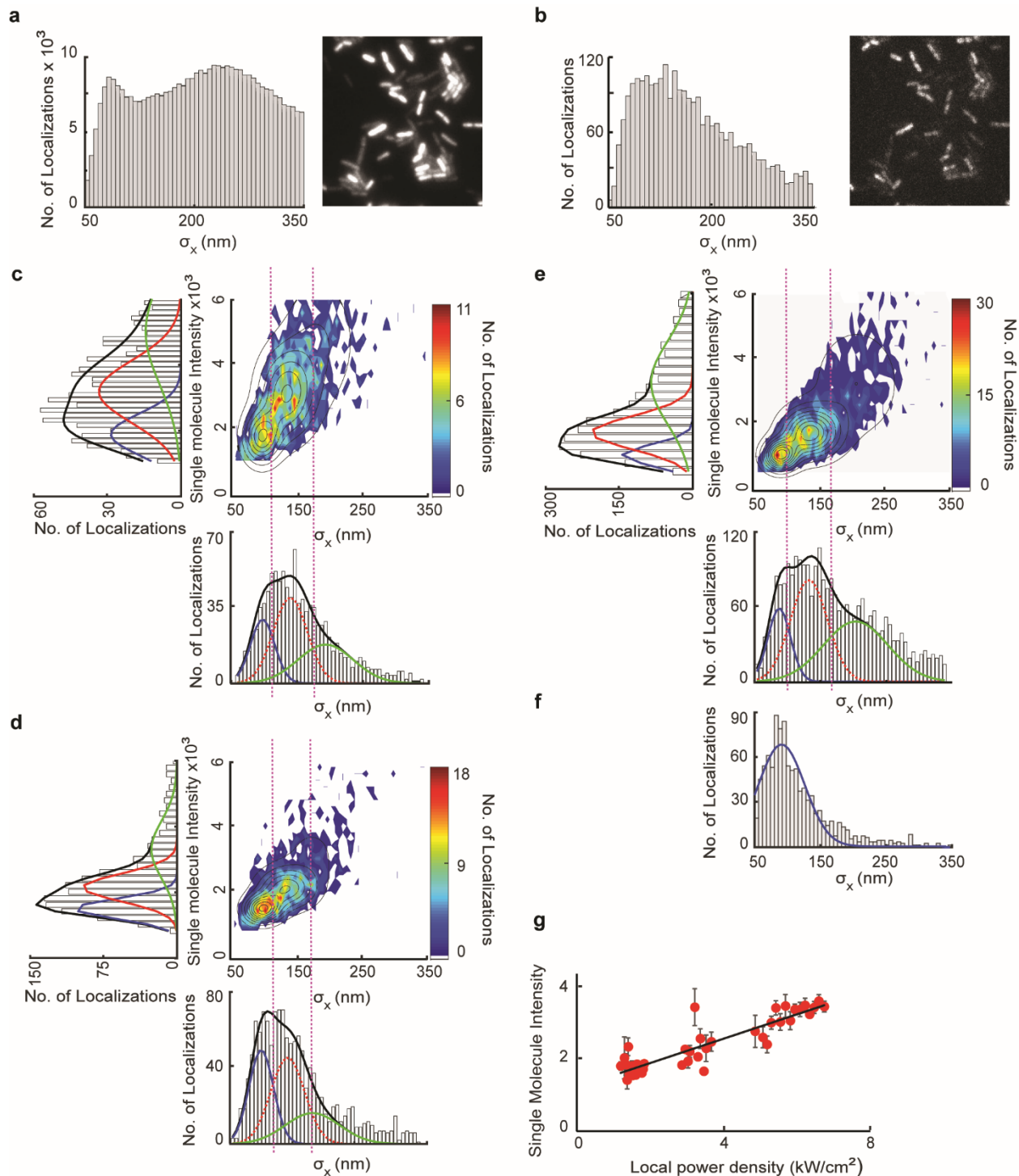
separately as described: Firstly, a sample prepared from a strain containing only the ZntR_{apo}^G (DZ-DZR-pZRG115S; Supplementary Table 3) was illuminated using 488-nm laser excitation (2-7 kW/cm²) with 4 ms exposure for 10000 frames. The candidate fitted spots were then filtered by their spot sizes; here the spot size is measured by the standard deviation of the fitted Gaussian PSF (Eq. S2), σ_x (or σ_y), the theoretical value of which is around 77 nm on the basis of diffraction-limited resolution ($\frac{\lambda}{2NA}$; NA is the objective numerical aperture). Based on the distribution of σ_x , we rejected any spot with σ_x smaller than 50 nm (too narrow for a reasonable single-molecule PSF) and any σ_x greater than 350 (too wide for a clean single-molecule PSF) (Supplementary Fig. 3a)³. Further, the first 1200 frames of each cell were removed to decrease the contamination by fluorescence images of an ensemble of sfGFP in the cell (Supplementary Fig. 3b), as initially the cell contains many sfGFP-tagged ZntR_{apo} molecules which can be spatially close to each other and the spot-size can overlap with the long tail of the sigma distribution of single molecules (Supplementary Fig. 3b); these were removed temporally as was done previously⁹. From the remaining frames, the candidate single sfGFP spots were analyzed similarly as described above, to obtain the intensity of the fitted Gaussian function ($I(x,y)$) and the spot sizes described by (σ_x, σ_y) in the Gaussian function.

To decouple and determine the local power dependence of the single molecule intensity, experiments were done at three different power densities. Two-dimensional histograms of these filtered σ_x and their corresponding intensity (I), which is the integrated volume of the fitted Gaussian function component in Eq. S2) resolved three populations (Supplementary Fig. 3c-e). These candidate populations were globally fitted with a three-component bivariate Gaussian function across the three different experimental power densities sharing the width (σ_{x2}), and peak position (x_2), of the 2nd component in Eq. S3 (Supplementary Fig. 3c-e, red dotted line) to further resolve the correct candidate spots and obtain their intensities:

$$z = \sum_{i=1}^3 A_i e^{-\frac{(x-x_i)^2}{2\sigma_{xi}^2}} e^{-\frac{(I-I_i)^2}{2\sigma_{Ii}^2}} \quad \text{Eq. S3}$$

Eq. S3 comprises 3 components of a bivariate Gaussian function where the first and third components correspond to populations of σ_x narrower and far greater than the theoretical value of a single-molecule PSF (~77 nm), respectively. The population of σ_x lower than the theoretical value was determined to be false detections as this population was also observed in the wild type BW25113 strain that does not express any fluorescence tag (Supplementary Fig. 3f). The 2nd component in the fitting corresponds to a population of σ_x (centered at 137 nm), similar to the expected PSF size, and thus is assigned as single sfGFP molecules in the cell. Due to high cell-to-cell heterogeneity of protein concentration, the total fluorescence of every cell decays to different extents after 1200 frames, at which there are still many cells that contain many sfGFPs and whose fluorescence is from the ensemble fluorescence. We assigned the population of σ_x with mean value higher than 137 nm to such any remaining ensemble fluorescence.

The single-molecule population σ_x (=137 nm) from the 2nd term (Supplementary Fig. 3c-e, red Gaussian fit) was selected out using thresholds (magenta lines) determined from the fitting (Supplementary Fig. 3c-e). For these selected single-molecule candidate spots, the corresponding intensities and the local power densities were determined (from the centroid position of the cell in the microscope field of view) and a calibration curve was formed. This single-molecule intensity and local power density calibration curve served to determine the corresponding single sfGFP intensity (Supplementary Fig. 3g).



Supplementary Fig. 3 | Determination of single-molecule intensity of sfGFP. **a**, Left: distribution of filtered candidate fluorescence spot size ($n = 429454$), measured by the Gaussian function standard deviation σ in Eq. S2, $50 \text{ nm} < \sigma_x < 350 \text{ nm}$; right: a representative frame from the first 1200 frames. **b**, Left: distribution of the candidate spot sizes, σ_x , after removal of first 1200 frames, resolves a single population; right: a representative frame at number > 1200 . **c-e**, Two-dimensional distribution of the candidate spot sizes and intensities at three laser power densities 7 kW/cm^2 ($n = 1333$ spots) (**c**), 3.5 kW/cm^2 ($n = 1359$ spots) (**d**), and 2 kW/cm^2 ($n = 2640$ spots) (**e**). The corresponding one-dimensional projections of the σ_x and intensity are plotted along the x and y axes, respectively. The black line is the total fit. The three colored lines (blue, red, and green) are the three Gaussian components of the fit, corresponding to the false detection, single molecules, and multi-molecule/ensemble populations,

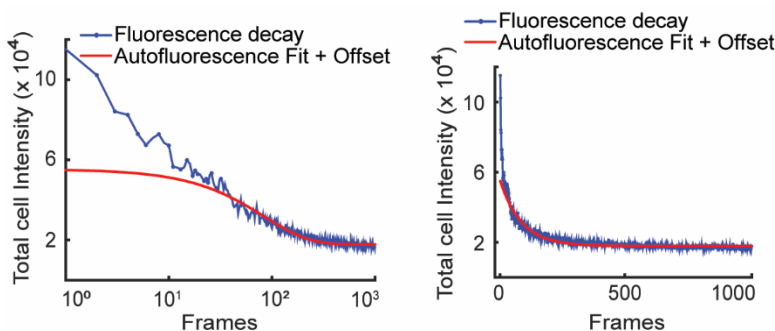
5

respectively. The dotted red line component represents the terms of the fit that were globally shared across the data of the three power densities. The vertical magenta dashed lines represent the thresholds applied to extract and isolate the middle population of correct candidates. **f**, Distribution of σ_x from WT BW25113 after similar filtering, shows only one population with average lower than 100 nm (blue population), resulting from false detection in the green channel for sfGFP imaging. **g**, Single molecule intensity vs. local power density calibration curve ($n = 5332$ spots). Source data are provided as a Source Data file.

Finally, the whole cell sfGFP intensity vs. time was fitted with a double exponential function and an offset (Supplementary Fig. 4) (Eq. S4):

$$y = Ae^{-k_1x} + Be^{-k_2x} + C \quad \text{Eq. S4}$$

where, the first component corresponds to the sfGFP fluorescence intensity and the 2nd to the cellular autofluorescence, and C is the background offset. The exponential fit was used only to determine the autofluorescence background and not to extrapolate the intensity at frame no. 1. Subtraction of the 2nd and 3rd terms of Eq. S4 from the raw initial value of the fluorescence at frame no 1 (Supplementary Fig. 4, blue curve) yields the total cellular sfGFP fluorescence.



Supplementary Fig. 4 | An example of a whole cell sfGFP fluorescence photobleaching decay curve (raw data, blue) obtained by imaging a strain that expresses only $ZntR_{apo}^G$ (DZ-DZR-pZRG115S) in linear-log (left) and linear-linear scale (right). The autofluorescence and offset (fits, i.e., 2nd and 3rd terms in Eq. S4) are shown in red. Source data are provided as a Source Data file.

The apparent copy number N_{SCQPC} of the sfGFP in the cell was calculated by dividing this initial total sfGFP fluorescence intensity with the single sfGFP intensity determined from the calibration curve (Supplementary Fig. 3g), with the local power density calculated from the centroid position of the cell. The total copy number of sfGFP-tagged ZntR in the cell N_{cell} was estimated using Eq. S5:

$$N_{cell} = \frac{N_{SCQPC}}{OS_{ZntR}} \quad \text{Eq. S5}$$

where OS_{ZntR} (=2) corresponds to the oligomeric state of ZntR (a homodimer).

1.2.4 Temporally profiling the derepression of *zinT*, a *Zur* regulon, in response to EDTA-induced Zn depletion

Profiling *zinT* expression at the translational level. Protein reporters such as β -galactosidase¹⁰, luciferase¹¹ as well as fusion fluorescent protein tags¹² have been widely used to track gene expression. To probe whether the transcription of *Zur* regulons is affected by $ZntR_{apo}$, we used sfGFP to tag *zinT*, a *zur* regulated periplasmic zinc trafficking protein¹³, to image its cellular protein concentration to report on its de-repression by *Zur* upon adding EDTA, a divalent metal ion chelator, to deplete cellular Zn levels¹⁴. The ZINTG (which carries the chromosomally tagged $ZntR^G$ and no other genetic modifications; referred to as wild type here), DZR-ZINTG (in which the chromosomal *zntR* is deleted by replacing by a *kan* drug marker), and ZRC115S-ZINTG (whose chromosomal *zntR* gene was mutated to *zntR_{apo}* (i.e., *zntR_{C115S}*))

(Supplementary Table 3) strains were grown in LB with appropriate antibiotics for 18 h at 37 °C. This culture was further diluted 1:100 in M9 imaging media supplemented with 20 μM Zn²⁺ to grow to OD₆₀₀ of 0.3. The cells were pelleted and washed with the same media and drop-casted into a petri-dish (Greiner Bio-One) pretreated with poly-L-lysine hydrobromide (Sigma). The cells were incubated in the petri-dish for 30 min to allow surface binding and washed with water to remove unbound cells. The same media was added to the surface-bound cells, which were further allowed to incubate for 1 h.

To follow the derepression of ZinT^G in the cell, M9 media supplemented with 2 mM EDTA¹⁴ was used to replace the media and the cells were imaged using 4 ms pulses of the 488 nm laser (1 kW/cm²) in stroboscopic imaging mode at 5 min intervals. The results are presented in Fig. 6c in the main text.

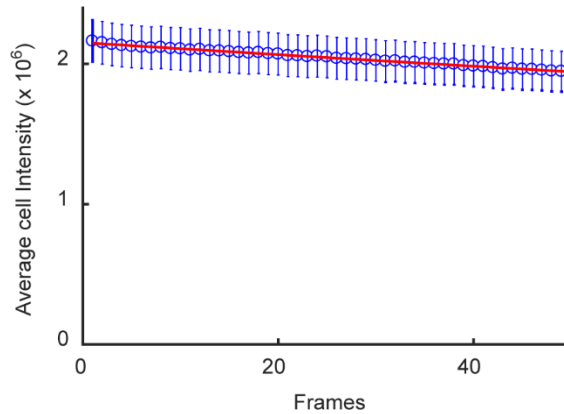
Moreover, we have determined, by imaging the ZinT^G strain (Supplementary Table 3) under steady state conditions with regular M9 media, that photobleaching effects are ~0.2% per image frame under our imaging conditions (Supplementary Fig. 5). Briefly, the cells were grown in M9 media to an OD₆₀₀ of 0.3 and treated with 2 mM EDTA for 1h to induce ZinT^G expression. The cells were then washed with regular M9 and imaged as described above. The photobleaching curve was fitted empirically with a double exponential function of the form:

$$I(t) = I_0 (pe^{(-\frac{t}{\tau_1})} + (1-p)e^{(-\frac{t}{\tau_2})}) \quad \text{Eq. S6}$$

where, I_0 the initial intensity, p is the fractional amplitude, and τ 's are time constants. Fitting with Eq. S6 (Supplementary Fig. 5, red line), we can extract $p = 0.34$, $\tau_1 = 497.43$ frames and $\tau_2 = 487.05$ frames;

Therefore, substituting in Eq. S6, with $t = 1$ frame,

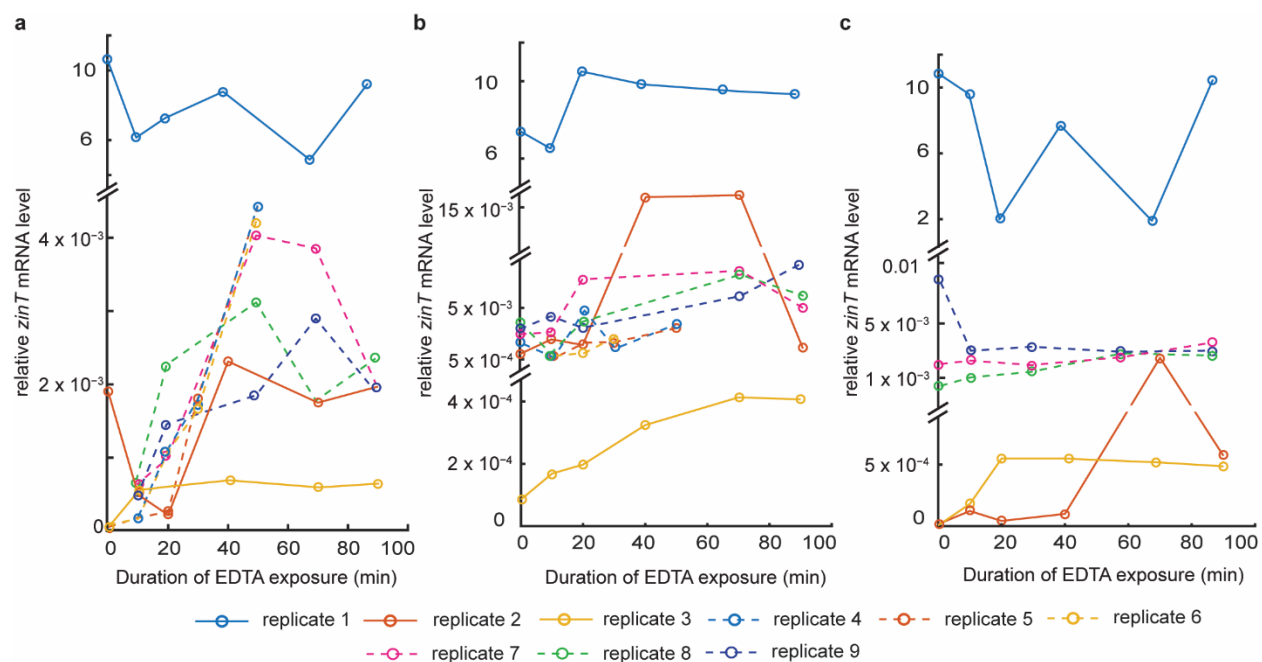
$$\frac{I(1)}{I_0} = 99.80\% \Rightarrow \Delta I = I(1) - I_0 = -0.2\%$$



Supplementary Fig. 5 | Photobleaching control measurement of ZinT^G. Fluorescence intensity obtained by imaging the ZinT^G strain, under steady state condition in regular M9 imaging media using low intensity 488 nm laser (1 kW/cm²). The blue dots are fluorescence intensity averaged over >100 cells measured in each consecutive frame. The red line is a double exponential fit with Eq. S6. Error bars are SEM from three independent experimental replicates. Source data are provided as a Source Data file.

Attempt to profile *zinT* expression at the transcriptional level, but data show irreproducibility. We also used mRNA quantitation via RT-PCR to profile the derepression of *zinT* upon adding EDTA. Briefly, the wild-type strain (BW25113), the $\Delta zntR$ strain JW3254-5 (in which the endogenous *zntR* is replaced by a *kan* drug marker), and the *zntR*_{apo} mutant strain ZRC115S (in which the chromosomal *zntR* gene carries a

C115S mutation) (Supplementary Table 3) were grown in 6 mL LB with appropriate antibiotics for 18 h at 37 °C. This culture was further diluted 1:100 in M9 imaging media and grown to OD₆₀₀ of 0.3. The cells were treated with 250 μM EDTA¹⁵ for the desired amount of time (0, 10, 20, 40, 70 or 90 min) to induce derepression of *zinT*, washed and collected by centrifugation. Total mRNA was purified using PureLink® RNA Mini Kit (Life Technologies), treated with turbo DNA-free™ kit (Invitrogen) and quantified by NanoDrop spectrophotometer (Thermo Scientific). Purified mRNAs were converted to the cDNA using SuperScript® III First- Strand Synthesis SuperMix kit (Life Technologies) with random hexamer primers. The primer pair, qPCR-zinT-fp and qPCR-zinT-rp was used for RT-PCR of *zinT* gene² (Supplementary Table 1). The mRNA levels of *zinT* was assessed relative to that of the housekeeping gene (16S rRNA) as an internal reference¹⁶. The samples were measured in triplicate in an optical 96-well plate (Life Technologies) in a reaction mixture with the SYBR Green reagent (Life Technologies) and imaged using QuantStudio™ 7 Pro (Thermo Fisher) Real-Time PCR System. We expected to observe a derepression of *zinT* mRNA levels that increases with the duration of exposure to EDTA. However, even with many attempts, the results do not show reproducibility for all three strains among the replicates (Supplementary Fig. 6). This irreproducibility in measuring time-response of gene transcription derepression at the mRNA level might come from the low mRNA copy number and the short lifetime of the mRNA in bacteria^{17,18}.



Supplementary Fig. 6 | Irreproducible RT-PCR analyses of relative *zinT* mRNA levels after addition of 250 μM EDTA. a, The JW3254-5 ($\Delta zntR$ deletion strain). **b,** The ZRC115S (*zntR*_{apo} mutant strain). **c,** The BW25113 (wild-type strain). The individual curves are independent replicates. Source data are provided as a Source Data file.

1.3 Construction of strains, protein purification, DNA labeling, sample preparation, imaging and data analysis for *in vitro* smFRET studies

1.3.1 Mutagenesis, expression, purification, and fluorescence labeling of Zur variants

To label Zur with the FRET acceptor Cy5, site-directed mutagenesis was used to make Zur variants that contain a unique labelable cysteine in each monomer (see Supplementary Notes 6.1) on the choice of cysteine position, the removal of other natural cysteines, and protection of essential Zn-binding cysteines at structural and regulatory sites). For example, the Zur variant, Zur^{Cy5}, was created, expressed, purified, labeled and further purified to obtain the single Cy5-labeled form at the specific cysteine at position C113. All Zur variants were cloned in a pET3a vector and the sequence was confirmed. The proteins were expressed in *E. coli* (BL21 DE3) cells and purified as previously described¹³. Briefly, the cells were grown

until $OD_{600} \sim 0.6$ before 0.4 mM isopropyl-beta-D-thiogalactopyranoside (IPTG) and 0.2 mM $ZnSO_4$ were added. After an additional 3 hours growth at 37 °C, cells were harvested by centrifugation and then lysed with lysozyme in lysis buffer (20 mM Tris, 300 mM NaCl, 50 mM Dithiothreitol (DTT), and 10% glycerol at pH 8.0). The cells were further disrupted with three cycles of freeze and thaw followed by sonication. The proteins were collected by centrifugation and the pellet was suspended in denaturing buffer (20 mM Tris, 6 M Urea, 100 mM Dithiothreitol (DTT) at pH 8.0). After 30 min of denaturing at 4 °C, the solution was centrifuged to remove insolubles, and the soluble proteins in the supernatant were collected and then added drop by drop into the refolding buffer (20 mM Tris, 100 μ M $ZnSO_4$, 5 mM Dithiothreitol (DTT) at pH 8.0) to refold the protein. Then, the protein was purified by anion exchange column (HiTrap Q HP, GE Healthcare). The collected fractions were further purified through a Heparin affinity column (16/10 Heparin FF, GE Healthcare), a gel filtration column (HILOAD 26/60 Superdex 200 PR, GE Healthcare), and an anion exchange column (Mono Q 5/50 GL, GE Healthcare). Protein purity was confirmed by SDS-PAGE, quantified using UV measurement at 280 nm, and stored at -80 °C in 50 mM Tris buffer with 50 mM NaCl, 10 nM $ZnSO_4$, 2 mM TCEP, and 10% glycerol at pH 8. Protein identity was confirmed by mass spectrometry (ESI-TOF, HPLC-ESI-MS/MS, UT Health San Antonio; Supplementary Fig. 28 later).

Cy5 FRET acceptor was labeled at the targeted cysteine in protein via maleimide chemistry. Zur was present as the fully-metallated holo-dimer form in the presence of $ZnSO_4$ with excess TCEP reducing disulfide bond formation. The Zn^{2+} ion first binds to the metal-binding cysteines of Zur, protecting these cysteines from dye labeling. Cy5-maleimide (Invitrogen) was added to the holo-Zur solution ([dye]:[Zur monomer] = 6:1) in 100 mM phosphate buffer solution at pH 7. The reaction mixture was kept on a shaker at 4 °C for ~18 hours and then quenched by adding excess beta-mercaptoethanol (BME). After incubating for additional 2 hours, the excess dye was removed through gel filtration (Superdex peptide 10/300 GL, GE Healthcare). Because Zur is a homodimer, a mixture of unlabeled, mono-labeled, and bi-labeled species were generated during the labeling reaction. The mono-labeled fraction was purified using an anion exchange column (Mono Q 5/50 GL) and has a dye:protein ratio of ~0.9:1. The extinction coefficient of 250,000 $M^{-1} cm^{-1}$ at 650 nm was used for determining the Cy5 concentration. Similarly, the extinction coefficient of 9,700 $M^{-1} cm^{-1}$ at 280 nm was used for determining the Zur concentration; this extinction coefficient was calibrated using the BCA protein quantification assay.

1.3.2 Mutagenesis, expression, purification for $ZntR_{apo}$ (i.e., $ZntR_{C115S}$ mutant) and Zn^{2+} binding assay

$ZntR(C115S)$ mutant was created, expressed, and purified as previously described^{19,20}. Briefly, the mutant was cloned in a pET3a vector and expressed in *E. coli* (BL21 DE3) cells. The cells were grown until $OD_{600} \sim 0.6$ before 0.4 mM IPTG was added. After an additional 3 hour growth at 37 °C, cells were harvested by centrifugation and then lysed with lysozyme in lysis buffer (50 mM Tris, 2 mM EDTA, 5 mM DTT at pH 8.0). The cells were further disrupted with three cycles of freeze and thaw and followed by sonication. The supernatant was collected after centrifugation and the proteins were precipitated out with 45% saturated $(NH_4)_2SO_4$ overnight. The precipitated proteins were resuspended in Tris buffer (20 mM Tris, 5 mM DTT at pH 8.0) and purified via a desalting column (HiPrep 26/10 Desalting, Cytiva), a Heparin affinity column (16/10 Heparin FF, GE Healthcare), and a gel filtration column (HILOAD 26/60 Superdex 200 PR, GE Healthcare). For the Heparin affinity column, the protein was stored in a buffer at pH 6 to increase binding affinity to the column. Protein purity was confirmed by SDS-PAGE, quantified using Bradford assay, and stored at -80 °C in 50 mM pH 8.0 Tris buffer with 250 mM NaCl, 5 mM DTT, and 5% glycerol. Protein identity was confirmed by mass spectrometry (HPLC-ESI-MS/MS, UT Health San Antonio, Supplementary Fig. 29 later).

Zn^{2+} binding was monitored by FluoZin-3 tetrapotassium salt (ThermoFisher, cat. #: F24194). Sample preparation, Zn^{2+} binding, and protein denaturing for the assay were followed as previously described^{20,21}. Briefly, all Zn^{2+} binding experiments were carried out in a PSB buffer containing 0.1 μ M $ZnSO_4$ and 1 mM DTT. DTT prevents Cys oxidation. *E. coli* $ZntR_{C115S}$ (4 μ M in terms of monomer) was mixed with 10 μ M $ZnSO_4$ and incubated at 4 °C for 30 min. The excess Zn^{2+} was washed five times using

10 k Amicon filter and equilibrated in a buffer containing 0.1 μM ZnSO_4 and 1 mM DTT. Then, the samples were denatured in 0.5% SDS (95 $^\circ\text{C}$ for 15 min). After cooling to room temperature, FluoZin-3 was added to have 10 μM in the samples, and fluorescence emission spectra (500- 600 nm) were collected with 494 nm excitation. The maximum emission (516 nm) was used to calculate Zn^{2+} content in comparison with a calibration curve obtained by measuring ZnSO_4 standard solutions.

1.3.3 Fluorescence labeled DNA preparation

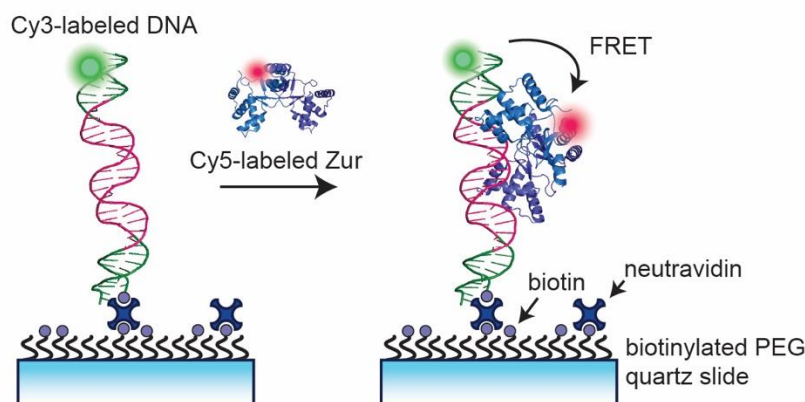
The Cy3 and biotin tagged DNA oligomeric strands were purchased from Integrated DNA Technologies (IDT, Coralville, IA) and dissolved in Nuclease-Free Duplex Buffer (IDT, Coralville, IA) and annealed together. Two types of double-strand DNA (dsDNA) constructs were used. The sequences of both constructs were from the *znuCB* gene promoter and contain the specific two-dyad sequence recognized by two Zur dimers: 5'/Cy3/AGAAGTGTGATATTATAACATTTTCATGACTA-3' and the complementary 5'-Biotin-TEG/TAGTCATGAAATGTTATAATATCACACTTCT-3'. The other construct is a truncated DNA that has only one dyad sequence: 5'/Cy3/AGAAGTGTGATATTATAACATT-3', and the complementary 5'-Biotin-TEG/AATGTTATAATATCACACTTCT-3'.

1.3.4 Functionalization of slide and immobilization of DNA for *in vitro* studies

A microfluidic channel containing the sample was formed by double-sided tape sandwiched between a quartz slide (Technical Glass Products, Inc. (TGP) and a borosilicate cover slip (Thermo Scientific). Quartz slides were first amine-functionalized with Vectabond (Vector Laboratories), followed by coating with biotinylated-polyethylene glycol (PEG) polymers (50:1 ratio of PEG and Biotin-PEG, Nanocs, m-PEG-SPA-5000 and biotin-PEG-NHS-3400) to reduce nonspecific protein and DNA adsorption on the quartz surfaces, and the biotinylated terminal group forms biotin-neutravidin linkages for immobilizing biotinylated DNA molecules (Supplementary Fig. 7)^{22,23}. Coverslips were also amine-functionalized using Vectabond and then coated with PEG polymers (Nanocs, 100 mg/mL m-PEG-SPA-5000). Quartz surfaces were further blocked using 2 mL BSA (0.1 mg/ml) to minimize non-specific binding. The neutravidin (Invitrogen) was introduced as 500 μL of 0.2 mg/mL in buffer solution (20 mM Tris, 200 nM ZnSO_4 , 2 mM MgCl_2 , 1 mM CaCl_2 , 100 mM potassium glutamate, 1 mM TCEP at pH 8.0) and incubated for 15 min. After washing out unbound neutravidin, 1 mL of 100 pM Cy3-labeled biotinylated DNA solution in buffer flowed through the channel for immobilization. Then, the Cy5-labeled Zur solution containing an oxygen scavenging system (0.1 mg/mL glucose oxidase, 0.025 mg/mL catalase, 4% glucose, and 1 mg/mL Trolox)²⁴ in the same buffer, and if applicable, containing Znr_{apo} , was flowed in continuously at a rate of 20 $\mu\text{L}/\text{min}$ for fluorescence imaging.

1.3.5 *In vitro* FRET experiments scheme

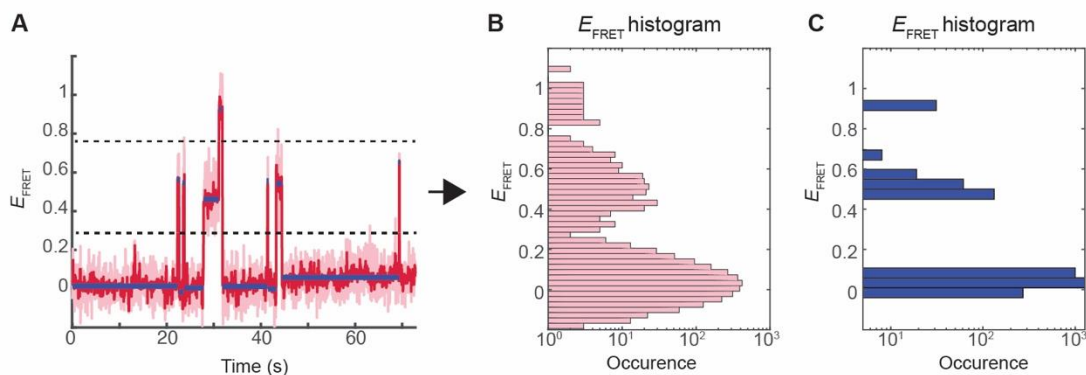
Single-molecule FRET experimental design and surface immobilization to probe Zur-DNA interactions are shown in Supplementary Fig. 7 and described in the text (Supplementary Methods 1.3.4), similarly as we studied other protein-DNA or protein-protein interactions^{23,25,26}. Double-strand DNA, in which one end of one strand had a FRET donor Cy3 and the other end of the other strand had biotin, was immobilized to the surface via a neutravidin-biotin linkage. The homo-dimeric Zur was labeled with a single FRET acceptor Cy5 and flew through the microfluidic channel across the immobilized DNA. Upon Zur binding to DNA, fluorescence intensities of Cy3 and Cy5 changed due to FRET. By monitoring the fluorescence intensities of Cy3 and Cy5 simultaneously, we studied Zur-DNA interactions in real-time.



Supplementary Fig. 7 | Experimental scheme of surface immobilization of Cy3-labeled DNA. Cy5-labeled Zur is supplied in a continuously flowing solution. Upon Zur binding to DNA, FRET occurs from the donor Cy3 (green sphere) to the acceptor (red sphere). Here, a homo-dimer Zur bound to 31-bp DNA is shown and the Cy5 location corresponds approximately to that in Zur^{Cy5} (Cy5 at C113). Zur and DNA structures are from PDB: 4MTD¹³. Figure created with Adobe Illustrator.

1.3.6 Single-molecule FRET experiments and data analysis

The single-molecule fluorescence experiments were performed using a prism-type total internal reflection microscope based on an Olympus IX71 inverted microscope, similarly as we previously reported^{23,25,26}. The immobilized Cy3-labeled DNA was excited by a continuous-wave circularly polarized 532-nm laser (CrystaLaser, GCL-025-L-0.5%) of ~7 mW focused onto an area of $\sim 94 \times 68 \mu\text{m}^2$ on the sample. The fluorescence of both Cy3 and Cy5 was collected by a 60 \times NA 1.2 water-immersion objective and split by a dichroic mirror into two channels using a Dual-View system (Optical Insights). The HQ550LP filter was used to reject the excitation laser light and each channel of fluorescence was further filtered (HQ580-60m or HQ660LP) and projected onto one-half of the imaging area of an EMCCD camera (Andor Ixon DV887) controlled by Andor IQ software. The time resolution for all the single-molecule experiments was 25 ms. All image analysis was done by custom-written codes in MATLAB (Supplementary Software 1). Individual Cy3 and Cy5 fluorescence intensity trajectories for immobilized DNA molecules interacting with Zur proteins were extracted from the fluorescence movie recorded by the camera. The FRET efficiency (E_{FRET}) was computed as an approximation using the relationship: $I_{\text{Cy5}} / (I_{\text{Cy5}} + I_{\text{Cy3}})$, where I_{Cy3} and I_{Cy5} are the fluorescence intensities. Then FRET trajectories that showed Cy3-Cy5 anti-correlated intensity fluctuation followed by a single photobleaching step were identified. The E_{FRET} histograms were compiled from hundreds of trajectories at each condition. In order to obtain higher resolution E_{FRET} histograms, a forward-backward non-linear (fnbl) filter was used to reduce the noise in the fluorescence trajectories^{27,28} and thresholded to distinguish E_{FRET} states. E_{FRET} value of each state was taken from the original E_{FRET} trajectories to avoid value changes by fnbl filtering (Supplementary Fig. 8).



Supplementary Fig. 8 | Construction of higher resolution E_{FRET} histogram. **a**, An example of E_{FRET} trajectory before (pink lines) and after forward-backward nonlinear (fbnl) filtering (red lines) with two thresholds (horizontal dashed lines) to distinguish the three E_{FRET} states. E_{FRET} value for each state is the mean value of each state (blue lines) from the original trajectory before fbnl filtering. **b**, E_{FRET} histogram from the original trajectory in (a). **c**, E_{FRET} histogram re-constructed with E_{FRET} values of individual states. Source data are provided as a Source Data file.

Supplementary Notes

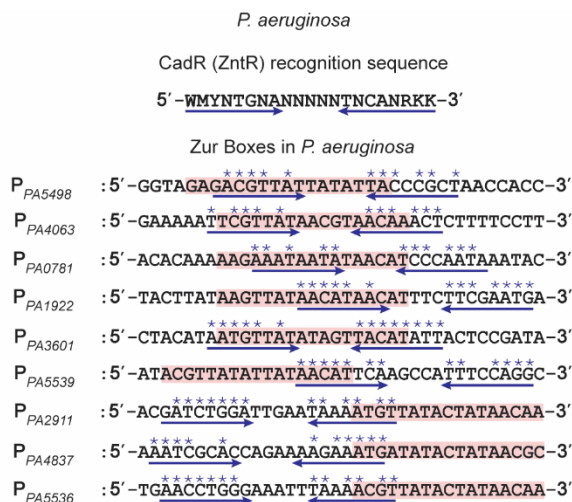
1 Genome sequence analysis and identification of potential recognition sequences of metal efflux regulators (e.g., ZntR) at promoters that are regulated by metal uptake regulators (e.g., Zur), or vice versa, in *E. coli*, other bacteria, and yeast

In this section, we present sequence analysis to identify potential recognition sequences of metal efflux regulators (e.g., ZntR) at promoters that are regulated by metal uptake regulators (e.g., Zur), or vice versa, in *E. coli*, other bacteria, and yeast. Softwares SnapGene and ApE were used to search for a potential efflux regulator recognition sequence around the known uptake regulator binding boxes, or vice versa, in the promoter regions of its regulons.

1.1 Potential partial ZntR recognition sequences around known Zur boxes in *E. coli* and other bacteria

The existence of sequences bearing some homology to known ZntR (or its homolog) recognition consensus sequence was observed around known Zur boxes in promoter regions in *E. coli*, *S. typhimurium*, and *P. aeruginosa*. In *E. coli*, these Zur regulon promoters include the promoters of genes *znuCB/znuA* (Zn^{2+} uptake gene cluster), *zinT* (periplasmic Zn^{2+} chaperone), *l31p* and *l33p* (a pair of ribosomal proteins), and *pliG* (a periplasmic lysozyme inhibitor) (Fig. 1b)¹³. In *S. typhimurium*, these include *zinT* and *znuABC* (Fig. 1b)^{29,30}.

In *P. aeruginosa*, the Zur regulon promoters include those of *PA5498* (Zn^{2+} uptake gene cluster, including *znuA*), *PA0781*, *PA2911*, *PA4837* and *PA1922* (putative TonB-dependent receptors), *PA5536* (*dksA2*, Zn^{2+} -independent global transcription regulator), *PA5539* (*folEB*, GTP cyclohydrolase), *PA4063* (periplasmic Zn^{2+} binding protein), and *PA3600* (ribosomal proteins) (Supplementary Fig. 9)³¹. In *P. aeruginosa*, Zn-efflux is regulated by CadR, a ZntR homolog of the MerR family that senses Zn^{2+} and Cd^{2+} as well; the recognition sequence of CadR is very similar to that of *E. coli* ZntR^{32,33}. Supplementary Fig. 9 shows the Zur boxes (pink shade) in *P. aeruginosa* that are overlapping with potential CadR recognition sequences (blue arrows, where blue asterisks show matches with CadR recognition consensus sequence)³².



Supplementary Fig. 9 | Partial recognition sequences of CadR, a ZntR-homolog, exist around Zur boxes in regulon promoters in *P. aeruginosa*. Potential CadR recognition sequences are shown by blue arrow dyads; the Zur boxes are highlighted in pink. The asterisks indicate matches with the known CadR consensus recognition sequence.

5 **1.2 *Aside from the Zur-ZntR Zn uptake-efflux regulator pair, potential Zn efflux regulator recognition sequences are also found at promoters controlled by Zn uptake regulators of other families in bacteria.***

In *B. subtilis*, Zur regulates Zn uptake^{34,35}, while CzcA, a ArsR-family regulator, is a Zn-efflux regulator³⁶. At the promoters of *zinT* (Zn²⁺ trafficking protein), *znuABC* (Zn²⁺ uptake gene cluster), *zagA* (Zn²⁺ chaperone) and *folEB* (GTP cyclohydrolase), which are regulated by Zur^{14,15}, we also discovered potential recognition sequences for CzcA Supplementary Fig. 10a).

In *S. pneumoniae*, the MarR-family AdcR is another Zn²⁺ uptake regulator³⁷, and SczA is another Zn²⁺ efflux regulator of the TetR family³⁸. At the promoter of *adcCBA* gene (a high affinity Zn²⁺ importer) regulated by AdcR, there are also potential SczA recognition sequences (Supplementary Fig. 10b).

15 **1.3 *This pattern of potential existence of partial efflux regulator recognition sequences around known uptake regulator binding box was also observed for regulator pairs involved in the homeostasis of other metals beyond Zn (for example: Fe and Ni) in bacteria.***

In *B. subtilis*, Fur is a Fe²⁺-uptake regulator while PerR is a Fe²⁺-efflux regulator both belonging to the Fur family (i.e., same family as Zur)³⁹. At the promoter of *dhbA* (gene involved in siderophore bacillibactin biosynthesis) regulated by Fur, we discovered potential PerR recognition sequence (Supplementary Fig. 10c).

In *E. coli*, NikR is a Ni-uptake regulator of the ribbon-helix-helix (RHH) family of DNA binding proteins⁴⁰, while RcnR is a Ni-efflux regulator of the CsoR family⁴¹. We discovered that at the promoter of gene *nikABCDE* (a Ni²⁺ transport system) regulated by NikR, there are also potential recognition sequence of RcnR (Supplementary Fig. 10d).

25 **1.4 *Oppositely, uptake regulator recognition sequence is also found around known efflux regulator binding box in bacteria.***

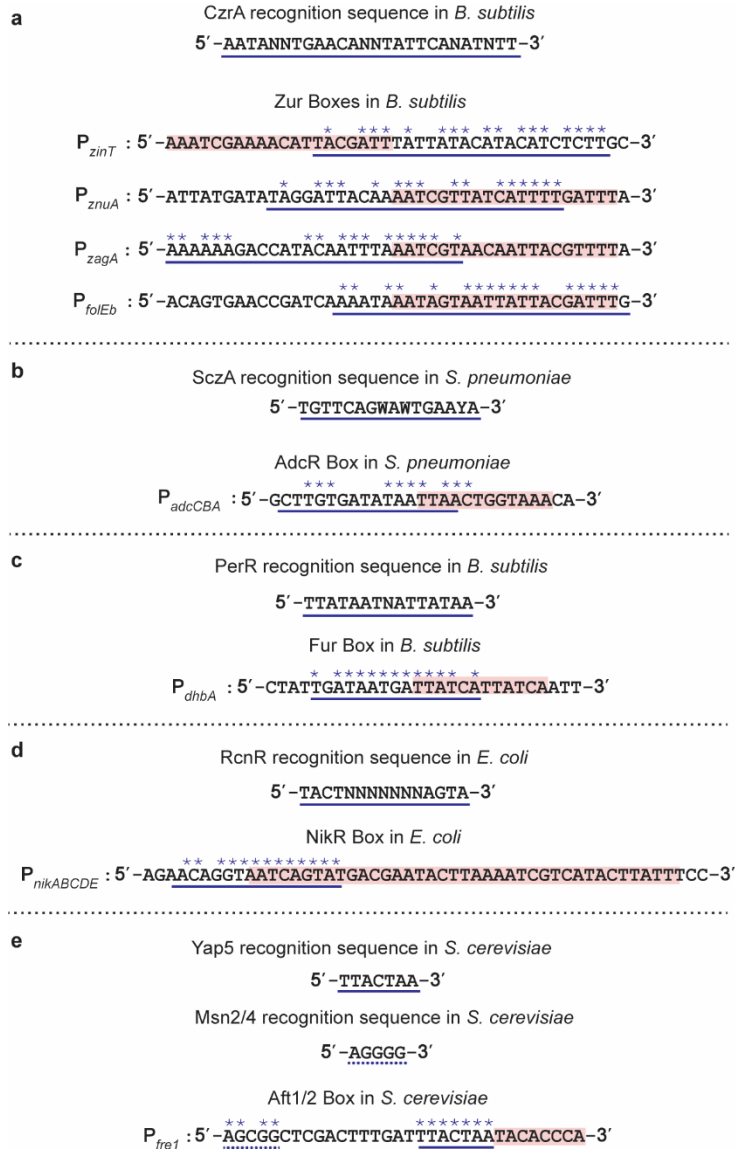
Additionally, in *B. subtilis*, Helmann et al. observed the existence of two potential Fur (uptake regulator) binding sites around the known PerR (efflux regulator) binding box⁴²; they also demonstrated the physiological importance of these two additional Fur boxes in iron efflux. It is worth noting that in this case, the recognition sequence of uptake regulator exists near efflux regular binding site, as opposed to the case of the recognition sequence of efflux regulator (e.g., ZntR) exists near the binding site of uptake

regulator (e.g., Zur), which suggests a broader relevance of potential uptake-efflux regulator cross-actions on DNA.

1.5 In yeast, a similar pattern of efflux regulator recognition sequence overlapping with known uptake regulator binding motifs can be found for iron homeostasis.

5 In yeast (*S. cerevisiae*), zinc homeostasis does not utilize pairs of efflux-uptake regulators and instead both uptake and efflux are controlled by one regulator; therefore the balance of cellular Zn concentration follows a different mechanism⁴³⁻⁴⁵.

10 On the other hand, for iron homeostasis, yeast uses distinct transcription factors to tightly regulate iron uptake and efflux⁴⁶. During conditions of iron deficiency, the two transcription factors, Aft1 and Aft2, bind to iron-regulatory promoter elements (FeREs) to activate the expression of genes involved in iron uptake, mobilization, and recycling, known as the iron regulons^{46,47}. When cellular iron reaches toxic levels, the regulators Yap5, Msn2, and Msn4 activate the expression of Ccc1, which detoxifies excess cytosolic iron by importing it into the vacuole for mobilization during deficiency⁴⁶⁻⁴⁸. Here, we discovered that
15 around the known Aft1/2 binding boxes on the promoter region of the iron regulon (e.g., *fre1*), there exist sequences that bear partial similarities with the known Yap5 and Msn2/4 binding motifs (Supplementary Fig. 10e).



Supplementary Fig. 10 | Potential efflux regulator recognition sequences exist around uptake regulator binding boxes. a, Top, the recognition consensus sequence of CzrA, a Zn-efflux regulator; bottom, existence of a partial CzrA recognition sequence around binding box of the Zn-uptake regular Zur in *B. subtilis*. **b,** Top, the recognition consensus sequence of SczA, an Zn-efflux regulator; bottom, existence of a partial SczA recognition sequence around a binding box of AdcR, a Zn-uptake regulator in *S. pneumoniae*. **c,** Top, the recognition consensus sequence of PerR, a Fe-efflux regulator; bottom, existence of a partial PerR recognition sequence around a binding box of Fur, a Fe-uptake regulator in *B. subtilis*. **d,** Top, the recognition consensus sequence of RcnR, a Ni-efflux regulator; bottom, existence of a partial RcnR recognition sequence around a binding box of NikR, a Ni-uptake regulator, in *E. coli*. **e,** Top and middle, the recognition consensus sequence Yap5 (solid blue underline) and that of Msn2/4 (dashed blue underline), both Fe-efflux regulators in *S. cerevisiae*; bottom, existence of a partial Yap5 and Msn2/4 recognition sequence around a binding box of Aft1/2, a Fe-uptake regulator in *S. cerevisiae*. The uptake regulator binding boxes have been highlighted in pink and the potential efflux regulator recognition sequences have been indicated by the blue underline, with each asterisk representing a match with their known consensus recognition sequence. All sequences were obtained from the NCBI genetic database.

2 Functionality and intactness of sfGFP-tagged ZntR in *E. coli* cells

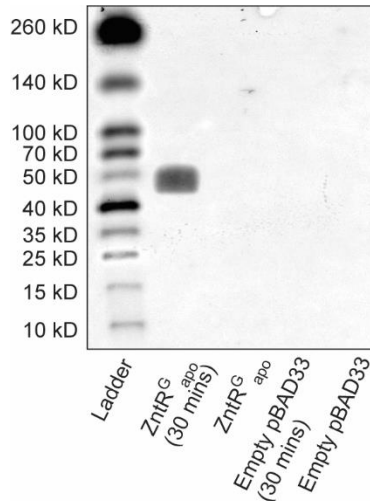
2.1 Western blot shows the intactness of ZntR-sfGFP fusion proteins

5 We previously showed that mEos3.2 tagged Zur is a functional regulator². The fusion tag remained largely intact in the cell (i.e., no discernible cleavage for the tagged Zur). We previously also showed that ZntR, tagged with mEos3.2 (a GFP variant), is also functional in the cell, but the mEos3.2 tag there has some cleavage in the cell³.

For sfGFP tagged ZntR that we use in this study, we performed western blot to check its intactness in the cells, focusing on the ZntR(C115S)-sfGFP fusion as the representative (i.e., ZntR_{apo}^G).

10 An anti-GFP antibody was used for immunoblotting. The DZ-DZR-pZRG115S strain which could express ZntR_{apo}^G from the pBAD33 plasmid inducible by L-arabinose, and a negative control strain DZ-DZR-pBAD33 containing the parent pBAD33 vector without insert were cultured overnight (18 hours) in 6 mL LB with appropriate antibiotics. A dilution (1:100) of the overnight culture was done in 5 mL M9 medium with amino acids (8% v/v 50x GIBCO), vitamins (4% 100x GIBCO), glycerol (0.4%) and the samples were further grown to an OD600 of 0.4. L-arabinose was then added to a final concentration of 1 mM into the appropriate cultures which were further incubated for 30 min to induce the plasmid expression. 1 mL aliquots of the resulting cell cultures were collected by centrifugation and washed with the same M9. The cell pellets were re-suspended in 95 μ L 2X SDS lysis buffer (BIORAD 2X Laemmli sample buffer), 2.5 μ L BME (2-mercaptoethanol; Sigma-Aldrich) and 2.5 μ L protein inhibitor cocktail (Promega). The lysed samples were run in SDSPAGE with ECL Plex fluorescent rainbow protein molecular weight markers (GE Healthcare Life Science) in 1X Running buffer, and then transferred onto the Hybond-LEP PVDF membrane (GE Healthcare Life Sciences). 4% Amersham ECL Prime blocking reagent (GE Healthcare Life Sciences) in PBS-T (0.1% Tween-20, Sigma-Aldrich) wash buffer was used to block the transferred membrane while shaking at RT for 2 hours. The membrane was washed with PBS-T and incubated with rabbit-derived antiGFP primary antibody (1:10,000 dilution, Rockland Immunochemical) for 18 hours at 4 °C. The membrane was rinsed with PBS-T 4 times and PBS buffer 3 times. The goat-derived Horseradish Peroxidase-conjugated Fab fragment anti-rabbit antibody (1:20,000 dilution, Rockland Immunochemical) was used as the secondary antibody, which could be probed with SuperSignal West Femto Maximum Sensitivity Substrate (Fisher Scientific). BioRad ChemiDoc MP Imaging System was used to detect peroxidase activity.

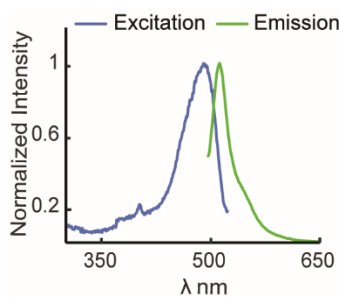
30 A dominant band from L-arabinose induced ZntR_{apo}^G was observed at MW ~ 43 kDa (that is, MW of ZntR + MW of sfGFP), and no discernable band was observed at MW ~ 27 kDa, which is expected to be the MW of sfGFP (Supplementary Fig. 11). Therefore, ZntR_{apo}^G is intact in the cell.



Supplementary Fig. 11 | Western blot demonstrated that ZntR^G is intact in the cell. Only ZntR^G expressed from a pBAD33 plasmid induced with L-arabinose was detectable (2nd column). In the negative controls, which are un-induced ZntR^G encoded in the same pBAD33 plasmid (3rd column), the empty pBAD33 (without the ZntR^G insert) induced with L-arabinose (4th column) and un-induced (5th column), no band was observed. The expected size of ZntR^G is ~ 43 kDa, and no cleavage product was observed (2nd column). Source data are provided as a Source Data file.

2.2 Ensemble fluorescence measurements show that the sfGFP-tagged ZntR is fluorescent

To test whether the sfGFP tag on ZntR is fluorescent inside cells, we performed bulk fluorescence measurements, using ZntR^G as the representative. Strain DZ-DZR-pZRG115S, which harbors the zntR-C115S-sfGFP gene encoded in a pBAD33 plasmid (Supplementary Table 2), was cultured in 6 mL LB with chloramphenicol (25 μg/mL), kanamycin (30 μg/mL) and 5 mM L-arabinose in 37 °C, shaking at 250 rpm, for 18 hours. The cells were then centrifuged, and the pellet was washed and re-suspended in PBS buffer (pH 7.4) for fluorescence measurements (Agilent Eclipse fluorometer). The emission spectrum of the green-fluorescent sfGFP was collected using 465 nm excitation; its excitation spectrum was obtained by monitoring the emission at 530 nm. Supplementary Fig. 12 shows the emission and excitation spectra of ZntR^G in the cells. The spectra closely match those expected for the sfGFP⁴. This shows that the sfGFP component of the fusion gene expressed inside the cell is fluorescent.



Supplementary Fig. 12 | The excitation (blue; emission detected at 530 nm) and emission (green; emission excited at 465 nm) spectra of cells expressing ZntR^G suspended in a PBS buffer. Source data are provided as a Source Data file.

3 Analysis of resolvable diffusion states of Zur in the cell and extraction of their effective diffusion coefficients (D) and fractional populations (A)

3.1 The resolved three diffusion states of Zur in the cell were assigned as FD, NB, or TB based on their diffusion coefficients and rationales

5 The distribution of the displacement lengths, r , obtained from tracking individual mE-tagged Zur proteins in two-dimension was fitted with a scaled probability distribution function (PDF_{2D}) (Fig. 2b, Eq. S7) or a cumulative distribution function (CDF_{2D}) (Eq. S8), using Brownian diffusion model to determine the number of resolvable diffusion states and their respective diffusion coefficients and fractional populations, as we previously did in studying Zur-DNA interactions² and ZntR-DNA interactions in *E. coli* cell³:

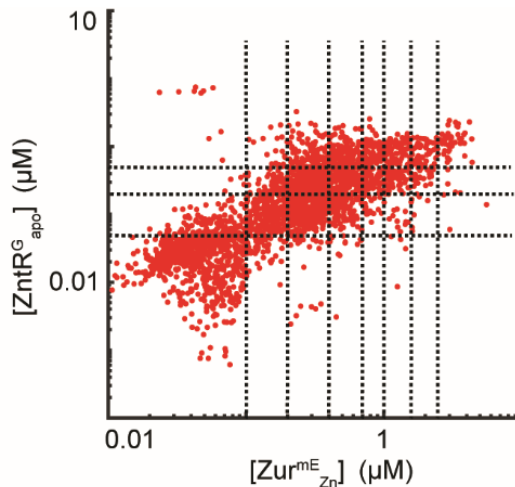
$$\text{PDF}_{2\text{D}}(r) = N \sum_i A_i \left(\frac{r}{2D_i T_{tl}} \exp\left(-\frac{r^2}{4D_i T_{tl}}\right) \right) \quad \text{Eq. S7}$$

$$\text{CDF}_{2\text{D}}(r) = \sum_i A_i \left(1 - \exp\left(-\frac{r^2}{4D_i T_{tl}}\right) \right) \quad \text{Eq. S8}$$

15 Here N is a scaling constant; D_i is the effective diffusion coefficient of state i whose fractional population is A_i , and $\sum A_i = 1$. T_{tl} is the time lapse (40 ms) in our time-lapse stroboscopic imaging. A linear combination of three Brownian diffusion states in the CDF was used here, assuming a quasi-static approximation, as we did previously because our measurement time resolution (40 ms) is faster than the interconversions between the states^{2,3}.

20 Only the first displacement of each experimentally obtained tracking trajectory was used to avoid potential biasing towards longer trajectories. In all data presented in this study, using all displacements of each trajectory does not affect the distribution of displacements as these distributions are statistically saturated (Supplementary Notes 3.3). Since the experimental PDF of displacement length requires a choice of bin size, fitting the CDF was preferred, and fitted parameters can be used to generate the corresponding fit for the PDF of displacement lengths.

25 From our single-cell protein quantitation of Zur^{mE} and ZntR^G_{apo} (or ZntR^G), we first sorted individual cells by their [ZntR^G_{apo}] (or [ZntR^G]) concentrations into groups of similar protein concentrations (e.g., horizontal dashed lines in Supplementary Fig. 13). Then within each group of cells having similar ZntR concentration, they are further sorted by their [Zur^{mE}] concentrations into groups having similar protein concentrations (e.g., vertical dashed lines in Supplementary Fig. 13).



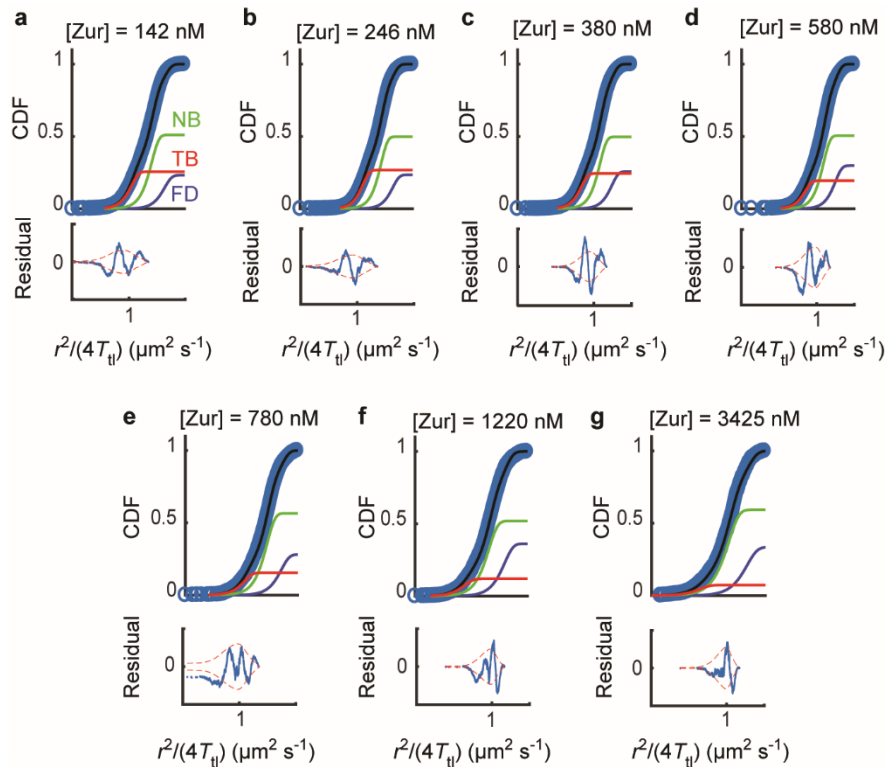
Supplementary Fig. 13 | Example of a two-dimensional scatter plot of $[Zur^{mE}]$ vs $[Zur^{G}_{apo}]$ of 4267 cells for the DZ-DZR-pZmE-pZRC115S strain expressing both proteins from plasmids; each red dot represents one cell. The horizontal dashed black lines divide cells into four different $[ZntR^{G}_{apo}]$ groups, each of which was further divided into 6-8 $[Zur^{mE}]$ groups by the vertical dashed black lines. The division lines were chosen to ensure that each concentration group in general have several thousands of single-molecule tracking trajectories of Zur^{mE} . Source data are provided as a Source Data file.

5

A global CDF fit was performed across these Zur concentration groups sharing the D_i 's because the diffusion coefficient is more likely an intrinsic property of each diffusion state and expected to be independent of protein concentration. Their respective fractional populations (A_i) are allowed to differ among different cell groups. Analyzing the residuals of the fit, minimally three diffusion states were required for the fitting the results of Zur, as we observed earlier².

10

Supplementary Fig. 14 shows exemplary CDF fits across different Zur_{Zn} concentration groups at $[ZntR_{apo}] = 27 \pm 8$ nM (error bar here is the standard deviation among the individual cells in the group). The effective diffusion coefficients of the states, D_i 's, and their respective fractional populations, A_i 's, across different concentrations of Zur and ZntR are summarized in Supplementary Table 5 and Table 6.



15

Supplementary Fig. 14 | Extraction of Zur^{mE} diffusion coefficients and fractional populations. (a-g) Top: exemplary global CDF fits for 1152 cells with $[ZntR^{G}_{apo}] = 27 \pm 8$ nM across different Zur^{mE} concentration groups. The red, green, and blue curves represent the resolved TB, NB, and FD states. The black lines are the overall fits of the CDFs. Bottom: the residuals in blue are shown with the 95% confidence bounds in red. Data provide in Supplementary Table 5 and Table 6.

20

The assignments of the three resolved states of Zur in the *E. coli* were reported, rationalized, and justified in our previous study². The fastest diffusion state of Zur^{mE} has an effective diffusion coefficient $D_{FD} \approx 5 \mu\text{m}^2/\text{s}^2$ and was assigned to those Zur proteins freely diffusing in the cytosol (i.e., FD state); the slowest diffusion state has an effective diffusion coefficient $D_{TB} = 0.04 \mu\text{m}^2/\text{s}^2$ and was assigned as Zur proteins tightly bound to DNA (e.g., at a Zur box) (i.e., TB state). The slight motion of TB state reflects chromosome dynamics and our experimental localization uncertainties of ~ 12 nm^{3,49-53}. The intermediate diffusion state has an effective diffusion coefficient $D_{NB} = 0.4 \mu\text{m}^2/\text{s}^2$ and was assigned to Zur non-specifically binding to DNA (i.e., NB state).

25

5 The values obtained for the diffusion coefficients are similar to what were previously observed for Zur², other metal-sensing regulators³ and other transcription factors in *E. coli*⁵³⁻⁵⁶. It is worth noting that these are effective diffusion coefficients, not intrinsic diffusion coefficients, as the effective values are influenced by the cell-confinement effects and the experimental time resolution (i.e., time lapse between images). The difference between effective and intrinsic diffusion coefficients are minimal for the TB and NB states as they are either quasi-stationary or slow, and the difference for FD state is larger, but FD state is always the fastest among the three states, as we evaluated previously^{2,3}.

Supplementary Table 5 | Summary of all the extracted Zur^{mE} diffusion coefficients of the three different states.

Proteins in the Strain	D_{FD} ($\mu\text{m}^2 \text{s}^{-1}$)	D_{NB} ($\mu\text{m}^2 \text{s}^{-1}$)	D_{TB} ($\mu\text{m}^2 \text{s}^{-1}$)
ZurZn , ZntR _{apo}	6.24±0.62	0.939±0.057	0.0532±0.0074
ZurC88S , ZntR _{apo}	5.46±0.59	0.723±0.14	0.0411±0.0024
ZurZn , ZntR _{Zn}	5.04±0.23	0.903±0.04	0.0426±0.0042

10 **Supplementary Table 6** | Summary of all the extracted populations of the three different Zur^{mE} diffusion states.

[ZntR _{apo}] (nM)	[ZurZn] (nM)	A _{FD} (%)	A _{NB} (%)	A _{TB} (%)
0±0	99±34	15.5±0.3	52.1±1	32.4±0.6
	174±15	18.8±0.4	53.3±1.1	27.9±0.6
	313±84	22.7±0.5	50.2±1	27.1±0.5
	633±81	28.7±0.6	49.5±1	21.7±0.4
	998±117	29.6±0.6	54±1.1	16.4±0.3
	1644±363	28.3±0.6	57.3±1.1	14.4±0.3
	3573±873	31.2±0.6	60.3±1.2	8.5±0.2
27±8	142±41	23.1±0.5	51.2±1	25.7±0.5
	246±29	23.5±0.5	49.7±1	26.7±0.5
	380±53	25.9±0.5	49.6±1	24.4±0.5
	582±59	30±0.6	50.6±1	19.5±0.4
	779±59	28.1±0.6	56.4±1.1	15.5±0.3
	1217±376	36.4±0.7	51.8±1	11.9±0.2
	3425±954	33.6±0.7	59.2±1.2	7.2±0.1
114±15	366±95	22.1±0.4	55.4±1.1	22.5±0.4
	596±61	23.2±0.5	58.8±1.2	18.1±0.4
	800±58	23.6±0.5	60.3±1.2	16.1±0.3
	953±30	24.1±0.5	59.9±1.2	16±0.3
	1146±130	25.5±0.5	59.2±1.2	15.3±0.3
	1867±254	24.8±0.5	64.7±1.3	10.5±0.2
	3311±1010	30.4±0.6	62.2±1.2	7.5±0.1
316±19	531±115	31±0.6	50.5±1	18.5±0.4
	800±61	30.4±0.6	54.8±1.1	14.8±0.3
	950±29	27.3±0.5	58.5±1.2	14.2±0.3
	1164±135	29.7±0.6	57±1.1	13.3±0.3

1986±259	30±0.6	58.4±1.2	11.5±0.2
3373±797	24.5±0.5	64.3±1.3	11.2±0.2

[ZntR _{apo}] (nM)	[ZurC ₈₈₈] (nM)	A _{FD} (%)	A _{NB} (%)	A _{TB} (%)
10±8	89±9	22.4±0.4	32.6±0.7	45±0.9
	155±29	22.7±0.5	46.7±0.9	30.6±0.6
	219±6	29.6±0.6	41.8±0.8	28.6±0.6
	262±21	26.8±0.5	43.4±0.9	29.8±0.6
	398±86	30.6±0.6	45.3±0.9	24.1±0.5
	975±370	35.9±0.7	56.3±1.1	7.8±0.2

70±30	107±27	18.9±0.4	46.9±0.9	34.2±0.7
	260±74	24.1±0.5	53.5±1.1	22.4±0.4
	447±28	23.6±0.5	54.5±1.1	21.9±0.4
	599±58	24.2±0.5	62.1±1.2	13.6±0.3
	802±51	25±0.5	63.9±1.3	11.1±0.2
	1364±353	28.4±0.6	64.3±1.3	7.4±0.1
	2351±96	31.5±0.6	61.7±1.2	6.8±0.1
	3054±477	32.1±0.6	65.3±1.3	2.6±0.1

247±72	464±118	15.1±0.3	67.1±1.3	17.8±0.4
	675±47	18±0.4	66.8±1.3	15.2±0.3
	993±136	19.6±0.4	66.7±1.3	13.7±0.3
	1424±145	21.4±0.4	70.9±1.4	7.8±0.2
	1802±55	21.2±0.4	69.8±1.4	9±0.2
	2145±170	22.2±0.4	69.9±1.4	7.9±0.2
	3269±616	25.1±0.5	68.6±1.4	6.3±0.1

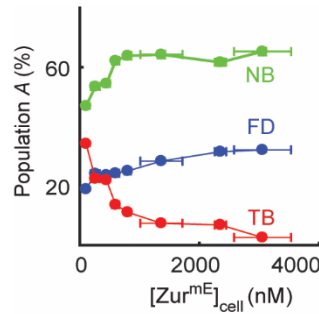
[ZntR _{Zn}] (nM)	[ZurZ _n] (nM)	A _{FD} (%)	A _{NB} (%)	A _{TB} (%)
27±7	78±11	14.6±0.3	33.7±0.7	51.8±1
	173±55	24.1±0.5	34.2±0.7	41.7±0.8
	345±30	27.5±0.6	30.2±0.6	42.3±0.8
	491±56	34±0.7	36.4±0.7	29.6±0.6
	698±56	42.4±0.8	23.4±0.5	34.2±0.7
	1187±391	49.9±1	32.1±0.6	18±0.4

64±3	136±40	8.9±0.2	29.3±0.6	61.8±1.2
	249±26	12.3±0.2	26.4±0.5	61.3±1.2
	379±56	17.5±0.3	31.8±0.6	50.7±1
	709±150	20.6±0.4	38.9±0.8	40.5±0.8
	1198±140	24.6±0.5	53.5±1.1	22±0.4
	1794±271	26.6±0.5	51.3±1	22.1±0.4
	3171±664	25.2±0.5	64.8±1.3	10±0.2

	149±35	14±0.3	19.3±0.4	66.7±1.3
	251±29	16.9±0.3	29±0.6	54.1±1.1
	368±43	17.7±0.4	28.3±0.6	53.9±1.1
131±5	517±42	20.3±0.4	38±0.8	41.7±0.8
	788±117	23.4±0.5	45.7±0.9	31±0.6
	1237±151	26.9±0.5	53.2±1.1	19.9±0.4
	1952±275	31.5±0.6	49.6±1	18.8±0.4
	3366±643	33±0.7	58.1±1.2	8.9±0.2
	178±74	13.5±0.3	28±0.6	58.5±1.2
	399±57	16.4±0.3	32.2±0.6	51.4±1
	543±29	17.2±0.3	30.9±0.6	51.9±1
407±48	690±58	16.3±0.3	39.4±0.8	44.3±0.9
	1123±221	26±0.5	43.8±0.9	30.2±0.6
	1945±285	29.6±0.6	53.9±1.1	16.5±0.3
	3664±771	30.7±0.6	57.9±1.2	11.4±0.2

3.2 *The fractional populations of Zur's three diffusion states show expected dependence on cellular [Zur]*

For all the conditions it was expectedly observed that the A_{FD} increases and A_{TB} decreases with increase in cellular [Zur]. Supplementary Fig. 15 shows an exemplary plot of fractional populations of the three diffusion states vs. Zur^{mE} concentration for the DZ-DZR-pZmE-pZRG115S strain expressing both the $ZntR_{apo}^G$ and Zur^{mE} proteins. These trends of A_{FD} and A_{TB} are expected because there are only a limited number of chromosomal binding sites for Zur and as [Zur] increases, there is more competition between the proteins for a limited number of tight binding sites, so each protein molecule spends larger fraction of its time in the free diffusion state than in the tight binding state.

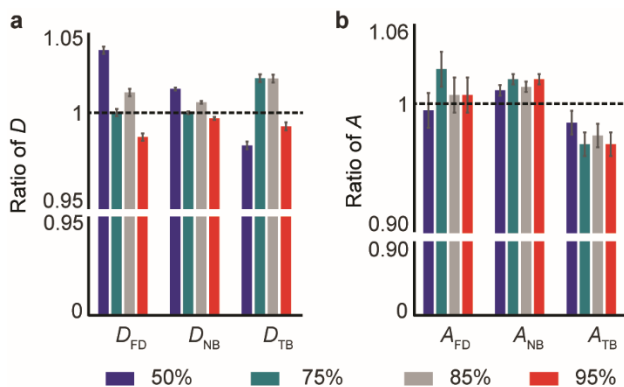


Supplementary Fig. 15 | Example plot of Zur protein concentration dependence of fractional populations of the TB, NB, and FD states, from the DZ-DZR-pZmE-pZRG115S strain expressing both the $ZntR_{apo}^G$ and Zur^{mE} proteins from plasmids (Supplementary Table 3). The data here consists of 4267 cells and did not sort the cells by $[ZntR_{apo}^G]$ in the cell. Source data are provided as a Source Data file.

3.3 *Bootstrap analysis shows statistical reliability of data*

A bootstrap analysis was performed by sampling randomly 50%, 75%, 85%, and 95% of the displacements lengths, to show that the extracted results from analyzing the CDF of the displacement lengths r are statistically reliable. The ratios of these extracted diffusion coefficients (D 's) and fractional

populations (A 's) over the results in Supplementary Table 5 and Table 6 clearly show that the extracted results from random sampling are all within 3% of the final results (Supplementary Fig. 16). This indicates that with just 50% of the experimental data we collected, we can determine diffusion coefficients and the corresponding fractional populations reliably, supporting the statistical saturation of our data.



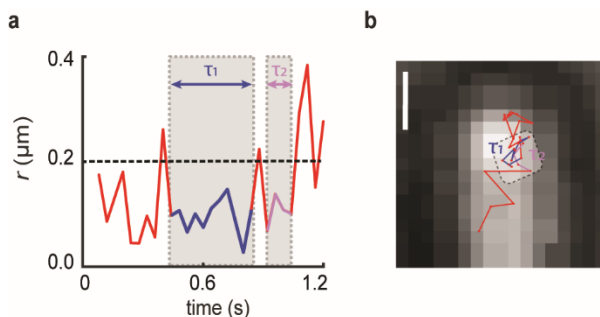
Supplementary Fig. 16 | Bootstrap analysis show that our experimental data are statistically saturated. Ratio of a, D's and b, A's by analyzing the CDF of a random subset of displacement lengths (i.e., 50%, 75%, 85%, and 95% of data) to the final results (100% of the data) in Supplementary Table 5 and Table 6. The ratios are all within the range of ~ 0.97 to ~ 1.03 , demonstrating that the results are within 3% of the final results and hence statistically saturated. Source data are provided as a Source Data file.

4 Extraction of kinetic and thermodynamic parameters for Zur-DNA interactions in cells

4.1 Extraction of k_{-1} , the apparent unbinding rate constant from the tight binding state

The quantitative analysis of Zur's unbinding kinetics from the TB sites on the chromosome follows our previous work², where the formulation and derivation of the kinetic model and its validation are described in detail. Here we briefly summarize the treatment.

Zur proteins that are bound to chromosomal sites tightly are almost immobile, giving rise to the TB state resolved (Supplementary Fig. 14; Fig. 2b) in the analysis of their displacement distributions with an effective diffusion coefficient $D_{TB} = 0.04 \mu\text{m}^2 \text{s}^{-1}$ and correspondingly small displacement length r between adjacent images (Supplementary Fig. 17b). Thresholding the displacement r -vs-time trajectories with an upper limit r_0 ($= 200 \text{ nm}$), which includes $>99.5\%$ of the TB state (Fig. 2b; Supplementary Fig. 17a) yields the microscopic residence times τ that are dominated by Zur tightly bound on DNA^{2,3}. This r_0 , the threshold displacement, was extracted from the displacement distribution (Fig. 2b), and it allows going from displacement distribution analysis to the residence time analysis. A residence time starts upon transition from larger values of r to below r_0 and terminates upon transitions above r_0 (or by photobleaching/blinking of the fluorescent mE tag) (Supplementary Fig. 17a). The distribution of microscopic residence times τ extracted from many displacement-vs-time trajectories can be analyzed to determine the apparent unbinding rate constant k_{-1} of Zur from the TB sites, using the 3-state kinetic model in Fig. 2c^{2,3}, while taking into account the photobleaching/blinking kinetics of the mE tag.

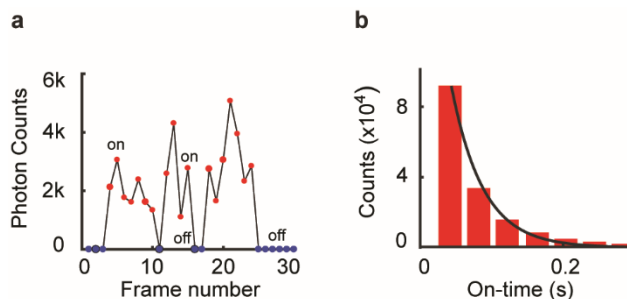


Supplementary Fig. 17 | Extraction of Zur's microscopic residence time on tight-binding sites on DNA. **a**, Exemplary displacement length r -vs-time trajectory of a single Zur^{mE} in an *E. coli* cell. The dashed horizontal line represents the r_0 threshold (~200 nm), below which >99.5% of TB state are included (vertical dashed line in Fig. 2b). A microscopic residence time τ begins when the displacement goes below r_0 and it ends when it goes above r_0 or when the tag photobleaches or photoblinks. Here in this example, τ_1 and τ_2 represent two residence times, denoted by the gray shade and blue/pink trajectory segments. **b**, The position-vs-time trajectory shows the residence sites corresponding to the two residence times denoted by the blue/pink trajectory segments in (a). The scale bar is 200 nm. Source data are provided as a Source Data file.

Experimentally, the microscopic residence time τ could also be terminated by a photobleaching/blinking event of the mE tag. The photobleaching/blinking rate constant k_{bl} can be determined from analyzing the distribution of the fluorescence on-times (Supplementary Fig. 18b) extracted from the corresponding fluorescence intensity trajectories of single-molecule tracking trajectories (Supplementary Fig. 18a). The distribution of on-time was fitted with Eq. S9, as we previously reported^{2,3}.

$$f_{on}(t) = N \exp\left(-k_{bl} \frac{T_{int}}{T_{tl}} t\right) \quad \text{Eq. S9}$$

Since we used time-lapse stroboscopic imaging, the apparent photobleaching/blinking rate constant from the fluorescence on-time distribution has been corrected by the ratio of the laser integration time T_{int} (= 4 ms) and the time-lapse T_{tl} (= 40 ms)^{2,3}. N is a normalization constant. The extracted k_{bl} , $230 \pm 10 \text{ s}^{-1}$, is consistent with the reported values under similar 561 nm excitations of the mE tag^{2,3,57,58}.



Supplementary Fig. 18 | Determination of the photobleaching and blinking rate constant k_{bl} . **a**, Exemplary fluorescence-vs-time trajectory of a mEos3.2 tagged Zur protein. The red dots represent frames where mEos3.2 fluorescence is detected and assigned as fluorescence-on frames. The blue dots correspondingly represent the off-frames with no protein fluorescence detection. **b**, The distribution of 165348 fluorescence on-times, fitted with Eq. S9 (black line), yields the k_{bl} (photobleaching/blinking rate constant). Source data are provided as a Source Data file.

Since diffusion is a probabilistic process at the microscopic level, freely diffusing or non-specifically bound proteins, which are expected to have large displacements in general ($D_{FD} = 5 \mu\text{m}^2 \text{ s}^{-1}$ and $D_{NB} = 0.82 \mu\text{m}^2 \text{ s}^{-1}$), have finite probabilities to have small displacement lengths as well. These will thus contribute to the microscopic residence times thresholded by r_0 . Thus, below r_0 , where >99.5% TB states are included, the contributions of the FD and NB states are 4.9% and 26.3% of their populations, respectively (Fig. 2b), and these need to be deconvoluted. To separate the contributions of FD and NB states from TB in the distribution of microscopic residence time, a survival probability $S(r_0, t)$, which is the probability for a protein at the origin to survive within a circle of radius r_0 within time t , was calculated, as we described previously^{2,3}.

$$S(r_0, t) = \left[1 - \exp\left(-\frac{r_0^2}{4Dt}\right) \right] \exp(-k_{eff}t) \quad \text{Eq. S10}$$

where D is the diffusion constant of the protein and k_{eff} is the summation of unbinding rate constants (applicable for the TB and the NB state only) and the effective photobleaching/blinking rate constant (i.e., $k_{\text{bl}} \frac{T_{\text{int}}}{T_{\text{tl}}}$). The overall survival probability for a Zur protein within r_0 is a linear combination of survival probabilities of each state weighted by its fractional population:

$$S_{\text{all}}(r_0, t) = A_{\text{FD}} S_{\text{FD}}(r_0, t) + A_{\text{NB}} S_{\text{NB}}(r_0, t) + A_{\text{TB}} S_{\text{TB}}(r_0, t) \quad \text{Eq. S11}$$

- 5 Then, the respective probability distribution function of the thresholded residence time τ , for the FD, NB, and TB states (i.e., $\varphi_{\text{FD}}(\tau)$, $\varphi_{\text{NB}}(\tau)$, and $\varphi_{\text{TB}}(\tau)$) can be obtained by taking a time-derivative of the survival probability (i.e., $\varphi(\tau) = -\frac{\partial S(t)}{\partial t} \Big|_{t=\tau}$):

$$\varphi_{\text{all}}(\tau) = A_{\text{FD}} \varphi_{\text{FD}}(\tau) + A_{\text{NB}} \varphi_{\text{NB}}(\tau) + A_{\text{TB}} \varphi_{\text{TB}}(\tau) \quad \text{Eq. S12}$$

$$\varphi_{\text{FD}}(\tau) = \left[\frac{r_0^2}{4D_{\text{FD}}\tau^2} \exp\left(-\frac{r_0^2}{4D_{\text{FD}}\tau}\right) + k_{\text{eff}}^{\text{FD}} \left(1 - \exp\left(-\frac{r_0^2}{4D_{\text{FD}}\tau}\right)\right) \right] \exp(-k_{\text{eff}}^{\text{FD}} \tau) \quad \text{Eq. S13}$$

$$\varphi_{\text{NB}}(\tau) = \left[\frac{r_0^2}{4D_{\text{NB}}\tau^2} \exp\left(-\frac{r_0^2}{4D_{\text{NB}}\tau}\right) + k_{\text{eff}}^{\text{NB}} \left(1 - \exp\left(-\frac{r_0^2}{4D_{\text{NB}}\tau}\right)\right) \right] \exp(-k_{\text{eff}}^{\text{NB}} \tau) \quad \text{Eq. S14}$$

$$\varphi_{\text{TB}}(\tau) = k_{\text{eff}}^{\text{TB}} \exp(-k_{\text{eff}}^{\text{TB}} \tau) \quad \text{Eq. S15}$$

Here, $k_{\text{eff}}^{\text{FD}} = k_{\text{bl}} \frac{T_{\text{int}}}{T_{\text{tl}}}$, $k_{\text{eff}}^{\text{NB}} = k_{\text{bl}} \frac{T_{\text{int}}}{T_{\text{tl}}} + k_{-2}$ and $k_{\text{eff}}^{\text{TB}} = k_{\text{bl}} \frac{T_{\text{int}}}{T_{\text{tl}}} + k_{-1}$ (see Fig. 2c for definition of rate constants).

- 10 k_{-2} is the unbinding rate constant from the NB sites. k_{-2} was extracted from the highest cellular concentration regime by fitting the residence time distribution with Eq. S16, in which A_{TB} is <10% and the $A_{\text{TB}}\varphi_{\text{TB}}(\tau)$ term in Eq. S12 becomes negligible:

$$\varphi_{\text{all}}(\tau) = A_{\text{FD}} \varphi_{\text{FD}}(\tau) + A_{\text{NB}} \varphi_{\text{NB}}(\tau) \quad \text{Eq. S16}$$

- 15 k_{-1} was extracted by fitting the residence time distribution from all the other concentration groups with Eq. S12 with predetermined D 's, A 's, k_{bl} , and k_{-2} . All determined rate constants are summarized in Supplementary Table 7. This method of extracting k_{-1} from the residence time distribution was further validated by using simulation data of multistate diffusion processes, as described in detail in our previous study³.

4.2 Extraction and summary of additional kinetics and thermodynamic parameters.

- 20 The Zur protein in a cell dynamically interconvert between the three states (FD, NB, and TB) at a timescale of tens to hundreds of ms (i.e., the apparent unbinding rate constant from tight-binding sites, k_{-1} , and the non-specific sites, k_{-2} , are on the order of 10^0 and 10^1 s^{-1} , and the corresponding binding rates are on the same order as well²), much faster than the protein lifetime in the cell and our total imaging time (~30 min to 1 hour), during which the cellular protein concentration largely remains constant. We can therefore

assume a quasi-equilibrium condition between these different states. By analyzing the relative populations of the three states, we can extract additional kinetic and thermodynamic parameters (Supplementary Table 7), for example, the binding rate constant (k_1), the binding affinity ($K_{D1} = k_0^{\text{off}}/k_1$) (Fig. 2c), etc., as we showed previously².

5 Using the quasi-equilibrium approximation between the TB, NB and FD states, we have the following relationships between the ratios of $[\text{PD}]_{\text{TB}}$ and $[\text{P}]_{\text{FD}}$ (Eq. S17), $[\text{PD}]_{\text{TB}}$ and $[\text{PD}]_{\text{NB}}$ (Eq. S18), and $[\text{PD}]_{\text{NB}}$ and $[\text{PD}]_{\text{FD}}$ (Eq. S19) as we derived previously², where $[\text{PD}]_{\text{TB}}$, $[\text{P}]_{\text{FD}}$, and $[\text{PD}]_{\text{NB}}$ are cellular protein concentrations of the TB, FD and NB states, which can be calculated from the fractional populations of A_{TB} , A_{FD} , and A_{NB} and the total cellular protein concentration.

$$\frac{[\text{PD}]_{\text{TB}}}{[\text{P}]_{\text{FD}}} = \frac{k_1[D_0]_{\text{TB}}}{k_{-1}} \frac{\partial \ln F_{\text{TB} \leftarrow \text{FD}}(x_{\text{TB} \leftarrow \text{FD}})}{\partial x_{\text{TB} \leftarrow \text{FD}}} \quad \text{Eq. S17}$$

$$\frac{[\text{PD}]_{\text{NB}}}{[\text{P}]_{\text{FD}}} = \frac{[D_0]_{\text{NB}}}{K_{D2} + [\text{P}]_{\text{FD}}} \quad \text{Eq. S18}$$

$$\frac{[\text{PD}]_{\text{TB}}}{[\text{PD}]_{\text{NB}}} = \frac{k_3[D_0]_{\text{TB}}}{k_{-3}([D_0]_{\text{NB}} - [\text{PD}]_{\text{NB}})} \frac{\partial \ln F_{\text{TB} \leftarrow \text{NB}}(x_{\text{TB} \leftarrow \text{NB}})}{\partial x_{\text{TB} \leftarrow \text{NB}}} \quad \text{Eq. S19}$$

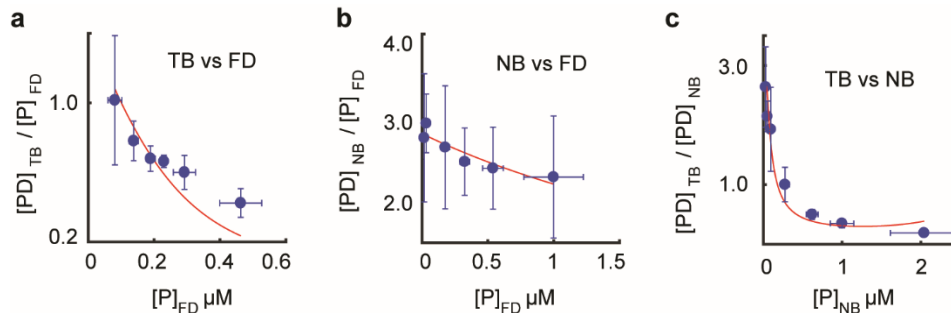
10

The expressions for: $x_{\text{TB} \leftarrow \text{FD}} = \frac{k_1[\text{P}]_{\text{FD}}}{k_{-1}}$, $x_{\text{TB} \leftarrow \text{NB}} = \frac{k_3[\text{PD}]_{\text{NB}}}{k_{-3}([D_0]_{\text{NB}} - [\text{PD}]_{\text{NB}})}$, $F_{\text{TB} \leftarrow \text{FD}}(x_{\text{TB} \leftarrow \text{FD}}) \equiv 1 + x_{\text{TB} \leftarrow \text{FD}} + x_{\text{TB} \leftarrow \text{FD}}^2 + \dots + x_{\text{TB} \leftarrow \text{FD}}^{n_0} = \sum_{i=0}^{n_0} x_{\text{TB} \leftarrow \text{FD}}^i$ and, $F_{\text{TB} \leftarrow \text{NB}}(x_{\text{TB} \leftarrow \text{NB}}) \equiv 1 + x_{\text{TB} \leftarrow \text{NB}} + x_{\text{TB} \leftarrow \text{NB}}^2 + \dots + x_{\text{TB} \leftarrow \text{NB}}^{n_0} = \sum_{i=0}^{n_0} x_{\text{TB} \leftarrow \text{NB}}^i$, were derived previously², where k_i and k_{-i} ($i = 1, 2, 3$) are the interconversion rate constants between the three diffusive states (Fig. 2c) and $[D_0]_{\text{TB}}$, and $[D_0]_{\text{NB}}$ are the cellular concentration of the TB and NB sites, respectively.

15

Using predetermined values of k_0^{off} , k_f , k_r , and K_m from the analysis of k_{-1} (Fig. 2 and Fig. 5) and a fixed value for the oligomerization number, n_0 (assumed to be 5 here), which is the maximum number of oligomers at a TB site (note we showed previously that for the range of values where $n_0 > 3$, the extracted kinetic parameters are not influenced significantly and approach asymptotic values within error bars²), we can fit $[\text{PD}]_{\text{TB}} / [\text{P}]_{\text{FD}}$ vs $[\text{P}]_{\text{FD}}$ with equation Eq. S17 (Supplementary Fig. 19a) and obtain the binding rate constant (k_1) and the binding affinity $K_{D1} (= k_0^{\text{off}}/k_1)$. Further, by fitting $[\text{PD}]_{\text{NB}} / [\text{P}]_{\text{FD}}$ vs $[\text{P}]_{\text{FD}}$ and $[\text{PD}]_{\text{TB}} / [\text{PD}]_{\text{NB}}$ vs $[\text{PD}]_{\text{NB}}$ with equation Eq. S18 and Eq. S19 (Supplementary Fig. 19b and c), we can obtain $K_{D2} (= k_{-2}/k_2)$, $[D_0]_{\text{NB}}$, $K_{D3} (= k_{-3}/k_3)$, and $[D_0]_{\text{TB}}$, respectively (Supplementary Table 7)².

20



25

Supplementary Fig. 19 | Example of relative population analysis for $\text{Zur}^{\text{mE}}_{\text{C88s}}$. a, $[\text{PD}]_{\text{TB}} / [\text{P}]_{\text{FD}}$ vs $[\text{P}]_{\text{FD}}$, b, $[\text{PD}]_{\text{NB}} / [\text{P}]_{\text{FD}}$ vs $[\text{P}]_{\text{FD}}$, and c, $[\text{PD}]_{\text{TB}} / [\text{PD}]_{\text{NB}}$ vs $[\text{P}]_{\text{NB}}$. The red lines are fits with Eq. S17 (a), Eq. S18 (b) and Eq. S19 (c). x, y error bars are s.d. Source data are provided as a Source Data file.

Supplementary Table 7 | Summary of extracted kinetic and thermodynamic parameters from live cell imaging experiments

	[ZntR _{apo}](nM)	k_0^{off} (s ⁻¹)	k_f (nM ⁻¹ s ⁻¹)	k_r (s ⁻¹)	K_m (nM)	k_1 (nM ⁻¹ s ⁻¹)*	K_{D1} (nM)*	[P] _{FD} ^{min} (nM)
Zur _{Zn}	0±0	16±1	0.016±0.004			0.85±0.16	19±4	
	27±8	15±1	0.019±0.002			0.24±0.02	62±6	
	114±15	12±2	0.041±0.007	n.o. †	n.o. †	0.06±0.01	207±58	n.o. †
	316±19	15±3	0.059±0.011			0.07±0.38	229±1287	
ZntR _{apo} acting on Zur _{Zn}		k_{bl} (s ⁻¹)	k_{-2} (s ⁻¹)	K_{D2} (nM)*		K_{D3} *	[D ₀] _{TB} (nM)*	[D ₀] _{NB} (nM)*
		225±3	7±0.4	550±210		0.043±0.003	966±124	1604±79
ZntR _{apo} acting on Zur _{Zn}		k_{f1} (nM ⁻¹ s ⁻¹)	k_{f2} (nM ⁻² s ⁻¹)	k_{r1} (s ⁻¹)		k_{r2} (nM ⁻¹ s ⁻¹)	K_{m1} (nM)	K_{m2}
		0.018±0.015	0.0003±0.0001	n.o. †		n.o. †	n.o. †	n.o. †
	[ZntR _{apo}](nM)	k_0^{off} (s ⁻¹)	k_f (nM ⁻¹ s ⁻¹)	k_r (s ⁻¹)	K_m (nM)	k_1 (nM ⁻¹ s ⁻¹)*	K_{D1} (nM)*	[P] _{FD} ^{min} (nM)
Zur _{C88S}	10±8	44±64	0.035±0.023	29±64	17±34	1.69±0.49	26±38	66±147
	70±30	49±46	0.047±0.013	37±46	25±40	1.92±0.41	25±25	86±148
	247±72	81±107	0.068±0.037	75±106	50±66	0.56±0.24	146±203	155±219
ZntR _{apo} acting on Zur _{C88S}		k_{bl} (s ⁻¹)	k_{-2} (s ⁻¹)	K_{D2} (nM)*		K_{D3} *	[D ₀] _{TB} (nM)*	[D ₀] _{NB} (nM)*
		227±3	9.5±0.1	3644±638		0.003±0.001	391±113	10234±1010
ZntR _{apo} acting on Zur _{C88S}		k_{f1} (nM ⁻¹ s ⁻¹)	k_{f2} (nM ⁻² s ⁻¹)	k_{r1} (s ⁻¹)		k_{r2} (nM ⁻¹ s ⁻¹)	K_{m1} (nM)	K_{m2}
		0.035±0.016	0.00014±0.00011	24.86±16.67		0.20±0.11	15.05±1.55	0.14±0.01
	[ZntR _{Zn}] (nM)	k_0^{off} (s ⁻¹)	k_f (nM ⁻¹ s ⁻¹)	k_r (s ⁻¹)	K_m (nM)	k_1 (nM ⁻¹ s ⁻¹)*	K_{D1} (nM)*	[P] _{FD} ^{min} (nM)
Zur _{Zn}	27±7	2±3	0.025±0.009			0.03±0.02	76±96	
	64±3	7±3	0.029±0.011			0.44±0.05	16±6	
	131±5	7±1	0.029±0.007	n.o. †	n.o. †	0.25±0.03	29±6	n.o. †
	407±48	9±3	0.024±0.009			0.21±0.02	41±13	
ZntR _{Zn} acting on Zur _{Zn}		k_{bl} (s ⁻¹)	k_{-2} (s ⁻¹)	K_{D2} (nM)*		K_{D3} *	[D ₀] _{TB} (nM)*	[D ₀] _{NB} (nM)*
		229±3	5.1±0.3	1747±1397		0.009±0.001	1175±216	3799±82

*n₀ = 5 (in the fitting routine)
†not observed

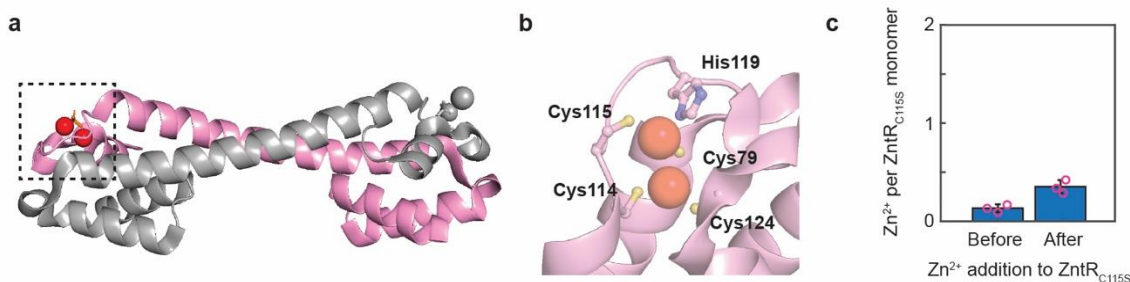
5 ZntR_{C115S} mutant has severely diminished Zn²⁺ binding affinity (lower than 10⁻⁷ M affinity), 8 orders of magnitude weaker than wild-type ZntR (~10⁻¹⁵ M)

10 In wild-type *E. coli* ZntR, two Zn²⁺ ions are bound to the protein through C114, C115, H119, C124, and C79 at each of the two binuclear Zn-binding sites in the dimeric protein (Supplementary Fig. 20 a-b)²⁰. Mutating either of these residues (e.g., C115S) deactivates ZntR, removing its capability of activating Zn efflux genes in the presence of Zn stress and approximating a constitutive apo-ZntR¹⁹. Therefore, we mutated C115 to serine to mimic the apo-form of ZntR; this ZntR_{C115S} mutant cannot activate the

transcription of the Zn-efflux transporter *zntA* in *E. coli* under Zn stress¹⁹, but can still bind DNA strongly inside cells with ~18 nM affinity³, both of which mimic the properties of the apo-form of ZntR.

To check whether ZntR_{C115S} is indeed incapable of bind Zn²⁺ significantly, we used the molecular sensor FluoZin-3 to perform Zn²⁺ binding assay under aerobic conditions²⁰ (Supplementary Methods 1.3.2), which becomes fluorescent upon binding Zn²⁺. We found that the as-purified ZntR_{C115S} contains ~0.13 Zn per monomer (Supplementary Fig. 20c, left). After adding Zn²⁺ (here a background of 10⁻⁷ M Zn²⁺ was kept in the buffer to ensure as much Zn²⁺ loading as possible into ZntR_{C115S} protein), the protein was found to contain ~0.35 Zn per monomer (Supplementary Fig. 20c, right), substantially lower than those of wild-type ZntR, which was found to contain 1 Zn per monomer under aerobic conditions and 2 Zn per monomer under anaerobic conditions²⁰. Therefore, the Zn²⁺ binding affinity of ZntR_{C115S} must be lower than 10⁻⁷ M (the background Zn²⁺ concentration in the Zn quantitation assay), which is at least 8 orders of magnitude weaker than the 10⁻¹⁵ M affinity of wild-type ZntR⁵⁹.

With its severely diminished Zn²⁺ binding affinity, we expect ZntR_{C115S} mutant to be dominantly in the apo form in cells, where Zn²⁺ concentration is extremely low (~femtomolar)⁵⁹. In addition, ZntR_{C115S} mutant is also expected to be dominantly in the apo form in our in vitro single-molecule FRET experiments, which used a background 200 nM Zn²⁺ in the solution. Even though some Zn²⁺ can bind to ZntR_{C115S} mutant in this buffer containing 200 nM Zn²⁺, excess Zn²⁺ is present in the buffer to fully metallate Zur (1 to 4 nM in protein concentration), which has ~10⁻¹⁶ M Zn²⁺ binding affinity, even 5 times higher than the wild-type ZntR⁵⁹. Thus, ZntR_{C115S} was not competing with Zur for Zn²⁺.



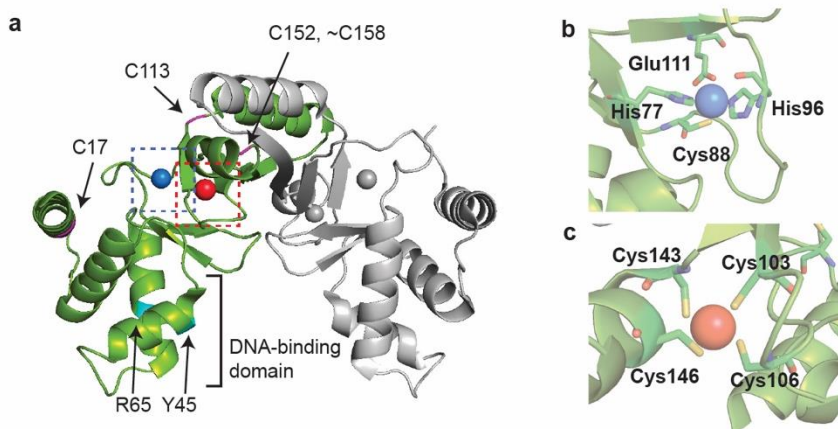
Supplementary Fig. 20 | **a**, Crystal structural of the homo-dimeric *E. coli* ZntR (PDB: 1Q08)⁶⁰, where the two ZntR monomers are colored pink and gray, and two Zn²⁺ are shown in red spheres at one of the two binuclear Zn-binding site. **b**, Zoomed-in image of zinc-binding residues at one binuclear site. **c**, As-purified ZntR_{C115S} was found to contain 0.13 ± 0.04 Zn/monomer before adding Zn²⁺. After ZntR_{C115S} was mixed with the excess ZnSO₄ followed by washing unbound Zn²⁺, 0.35 ± 0.07 Zn/monomer was bound to ZntR_{C115S} in the buffer containing a background of 0.1 μM Zn²⁺. The values are mean ± S.D. obtained from 3 times repeated experiments. Source data are provided as a Source Data file.

6 Protein labeling design for single-molecule FRET measurements *in vitro*

6.1 Selecting locations for fluorescent probe location on Zur based on Zur structure

For the dimeric *E. coli* Zur, each monomer contains nine cysteines. Five of these nine cysteines are essential for Zur's Zn-binding properties at two Zn-binding sites: one cysteine at the regulatory Zn-binding site (C88, Supplementary Fig. 21b) and the other four at the structural Zn-binding site (C103, C106, C143, C146; Supplementary Fig. 21c)^{13,59}. All these five essential cysteines can be protected by Zn from fluorophore labeling. The left four cysteines are non-conserved and are all exposed to the surface (C17, C113, C152, C158) on the basis of Zur's crystal structure¹³. In one variant, we used the natural C113 as the Cy5 labeling site, which is far away from Zur's DNA binding domain (Supplementary Fig. 21a), and thus

labeling at this position is expected to not interfere with Zur's DNA binding; the other three non-conserved cysteines (C17, C152, C158) were mutated to serine; we refer this labeled Zur variant (Cy5 at C113) as Zur^{Cy5} in this study unless otherwise noted. Alternatively, when we used C158 as a labeling site, other three cysteine residues (C17, C113, C152) were mutated to serines; we refer to this labeled variant as Zur^{Cy5-C158}.



5
Supplementary Fig. 21 | Fluorescent probe location on Zur based on Zur structure. **a**, Crystal structure of the homo-dimeric *E. coli* Zur (PDB: 4MTD¹³), where the two Zur monomers are colored green and gray, and two zinc ions are shown in blue and red spheres (four Zn²⁺ total per dimer). The positions of the four potential labeling sites, which are non-conserved cysteine residues (C17, C113, C152, C158), are colored in magenta and indicated by arrows (C158 location is unresolved in the structure and is denoted approximately together with the C152 location). DNA-binding domain is denoted on the green monomer, and the specific residues that make hydrogen bonds to the DNA bases (Y45, R65) are colored in cyan. In one variant, we used the natural C113 as the Cy5 labeling site, which is far away from Zur's DNA binding domain, and thus labeling at this position is expected to not interfere with Zur's DNA binding; the other three non-conserved cysteines (C17, C152, C158) were mutated to serine; we refer this labeled Zur variant (Cy5 at C113) as Zur^{Cy5}. **b-c**, Zoomed-in image of one cysteine (C88) at the regulatory site (b) and four cysteines (C103, C106, C143, C146) at the structural site (c). Source data are provided as a Source Data file.

6.2 Prediction of E_{FRET} values based on Zur-DNA complex structure

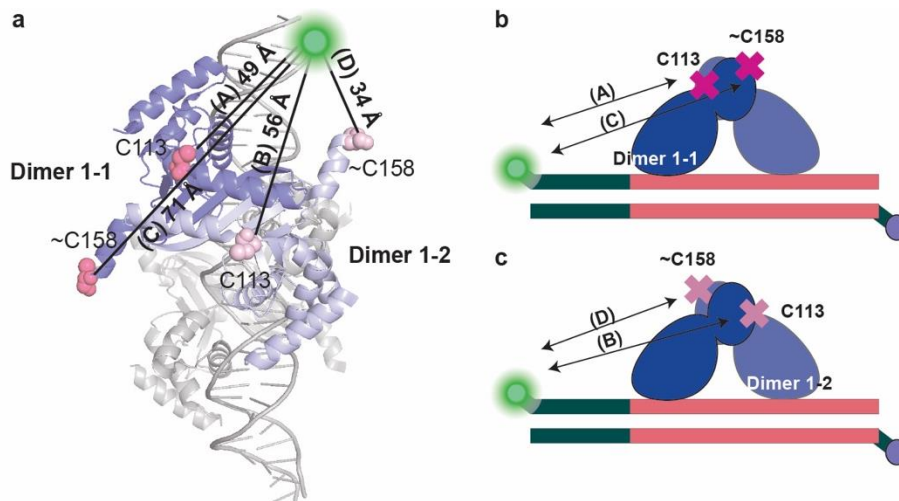
For a single Zur^{Cy5} dimer bound to 22-bp truncated DNA^{Cy3}, there are one FRET donor and one acceptor, forming a single FRET donor – acceptor system. In this system, E_{FRET} value can be estimated using Eq. S20⁶¹, where R_0 is the Förster radius (5.4 nm for Cy3-Cy5 pair⁶²), R is the distance measured between two anchoring positions of the dyes, and τ_D is the lifetime of the donor Cy3.

$$E = \frac{k_{D \rightarrow A}}{k_{D \rightarrow A} + \frac{1}{\tau_D}}, k_{D \rightarrow A} = \frac{1}{\tau_D} \left(\frac{R_0}{R}\right)^6 \quad \text{Eq. S20}$$

For Zur^{Cy5}, Cy5 is attached to the surface-exposed C113 of one monomer of the dimeric Zur. This labeling scheme makes a singly labeled Zur homodimer asymmetric, giving rise to two different binding orientations on DNA. Based on the crystal structure of holo Zur-DNA complex and our label position (Supplementary Fig. 22)¹³, the Cy3–Cy5 anchor-to-anchor distances in a Zur^{Cy5}–DNA complex are about (A) 49 Å and (B) 56 Å for the two binding orientations (Supplementary Fig. 22b and c) The corresponding E_{FRET} values are ~0.64 and ~0.45, respectively, and should be resolvable in an experimental E_{FRET} histogram (e.g., Fig. 3d and e). Experimentally, we observed two E_{FRET} states at ~0.65 and ~0.44 (Fig. 3d and e), in agreement with these predictions.

Similarly, a single dimer Zur^{Cy5-C158} binding to the truncated 22-bp DNA^{Cy3} should also give rise to two different binding orientations with distances of (C) 71 Å and (D) 34 Å (Supplementary Fig. 22b and c), and the corresponding E_{FRET} values should be ~0.16 and ~0.94, respectively. The distance is measured between dye labeling anchor to C152 of Zur due to structurally unresolved C158. Thus, the observed value

can be unmatched from the corresponding value but is expected to be farther away from Cy5 compared to C113. Experimentally, we observed two E_{FRET} states at ~ 0.41 and ~ 0.77 (Fig. 3f), in agreement with these predictions. All expected E_{FRET} values calculated by Eq. S20 are summarized in the ‘Expected E_{FRET} (1)’ column in Supplementary Table 8.



5

Supplementary Fig. 22 | Prediction of E_{FRET} value based on Zur-DNA complex structure for single Zur dimer binding. **a**, Crystal structure of two holo Zur dimers bound on DNA (PDB: 4MTD¹³), where one dimer Zur is colored purple (Dimer 1-1) and light purple (Dimer 1-2) for the two monomers, and the other dimer of Zur and DNA are colored gray. Two labeling positions (C113 and ~C158) are shown in pink and light pink spheres for Dimer 1-1 and Dimer 1-2, respectively. **b**, A cartoon showing that one homodimeric Zur is bound to 22-bp truncated DNA with labeling positions colored as pink crosses for Dimer 1-1. The Cy3–Cy5 anchor-to-anchor distances for each labeling position are (A) 49 Å and (C) 71 Å, and the corresponding E_{FRET} values are ~ 0.64 and ~ 0.16 , respectively. **c**, A cartoon showing that the same homodimeric Zur is bound to 22-bp truncated DNA as shown in (b) with labeling positions colored as light pink crosses for Dimer 1-2. The Cy3–Cy5 anchor-to-anchor distances for each labeling position are (B) 56 Å and (D) 34 Å, and the corresponding E_{FRET} values are ~ 0.45 and ~ 0.94 , respectively. Source data are provided as a Source Data file.

10

15

Alternatively, the FRET value can be predicted on the basis of our experimental calibration of observed E_{FRET} vs. Cy3–Cy5 distances, where Cy3–Cy5 are anchored on DNA structures with known inter-distances between the anchor points^{26,63,64}. Experimental data were fitted empirically using Eq. S21, where R_0 is the Förster radius (5.4 nm for Cy3–Cy5⁶²) and R is the distance measured between two phosphate backbone atoms corresponding to the anchoring position of the dyes.

20

$$E = \frac{k_{D \rightarrow A}}{k_{D \rightarrow A} + \frac{1}{\tau_D}}, k_{D \rightarrow A} = \frac{1}{\tau_D} \left(\frac{R_0 \beta}{R + \alpha} \right)^6 \quad \text{Eq. S21}$$

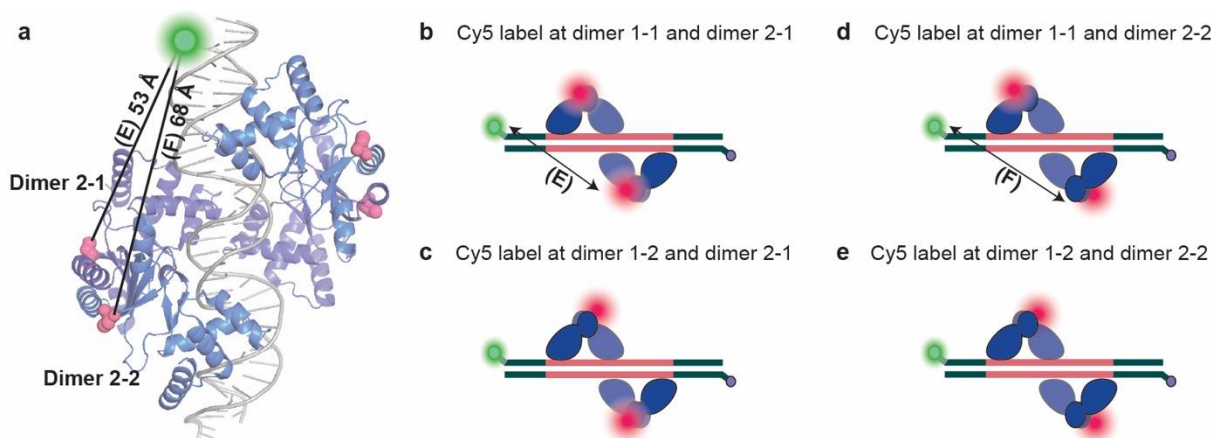
Here, α is the correction parameter for the additional distance due to the dye linker length and β is the correction parameter for deviation in R_0 because of the linker flexibility and the orientation of the dyes⁶⁵. Based on the fitting, $\alpha = 5.3 \pm 0.6$ nm and $\beta = 1.9 \pm 0.1$ ²⁶. Note the E_{FRET} value is not corrected for the relative fluorescence detection efficiencies and quantum yields of the dyes^{65,66}. Thus, the numerical values including α and β should be treated as empirical fitting parameters, not be interpreted literally despite their physical connections. This empirical calibration curve provides a direct correlation between an experimental observable (apparent E_{FRET}) and a distance quantity (anchor-to-anchor distance) that can be independently determined reliably using structural modeling. All expected E_{FRET} values calculated by Eq. S21 are summarized in the ‘Expected E_{FRET} (2)’ column in Supplementary Table 8.

25

For Zur^{Cy5} bound to 31-bp truncated DNA^{Cy3}, which encodes the complete two-dyad Zur binding box, two homodimeric Zur can bind to the DNA simultaneously, which makes 1 FRET donor – 2 FRET acceptor system. Here, E_{FRET} value can be calculated using Eq. S22⁶⁷.

$$E = \frac{k_{D \rightarrow A1} + k_{D \rightarrow A2}}{k_{D \rightarrow A1} + k_{D \rightarrow A2} + \frac{1}{\tau_D}}, k_{D \rightarrow A1} = \frac{1}{\tau_D} \left(\frac{R_0}{R_1} \right)^6, k_{D \rightarrow A2} = \frac{1}{\tau_D} \left(\frac{R_0}{R_2} \right)^6 \quad \text{Eq. S22}$$

5 For the two Zur dimers, one is at the dyad sequence proximal to the Cy3 label on DNA (Dimer 1), the other at the dyad distal to the Cy3 label (Dimer 2). Both dimers, each carrying a Cy5 label that breaks the dimer symmetry, can each give rise to two different binding orientations. The two possible orientations for the proximal dimer are shown in Supplementary Fig. 22a. For the distal dimer, its two orientations give a Cy5-Cy3 distance of (E) 53 Å and (F) 68 Å, respectively, as shown in Supplementary Fig. 23a. Two Zur dimer binding with two binding orientations each make four combinations of two-dimer-bound form (Supplementary Fig. 23b-e).



15 **Supplementary Fig. 23 | Prediction of E_{FRET} value based on Zur-DNA complex structure for two Zur dimer binding.** a, Crystal structure of two holo Zur dimer bound to DNA, where two dimers of Zur are colored purple and blue, respectively. Cy5 labeling positions (C113) are shown in pink spheres. Cy3-Cy5 anchor-to-anchor distances for Dimer 2 are indicated for the two monomers as (E) 53 Å and (F) 68 Å, and the corresponding E_{FRET} values are ~0.53 and ~0.20, respectively. b-e, Cartoons showing DNA-bound two Zur_{Zn}^{Cy5} dimers, each at one of the two dyads in two labeling orientations. Source data are provided as a Source Data file.

20 Again, the FRET values for two FRET acceptor system can be predicted on the basis of our experimental calibration of observed E_{FRET} vs. Cy3-Cy5 distances as well as one FRET acceptor system. R_0 and R_1 , R_2 are corrected with β and α , respectively based on Eq. S21. The expected FRET values and the experimentally observed FRET values are summarized in Supplementary Table 8; they show good agreements, especially in the ordering of E_{FRET} values among the different configurations.

Supplementary Table 8 / Expected E_{FRET} values calculated from structural model

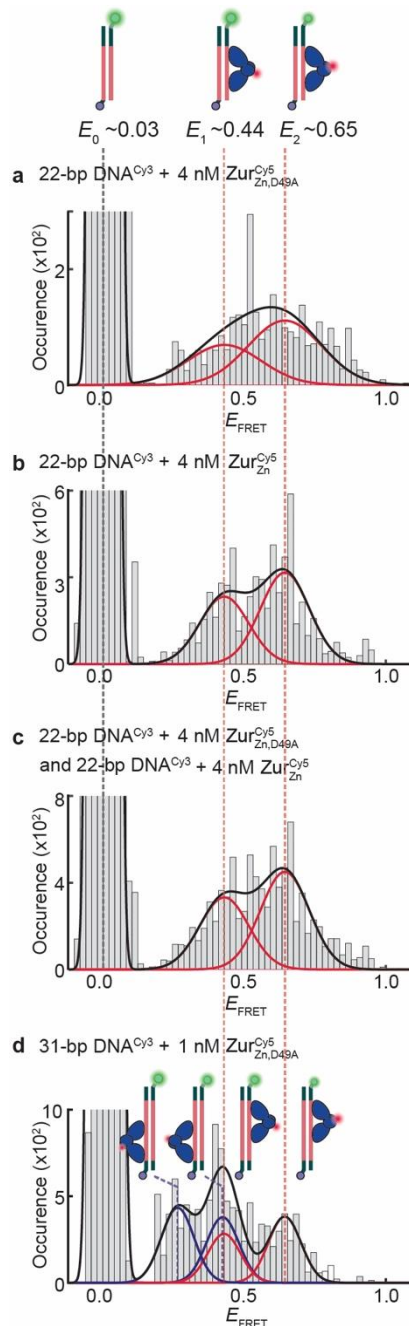
	Cy5 location	distance from Cy3 (Å)	Expected E_{FRET} (1)	Expected E_{FRET} (2)	Observed E_{FRET}
1 FRET acceptor	Dimer1-1 (C113)	49	0.64	0.51	0.65
	Dimer1-2 (C113)	56	0.45	0.41	0.44
	Dimer2-1 (C113)	53	0.53	0.45	0.43

	Dimer2-2 (C113)	68	0.20	0.27	0.27
	Dimer1-1 (~C158)	71	0.16	0.24	0.41
	Dimer1-2 (~C158)	34	0.94	0.73	0.77
	Dimer1-1, Dimer 2-1 (C113)	49, 53	0.74	0.65	0.80
2 FRET acceptor	Dimer1-1, Dimer 2-2 (C113)	49, 68	0.67	0.58	0.68
	Dimer1-2, Dimer 2-1 (C113)	56, 53	0.66	0.60	0.68
	Dimer1-2, Dimer 2-2 (C113)	56, 68	0.51	0.52	0.47

7 Procedures for Gaussian fitting to extract E_{FRET} values from the E_{FRET} histograms

As we described in Fig. 3d-e, in the main text, the binding of $\text{Zur}_{\text{Zn}, \text{D49A}}^{\text{Cy5}}$ and $\text{Zur}_{\text{Zn}}^{\text{Cy5}}$ onto the 22-bp truncated DNA^{Cy3} are expected to show the same E_{FRET} states because there is only one binding dyad site on the truncated DNA for Zur and the D49A mutation that removes the key inter-dimer salt-bridge interaction would not cause a significant difference between $\text{Zur}_{\text{Zn}, \text{D49A}}^{\text{Cy5}}$ and $\text{Zur}_{\text{Zn}}^{\text{Cy5}}$ (Fig. 3a, bottom). We extracted the E_{FRET} values for the two binding orientations of $\text{Zur}_{\text{Zn}, \text{D49A}}^{\text{Cy5}}$ on the truncated 22-bp DNA^{Cy3} via two-dimensional histogram analysis of lower vs. higher E_{FRET} values observed in the E_{FRET} trajectories (Fig. 3c; Supplementary Fig. 30a), which are 0.43 ± 0.13 and 0.69 ± 0.13 . With the same two-dimensional histogram analysis for $\text{Zur}_{\text{Zn}}^{\text{Cy5}}$ on the truncated DNA^{Cy3}, E_{FRET} values for its two binding orientations are 0.41 ± 0.08 and 0.66 ± 0.08 (Supplementary Fig. 30b), which, expectedly, are within error too, and thus the same as, those for $\text{Zur}_{\text{Zn}, \text{D49A}}^{\text{Cy5}}$. Therefore, to further improve data fitting reliability, we subsequently fitted two data sets globally with Gaussian functions sharing the peak positions (Supplementary Fig. 24a-b). Alternatively, we can also combine two data sets to have better statistics for fitting (Supplementary Fig. 24c). Both analyses gave the same three E_{FRET} values, ~ 0.03 , ~ 0.44 , and ~ 0.65 , for the free DNA state and the two binding orientations of the protein on the truncated DNA^{Cy3}.

We used these values to resolve E_{FRET} states for $\text{Zur}_{\text{Zn}, \text{D49A}}^{\text{Cy5}}$ bindings on the 31-bp DNA^{Cy3}, which have the complete two dyads of the Zur binding box (Fig. 3a, middle). One dyad binding site is proximal to the Cy3 label on DNA and is the same as the one in the 22-bp truncated DNA^{Cy3} (Fig. 3a, middle vs. bottom); so $\text{Zur}_{\text{Zn}, \text{D49A}}^{\text{Cy5}}$ binding to this proximal site is expected to show the same two E_{FRET} states as those from binding on the truncated DNA^{Cy3}. To resolve the rest E_{FRET} states, we fitted the E_{FRET} histogram with five Gaussian functions including (Supplementary Fig. 24d): a peak for the free DNA state near zero E_{FRET} value; two peaks whose positions and the amplitude ratio are taken from the interaction with the truncated DNA^{Cy3}; and two more peaks to account for the two orientations of $\text{Zur}_{\text{Zn}, \text{D49A}}^{\text{Cy5}}$ binding to the distal dyad site on the 31-bp DNA^{Cy3} whose positions and amplitudes are floated; the widths of the four DNA bound peaks are shared. The fitted results gave the additional two E_{FRET} values at ~ 0.43 and ~ 0.27 , respectively (Supplementary Fig. 24d). All these E_{FRET} values also agree with predictions from the Zur_{Zn} -DNA complex structure (Supplementary Table 8).



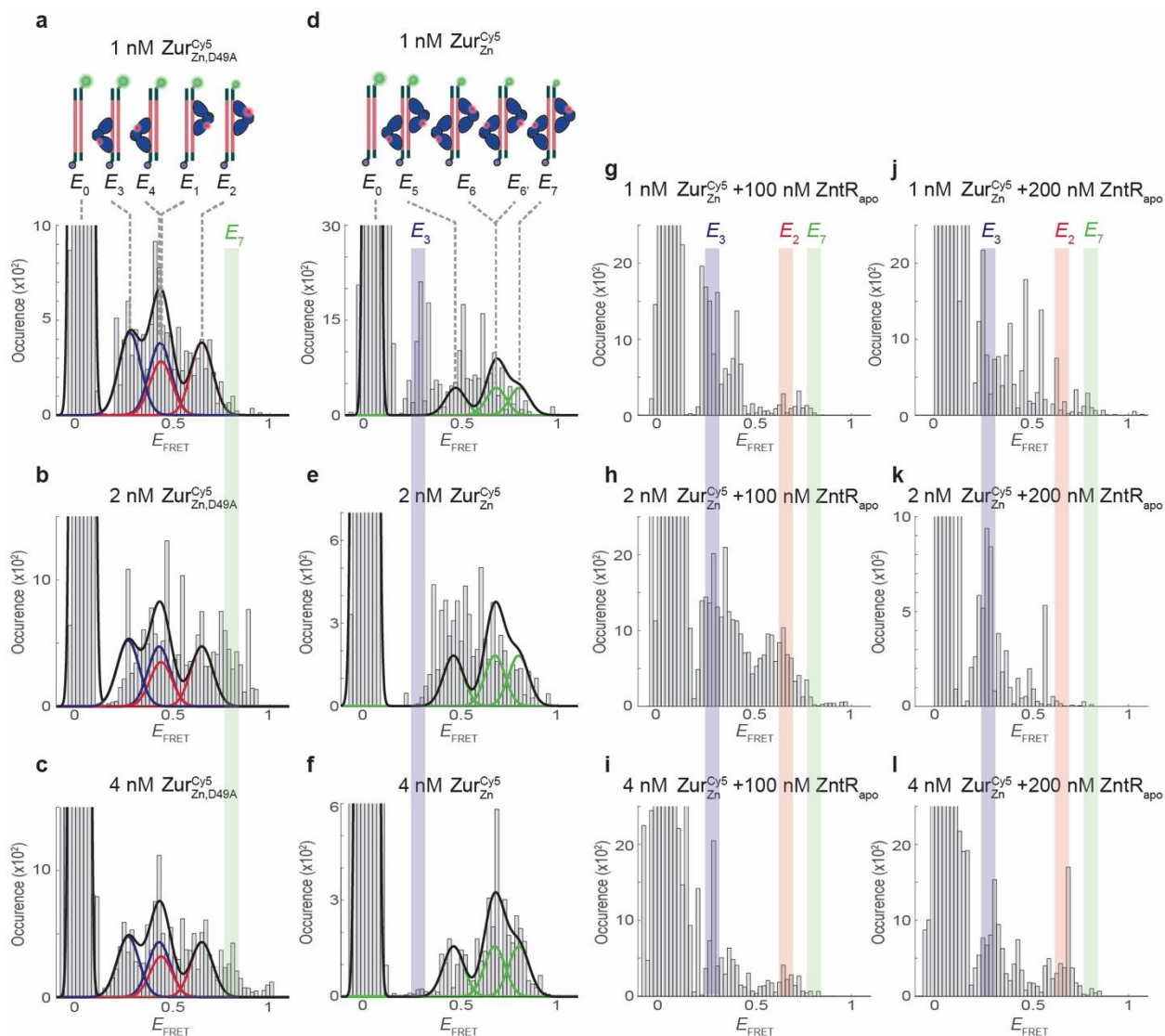
Supplementary Fig. 24 | **a**, Histograms of E_{FRET} trajectories of an immobilized 22-bp truncated DNA^{Cy3} interacting with Zur^{Cy5}_{Zn,D49A} (Cy5 at C113) (4 nM). **b**, Same as (a), but with Zur^{Cy5}_{Zn} (4 nM). Two histograms are globally fitted with Gaussian functions sharing the peak positions. **c**, Histograms of E_{FRET} trajectories of combined data of (a) and (b) and fitted with Gaussian functions. **d**, Same as (a), but with 31-bp DNA and 1 nM of Zur^{Cy5}_{Zn,D49A}; red and blue lines: Gaussian resolved fits; black lines: overall fits. Red dashed lines indicate two peaks that are assigned for Zur bindings on the proximal dyad to Cy3 with two orientations. (d) is the same figure as Fig. 4a in the main text. Cartoons show free DNA and DNA-bound Zur in two binding orientations. The FRET donor (green sphere) and acceptor (red sphere) are drawn on DNA and Zur at their approximate locations. Histograms are compiled from 260, 347, 607, 405 E_{FRET} trajectories for (a-d), respectively; bin size = 0.02. Source data are provided as a Source Data file.

8 ZntR_{apo} preferentially disrupts Zur_{Zn} binding at the dyad proximal to the Cy3 labeling position on DNA

When Zur_{Zn}^{Cy5} interacts with 31-bp DNA^{Cy3}, a single Zur_{Zn}^{Cy5} dimer can bind to either of the two dyads of Zur box on DNA and maximally two Zur_{Zn}^{Cy5} dimers can bind to the DNA simultaneously.

5 At a lower concentration of Zur_{Zn}^{Cy5} (e.g., 1 and 2 nM, Supplementary Fig. 25d-e), E_3 peak at ~ 0.2 is observed in E_{FRET} histogram, indicating that one-dimer-bound form occurs, as E_3 is characteristic of the one-dimer bound form (Supplementary Fig. 25a). Meanwhile, when Zur_{Zn}^{Cy5} concentration is increased to 4 nM (Fig. 4c; Supplementary Fig. 25f), E_3 peak is no longer observed, reflecting that Zur_{Zn}^{Cy5} dominantly occupy both dyad recognition sites. For all Zur_{Zn}^{Cy5} concentrations, upon introducing $ZntR_{apo}$, E_{FRET} histogram shows a significant E_3 peak (~ 0.2) (Supplementary Fig. 25g-l), while E_7 peak (at ~ 0.8 , which is characteristic of two-dimer bound form) almost disappears, indicating that $ZntR_{apo}$ disrupts Zur_{Zn} interactions with DNA, leading to the dominance of one-dimer bound form.

10 Interestingly, among the two dyads that Zur_{Zn}^{Cy5} binds, they are not equally populated in the presence of $ZntR_{apo}$. There are much higher population at a lower E_{FRET} value (E_3), which corresponds to Zur_{Zn}^{Cy5} binding at the dyad site distal to Cy3, than at a higher E_{FRET} value (E_2), which corresponds to Zur_{Zn}^{Cy5} binding at the dyad site proximal to Cy3 (Supplementary Fig. 25g-l). Therefore, $ZntR_{apo}$ preferentially disrupts Zur_{Zn}^{Cy5} binding at the proximal dyad to the Cy3 label. From sequence analysis of potential ZntR recognition sequence at the *znuBC* promoter that the 31-bp DNA is based upon, the most probable ZntR binding site overlaps more significantly with the Zur-binding dyad proximal to the Cy3 label position (Fig. 1b). We, therefore, conclude that $ZntR_{apo}$ facilitates the unbinding of incumbent Zur through recognizing the most probably binding sequences.



Supplementary Fig. 25 | ZntR_{apo} preferentially disrupts Zur_{Zn} binding at the dyad proximal to the Cy3 labeling position on DNA. Histograms of E_{FRET} trajectories of immobilized 31-bp DNA^{Cy3} interacting with different Cy5-labeled Zur constructs in the absence or presence of ZntR_{apo}. **a-c**, E_{FRET} histograms of 1 to 4 nM Zur^{Cy5}_{Zn,D49A} interacting with 31-bp DNA^{Cy3}. Blue/red lines are Gaussian-resolved protein-bound states; each color corresponds to the two orientations of one Zur^{Cy5}_{Zn,D49A} dimer at one of the two dyads of Zur binding box (red: E_1 and E_2 states at ~ 0.44 and ~ 0.65 , respectively; blue: E_3 and E_4 states at ~ 0.27 and 0.43 , respectively, as assigned in Fig. 4a in the main text). Black line: overall fits. **d-f**, E_{FRET} histograms of 1 to 4 nM Zur^{Cy5}_{Zn} interacting with the 31-bp DNA^{Cy3} (green: E_5 , E_6 (E_6), E_7 states at ~ 0.47 , ~ 0.68 , ~ 0.80 , respectively, as assigned in Fig. 4c in the main text). **g-l**, Same as (d-f), but in the presence of 100 nM (g-i) and 200 nM (j-l) ZntR_{apo}. E_7 state position (~ 0.8) is denoted as a green shade; it is an indicator of the two-dimer-bound form of Zur on DNA. E_3 state position (~ 0.3) is denoted as a blue shade; it is an indicator of the one-dimer-bound form of Zur binding at the dyad distal to the Cy3 labeling position on DNA. E_2 state position (~ 0.7) is denoted as a red shade; it is an indicator of one-dimer-bound form of Zur binding at the dyad proximal to the Cy3 labeling position on DNA. Here panel a, c, f, l are the same figures as Fig. 4a, b, c, d in the main text, respectively. Histograms are compiled from 405, 567, 433, 242, 334, 255, 133, 423, 147, 127, 86, 148 E_{FRET} trajectories for (a-i), respectively. Source data are provided as a Source Data file.

9 Summary of kinetic parameters for Zur^{Cy5}-31-bp DNA^{Cy3} interactions measured by *in vitro* smFRET

Supplementary Table 9 | Kinetic parameters for Zur^{Cy5}-31-bp DNA^{Cy3} interaction measured using *in vitro* smFRET

	[Zur] (nM)	[ZntR _{apo}] (nM)	Unbinding rate (s ⁻¹)	Binding rate (s ⁻¹)	k_0^{off} (s ⁻¹)	k_f (nM ⁻¹ s ⁻¹)	k_1 (nM ⁻¹ s ⁻¹)	k_{f1} (nM ⁻¹ s ⁻¹)	k_{f2} (nM ⁻² s ⁻¹)
Zur ^{Cy5} _{Zn}	1		1.90 ± 0.31	0.049 ± 0.024					
	2	0	2.53 ± 0.55	0.052 ± 0.015	1.20 ± 0.06	0.69 ± 0.04	0.023 ± 0.006		
	4		4.02 ± 1.01	0.108 ± 0.014					
Zur ^{Cy5} _{Zn}	1		3.05 ± 0.49	0.088 ± 0.024					
	2	100	2.88 ± 0.40	0.090 ± 0.012	1.57 ± 0.13	0.93 ± 0.47	0.006 ± 0.006	0.69 ± 0.02	0.006 ± 0.0004
	4		5.66 ± 0.57	0.102 ± 0.019					
Zur ^{Cy5} _{Zn}	1		2.33 ± 0.36	0.083 ± 0.033					
	2	200	4.99 ± 1.83	0.090 ± 0.034	0.55 ± 0.24	1.80 ± 0.11	0.087 ± 0.032		
	4		7.71 ± 0.64	0.311 ± 0.055					

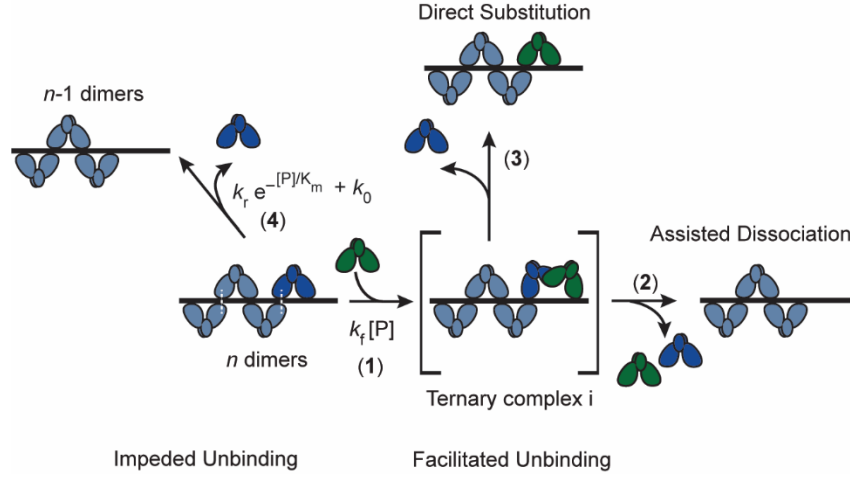
5 10 A through-DNA mechanism for Zur-DNA-ZntR_{apo} interactions and kinetic derivations

Our previous single-molecule tracking studies of single cells showed that the apparent unbinding rate constant k_{-1} of Zur from its tight-binding sites on DNA follows a biphasic, impeded-followed-by-facilitated unbinding behavior: it initially decreases with increasing cellular Zur concentration up to ~100 nM, reaching a minimum, and then increases at higher Zur concentrations². The impeded unbinding results from Zur oligomerization at its tight-binding site on DNA, in which the salt-bridge interactions between Zur dimers contribute to its oligomerization, which in turn stabilizes Zur on DNA and slows down its unbinding kinetics (Supplementary Fig. 26, Step 4).

When the cellular Zur concentration further increases, the facilitated unbinding pathways becomes more competitive, in which a freely diffusing Zur in the cytoplasm can bind partially to a recognition site occupied by an incumbent Zur to form a ternary protein-DNA complex *i* (Supplementary Fig. 26, Step 1); this ternary complex is made possible by the bivalent interactions between the homodimeric protein and the dyad-symmetric recognition sequence, in which each of the two dimeric proteins binds to half of the dyad sequence on the DNA. The unstable nature of this ternary complex subsequently leads to either the falling-off of both proteins from DNA, a so-called assisted dissociation pathway (Supplementary Fig. 26, Step 2), or a direct substitution of the incumbent protein by the incoming protein (Supplementary Fig. 26, Step 3). Both these pathways lead to an increase in the unbinding rate of the incumbent protein when the concentration of the protein in the cell increases, giving rise to the facilitated unbinding behavior.

Besides the Fur-family metalloregulator Zur, we also discovered the facilitated unbinding for the MerR-family metalloregulators CueR and ZntR in cells³, which also are dimeric proteins recognizing dyad symmetric sequences on DNA. For CueR, we further characterized this facilitated unbinding using *in vitro* single-molecule FRET experiments, which clearly showed the assisted dissociation and direct substitution pathways²³. Such facilitated unbinding was also observed *in vitro* for a number of other DNA-binding proteins, including a sequence-nonspecific DNA-binding protein (e.g., nucleoid-associated proteins, NAP), a sequence-neutral single-stranded DNA-binding protein (e.g., Replication protein A, RPA), and DNA

polymerases^{23,68,77–85,69–76}. Moreover, facilitated dissociation was also observed between heterotypic proteins on DNA (e.g., the unbinding of a human linker histone H1.0 (H1) bound to a nucleosome facilitated by a histone chaperone prothymosin α and the unbinding of NF- κ B facilitated by its specific inhibitor I κ B α), where the 2nd protein seems to only interact with the DNA-bound protein and not the DNA^{86–88}. Facilitated unbinding has also been investigated theoretically^{89–92}.



Supplementary Fig. 26 | Schematics of impeded unbinding (left, Step 4) for Zur and facilitated unbinding for Zur and ZntR/CueR (right, Steps 1, 2 and 3). Freely diffusing proteins are shown in green. Incumbent proteins on DNA are shown in blue. [P]: concentration of Zur or ZntR protein.

For the impeded-followed-by-facilitated unbinding behavior of Zur, we have previously derived the following equation to quantitatively describe Zur's apparent 1st-order unbinding rate constant k_{-1} from a tight-binding site as a function of its cellular concentration of freely diffusing component²:

$$k_{-1} = k_0^{\text{off}} + k_r \left(e^{-\frac{[\text{Zur}]}{K_m}} - 1 \right) + k_f [\text{Zur}] \quad \text{Eq. S23}$$

where k_{-1} is the apparent 1st-order apparent unbinding rate constant; k_f is a 2nd-order facilitated unbinding rate constant; $k_0^{\text{off}} = k_0 + k_r$, where k_0 is the intrinsic protein unbinding rate constant; k_r is a 1st-order impeded unbinding rate constant; and K_m , is the effectively affinity constant (in concentration units) of Zur oligomerization on DNA.

$$K_m \equiv \frac{k_0^{\text{off}}}{k_1 (1 - \alpha)} \equiv \frac{k_0 + k_r}{k_1 (1 - \alpha)} \quad \text{Eq. S24}$$

where, k_1 is the binding rate constant to the tight-binding site on DNA and α ($0 < \alpha < 1$) is a factor by which the impeded unbinding rate constant k_r is attenuated².

10.1 Empirical kinetic equation for ZntR_{apo}-induced enhancement of Zur's facilitated unbinding and diminishment of Zur's impeded unbinding

In this study we have uncovered the effects of ZntR_{apo} on Zur unbinding and our results show that k_r and k_f of Zur both depend on [ZntR_{apo}] linearly with a positive slope and intercept (Fig. 2f, Fig. 4f and Fig. 5c and e). Thus, we can replace k_r and k_f in Eq. S23 as:

$$k_r = k_{r2} [\text{ZntR}_{\text{apo}}] + k_{r1} \quad \text{Eq. S25}$$

$$k_f = k_{f2}[\text{ZntR}_{\text{apo}}] + k_{f1} \quad \text{Eq. S26}$$

where k_{r1} , k_{r2} , k_{f1} , and k_{f2} are empirical constants. Eq. S23 becomes:

$$k_{-1} = k_0 + (k_{r2}[\text{ZntR}_{\text{apo}}] + k_{r1})\left(e^{-\frac{[\text{Zur}]}{K_m}}\right) + (k_{f2}[\text{ZntR}_{\text{apo}}] + k_{f1})[\text{Zur}] \quad \text{Eq. S27}$$

Eq. S27 empirically describes the apparent unbinding rate constant k_{-1} of Zur as a function of $[\text{Zur}]$ and $[\text{ZntR}_{\text{apo}}]$ in the cell. Below we will use the mechanistic model from Fig. 5F to derive this relationship between k_{-1} and $[\text{Zur}]$ and $[\text{ZntR}_{\text{apo}}]$.

- 5 Since K_m is related to k_r linearly (Eq. S24), which in turn is linearly dependent on $[\text{ZntR}_{\text{apo}}]$ (Eq. S25), K_m is therefore also dependent on $[\text{ZntR}_{\text{apo}}]$ linearly, as follows:

$$K_m = \frac{k_0 + (k_{r2}[\text{ZntR}_{\text{apo}}] + k_{r1})}{k_1(1-\alpha)} \quad \text{Eq. S28}$$

- 10 This linear dependence of K_m on $[\text{ZntR}_{\text{apo}}]$ is indeed observed (Fig. 5e dashed line, right). We thus can write the following empirical relationship:

$$K_m = K_{m2}[\text{ZntR}_{\text{apo}}] + K_{m1} \quad \text{Eq. S29}$$

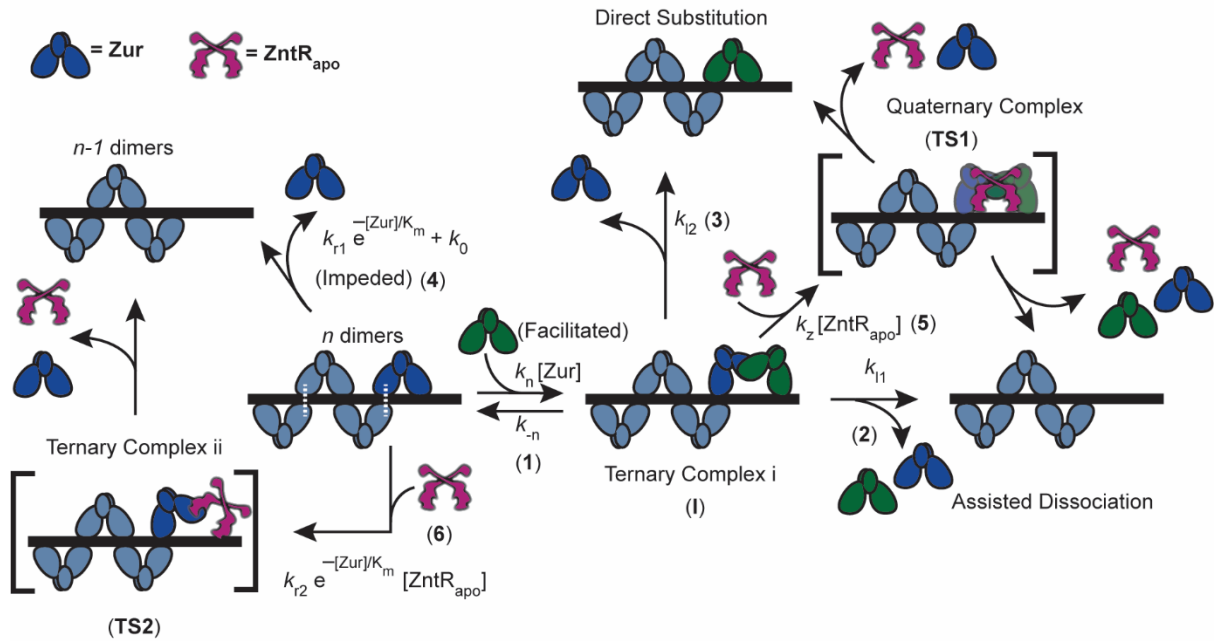
where the slope K_{m2} equals $\frac{k_{r2}}{k_1(1-\alpha)}$, and the intercept K_{m1} equals $\frac{k_0+k_{r1}}{k_1(1-\alpha)}$.

- 15 By fitting k_f vs $[\text{ZntR}_{\text{apo}}]$ (Fig. 2f, Fig. 4f and Fig. 5c) with Eq. S26, we can extract the slope k_{f2} and intercept k_{f1} . Similarly, by fitting k_r vs $[\text{ZntR}_{\text{apo}}]$ (Fig. 5e solid line, left) with Eq. S25, we can obtain the slope k_{r2} and intercept k_{r1} . Finally, by fitting K_m vs $[\text{ZntR}_{\text{apo}}]$ (Fig. 5e dashed line, right) with Eq. S29, we can obtain the slope K_{m2} and intercept K_{m1} . All these fitted parameters are summarized in Supplementary Table 7 and Table 9.

10.2 Kinetic derivation and justification of the mechanistic model for ZntR_{apo} -dependent Zur unbinding from DNA

- 20 On the basis of the observed $[\text{Zur}]$ and $[\text{ZntR}_{\text{apo}}]$ dependence of Zur's unbinding kinetics, which are empirically described by Eq. S27 above, we proposed the mechanistic scheme of Zur unbinding, in which ZntR_{apo} can act directly on DNA-bound Zur (Fig. 5F; Supplementary Fig. 27). Starting from oligomeric Zur dimers bound at a tight-binding site (i.e., n dimers), Zur can unbind spontaneously (k_0 component in Step 4) and its unbinding can also be impeded by its oligomerization on DNA due to the extra
- 25 stability from inter-dimer interactions (the $k_{r1} e^{-\frac{[\text{Zur}]}{K_m}}$ component in Step 4), as we previously formulated². In the presence of free Zur and ZntR_{apo} in the surrounding, this mechanism can proceed by the formation of one ternary complex intermediate, i (Step 1), and two transition states, TS1 (a quaternary complex) and TS2 (a ternary complex ii). The formation of ternary complex intermediate i, using an incoming freely diffusing cytoplasmic Zur (Step 1), can lead to Zur's assisted dissociation and direct substitution (Steps 2
- 30 and 3), accounting for the facilitated unbinding of Zur that we previously discovered². The formation of the heteromeric TS1 quaternary complex, using an incoming free ZntR_{apo} , accounts for ZntR_{apo} -enhanced facilitated unbinding of Zur (Step 5), while the formation of the heteromeric TS2 ternary complex ii, also

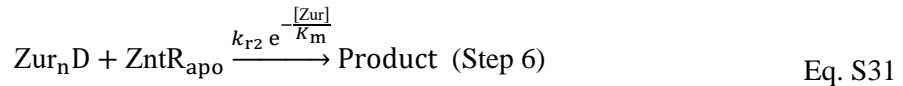
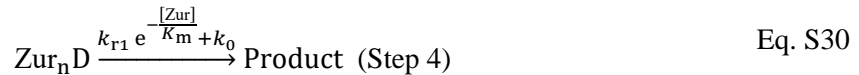
using an incoming free $ZntR_{apo}$ (Step 6), accounts for $ZntR_{apo}$ dependent diminishment of Zur's impeded unbinding process.



5 **Supplementary Fig. 27 | A “through-DNA” mechanistic model for $ZntR_{apo}$ -dependent Zur unbinding kinetics.** Starting with n oligomerized Zur dimers at a tight-binding site on DNA, the unbinding of an incumbent Zur protein (dark blue) can be facilitated by a freely diffusing Zur (dark green) through the formation of a ternary complex i (Step 1), leading to assisted dissociation (Step 2) or direct substitution (Step 3); this facilitated unbinding of Zur can be enhanced by $ZntR_{apo}$ through the formation of a heteromeric quaternary complex (Step 5). The oligomer-induced impedance of Zur unbinding (Step 4) can be weakened by $ZntR_{apo}$ through the formation of a heteromeric ternary complex ii (Step 6), leading to faster Zur unbinding as well. White dashed lines denote salt bridge interactions between Zur dimers. The associated rate constants, k 's, are denoted on the respective kinetic steps in the mechanism.

15 The mechanism in Supplementary Fig. 27 can be separated into the following kinetic processes with their associated rate constants:

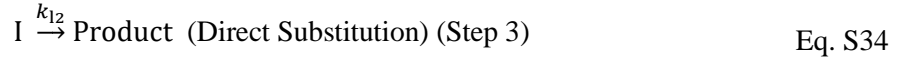
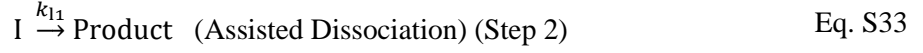
Impeded and spontaneous unbinding pathways of Zur and the dependence on $[ZntR_{apo}]$



where $Zur_n D$ represents n Zur dimers bound at a tight-binding site on DNA (i.e., D). In step 4 (Eq. S30), the rate constant is $k_{r1} e^{-\frac{[Zur]}{K_m} + k_0}$, where K_m is the effective dissociation constant of the protein oligomer, as we derived in our previous work to account for the impeded unbinding of Zur from DNA².

20 Facilitated unbinding pathways of Zur and its enhancement by $[ZntR_{apo}]$





Eq. S33 and Eq. S34 can be combinedly written as



where, $k_1 = k_{11} + k_{12}$. For the ZntR_{apo}-enhanced facilitated unbinding:



Taking into account Eq. S30 – Eq. S36 , we can write the following rate equations:

$$\frac{d[I]}{dt} = k_n[\text{Zur}_n\text{D}][\text{Zur}] - k_{-n}[I] - k_1[I] - k_z[I][\text{ZntR}_{\text{apo}}] \quad \text{Eq. S37}$$

$$\frac{d[\text{Products}]}{dt} = k_{r1} e^{-\frac{[\text{Zur}]}{K_m}} [\text{Zur}_n\text{D}] + k_{r2} e^{-\frac{[\text{Zur}]}{K_m}} [\text{Zur}_n\text{D}][\text{ZntR}_{\text{apo}}] + k_0 [\text{Zur}_n\text{D}] + k_1 [I] + k_z [I][\text{ZntR}_{\text{apo}}] \quad \text{Eq. S38}$$

Here “Products” represent all product species that resulted from the Zur unbinding from tight-binding sites via all possible pathways. Assuming steady state approximation to Eq. S37:

$$\frac{d[I]}{dt} = 0$$

We then have:

$$k_n[\text{Zur}_n\text{D}][\text{Zur}] - k_{-n}[I] - k_1[I] - k_z[I][\text{ZntR}_{\text{apo}}] = 0$$

$$k_{-n}[I] + k_1[I] + k_z[I][\text{ZntR}_{\text{apo}}] = k_n[\text{Zur}_n\text{D}][\text{Zur}]$$

$$\therefore [I] = \frac{k_n[\text{Zur}_n\text{D}][\text{Zur}]}{k_{-n} + k_1 + k_z[\text{ZntR}_{\text{apo}}]} \quad 10$$

Replacing the expression for [I] in Eq. S38

$$\frac{d[\text{Products}]}{dt} = k_{r1} e^{-\frac{[\text{Zur}]}{K_m}} [\text{Zur}_n\text{D}] + k_{r2} e^{-\frac{[\text{Zur}]}{K_m}} [\text{Zur}_n\text{D}][\text{ZntR}_{\text{apo}}] + k_0 [\text{Zur}_n\text{D}] + k_1 \frac{k_n[\text{Zur}_n\text{D}][\text{Zur}]}{k_{-n} + k_1 + k_z[\text{ZntR}_{\text{apo}}]} + k_z \frac{k_n[\text{Zur}_n\text{D}][\text{Zur}]}{k_{-n} + k_1 + k_z[\text{ZntR}_{\text{apo}}]} [\text{ZntR}_{\text{apo}}] \quad \text{Eq. S39}$$

To simply, we can make the approximation that the Ternary Complex I is not a stable species and its dissociation is fast compared with the formation of the heteromeric Quaternary Complex TS1, i.e., $k_{-n} \gg k_z[\text{ZntR}_{\text{apo}}]$. Moreover, the direct substitution rate constant k_{12} (Step 3) is effectively the same as that k_{-n} , and thus the same approximation gives $k_{12} \gg k_z[\text{ZntR}_{\text{apo}}]$ and therefore $k_1 = k_{11} + k_{12} \gg k_z[\text{ZntR}_{\text{apo}}]$. Consequently, the dominator in the 4th and 5th term in Eq. S39 can be simplified to:

$$\begin{aligned} \frac{d[\text{Products}]}{dt} = & k_{r1} e^{-\frac{[Zur]}{K_m}} [Zur_n D] + k_{r2} e^{-\frac{[Zur]}{K_m}} [Zur_n D] [ZntR_{apo}] + k_0 [Zur_n D] \\ & + k_l \frac{k_n [Zur_n D]}{k_{-n} + k_l} [Zur] + k_z \frac{k_n [Zur_n D]}{k_{-n} + k_l} [Zur] [ZntR_{apo}] \end{aligned} \quad \text{Eq. S40}$$

Also, from the three-state model (Fig. 2c) using which we extracted the apparent unbinding rate constant k_{-1} , we also have the following,

$$\frac{d[\text{Products}]}{dt} = k_{-1} [Zur_n D] \quad \text{Eq. S41}$$

Equating Eq. S40 and Eq. S41, we have the following:

$$\begin{aligned} k_{-1} = & k_{r1} e^{-\frac{[Zur]}{K_m}} + k_{r2} e^{-\frac{[Zur]}{K_m}} [ZntR_{apo}] + k_0 + k_l \frac{k_n}{k_{-n} + k_l} [Zur] \\ & + k_z \frac{k_n}{k_{-n} + k_l} [Zur] [ZntR_{apo}] \end{aligned} \quad \text{Eq. S42}$$

Replacing in Eq. S42 by:

$$k_{f2} \equiv k_z \frac{k_n}{k_{-n} + k_l} \quad \text{and} \quad k_{f1} \equiv k_l \frac{k_n}{k_{-n} + k_l}$$

5 we can arrive at the following equation, which has the same form as the empirical Eq. S27,

$$k_{-1} = k_0 + (k_{r2} [ZntR_{apo}] + k_{r1}) \left(e^{-\frac{[Zur]}{K_m}} \right) + (k_{f2} [ZntR_{apo}] + k_{f1}) [Zur] \quad \text{Eq. S43}$$

11 Additional data and figures

a

E coli Zur WT: MEKTTTQELL AQA EKICAQR NVRLTPQRLE VLRLMSLQDG AISAYDLLDL
 Zur variant 1: MEKTTTQELL AQA EKISAQR NVRLTPQRLE VLRLMSLQDG AISAYDLLDL
 Zur variant 2: MEKTTTQELL AQA EKISAQR NVRLTPQRLE VLRLMSLQDG AISAYDLLAL
 Zur variant 3: MEKTTTQELL AQA EKISAQR NVRLTPQRLE VLRLMSLQDG AISAYDLLDL

E coli Zur WT: LREAEPQAKP PTVYRALDFL LEQGFVHKVE STNSYVLCHL FDQPTHTSAM
 Zur variant 1: LREAEPQAKP PTVYRALDFL LEQGFVHKVE STNSYVLCHL FDQPTHTSAM
 Zur variant 2: LREAEPQAKP PTVYRALDFL LEQGFVHKVE STNSYVLCHL FDQPTHTSAM
 Zur variant 3: LREAEPQAKP PTVYRALDFL LEQGFVHKVE STNSYVLCHL FDQPTHTSAM

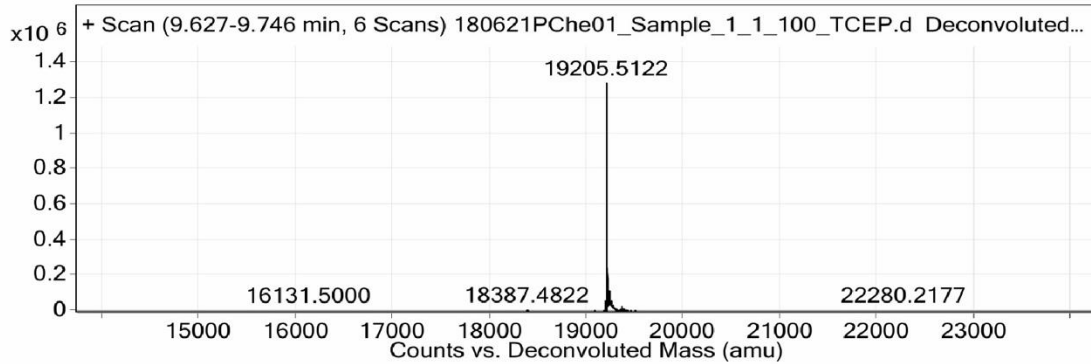
E coli Zur WT: FICDRCGAVK EECAEGVEDI MHTLAAKMGF ALRHNVIEAH GLCAACVEVE
 Zur variant 1: FICDRCGAVK EECAEGVEDI MHTLAAKMGF ALRHNVIEAH GLCAACVEVE
 Zur variant 2: FICDRCGAVK EECAEGVEDI MHTLAAKMGF ALRHNVIEAH GLCAACVEVE
 Zur variant 3: FICDRCGAVK EESAEGVEDI MHTLAAKMGF ALRHNVIEAH GLCAACVEVE

E coli Zur WT: ACRHPEQCQH DHSVQVKKKP R
 Zur variant 1: ASRHPEQSQH DHSVQVKKKP R
 Zur variant 2: ASRHPEQSQH DHSVQVKKKP R
 Zur variant 3: ASRHPEQCQH DHSVQVKKKP R

Zur variant 1 for Zur^{Cy5-C113}: E coli Zur (C17S, C152S, C158S)- expected mass 19205.6 Da
 Zur variant 2 for Zur^{Cy5-C113}_{D49A}: E coli Zur (C17S, C152S, C158S, D49A)- expected mass 19161.6 Da
 Zur variant 3 for Zur^{Cy5-C158}: E coli Zur (C17S, C113S, C152S)- expected mass 19205.6 Da

b

Spectrum



c

PCh01 (100%), 19,161.6 Da
 Zinc uptake regulation protein (Zur), E. coli, C17S, D49A, C152S, C158S [mutant of P0AC51 (ZUR_ECOLI)]
 79 exclusive unique peptides, 159 exclusive unique spectra, 578 total spectra, 156/171 amino acids (91% coverage)

MEKTTTQELL	AQA EKISAQR	NVRLTPQRLE	VLRLMSLQDG	AISAYDLLAL
LREAEPQAKP	PTVYRALDFL	LEQGFVHKVE	STNSYVLCHL	FDQPTHTSAM
FICDRCGAVK	EECAEGVEDI	MHTLAAKMGF	ALRHNVIEAH	GLCAACVEVE
ASRHPEQSQH	DHSVQVKKKP	R		

d

PCh02 (100%), 19,205.6 Da
 Zinc uptake regulation protein, E. coli, C113S, C152S [mutant of P0AC51 (ZUR_ECOLI)]
 32 exclusive unique peptides, 81 exclusive unique spectra, 247 total spectra, 168/171 amino acids (98% coverage)

MEKTTTQELL	AQA EKISAQR	NVRLTPQRLE	VLRLMSLQDG	AISAYDLLDL
LREAEPQAKP	PTVYRALDFL	LEQGFVHKVE	STNSYVLCHL	FDQPTHTSAM
FICDRCGAVK	EESAEGVEDI	MHTLAAKMGF	ALRHNVIEAH	GLCAACVEVE
ASRHPEQCQH	DHSVQVKKKP	R		

Supplementary Fig. 28 | Identities of recombinant Zur variants are confirmed with mass spectrometry. **a**, Amino-acid sequences of *E. coli* Zur and our designed variants. The specific mutant residues and expected mass for each variant are written below the sequences. **b**, Mass of Zur variant 1 is determined by ESI-TOF. The protein mass agrees with the expected value. **c-d**, Amino acid sequences of Zur variant 2 (c) and 3 (d) are determined by LC-MS/MS. The results are visualized via the Scaffold software (Proteome Software). Amino-acids matched to a MS/MS spectrum are highlighted (yellow/green). Amino-acids in green have a post-translational modification. Each variant is observed with >90% coverage and all mutation residues circled in red are confirmed. Source data are provided as a Source Data file.

5

a

E. coli ZntR WT: MYRIGELAKM AEVTPDTIRY YEKQQMMEHE VRTEGGFRLY TESDLQRLKF
 ZntR variant 1: MYRIGELAKM AEVTPDTIRY YEKQQMMEHE VRTEGGFRLY TESDLQRLKF

E. coli ZntR WT: IRHARQLGFS LESIRELLSI RIDPEHHTCQ ESKGIVQERL QEVEARIAEL
 ZntR variant 1: IRHARQLGFS LESIRELLSI RIDPEHHTCQ ESKGIVQERL QEVEARIAEL

E. coli ZntR WT: QSMQRS LQRL NDACCGTAHS SVYCSILEAL EQGASGVKSG C
 ZntR variant 1: QSMQRS LQRL NDACSGTAHS SVYCSILEAL EQGASGVKSG C

ZntR variant 1 for ZntR_{apo}: *E. coli* ZntR (C115S)- expected mass 16163.5 Da

b

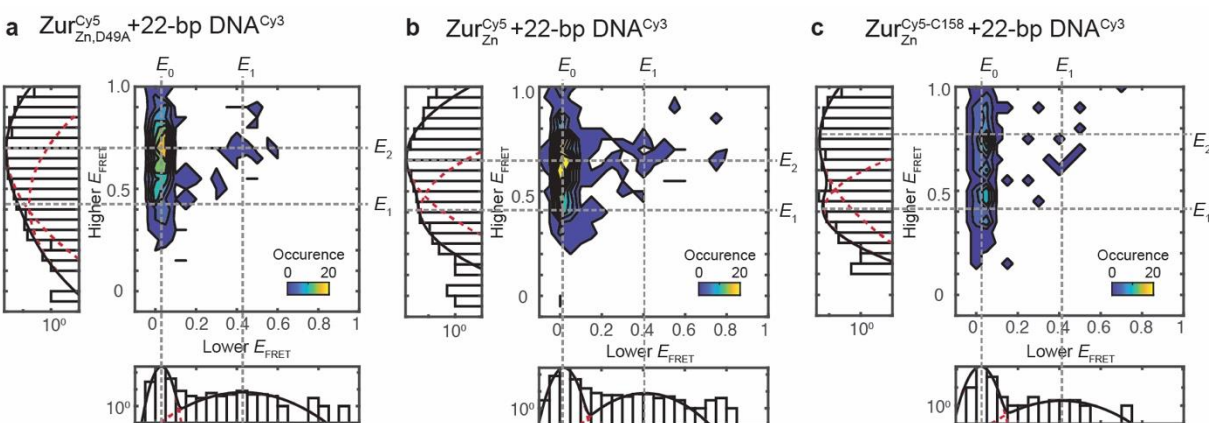
PChe03 (100%), 16,163.5 Da
 HTH-type transcriptional regulator ZntR, *E. coli*, C115S [mutant of P0ACS5 (ZNTR_ECOLI)]
 39 exclusive unique peptides, 90 exclusive unique spectra, 212 total spectra, 127/141 amino acids (90% coverage)

MYRIGELAKM AEVTPDTIRY YEKQQMMEHE VRTEGGFRLY TESDLQRLKF
 IRHARQLGFS LESIRELLSI RIDPEHHTCQ ESKGIVQERL QEVEARIAEL
 QSMQRS LQRL NDACSGTAHS SVYCSILEAL EQGASGVKSG C

Supplementary Fig. 29 | Identity of recombinant ZntR variant is confirmed with mass spectrometry. **a**, Amino-acid sequences of *E. coli* ZntR and our designed variant. The specific mutant residue and expected mass for the variant are written below the sequences. **b**, Amino acid sequence of ZntR variant 1 is determined by LC-MS/MS. The results are visualized via the Scaffold software (Proteome Software). Amino-acids matched to a MS/MS spectrum are highlighted (yellow/green). Amino-acids in green have a post-translational modification. ZntR variant is observed with 90% coverage confirming the C115S mutation circled in red. Source data are provided as a Source Data file.

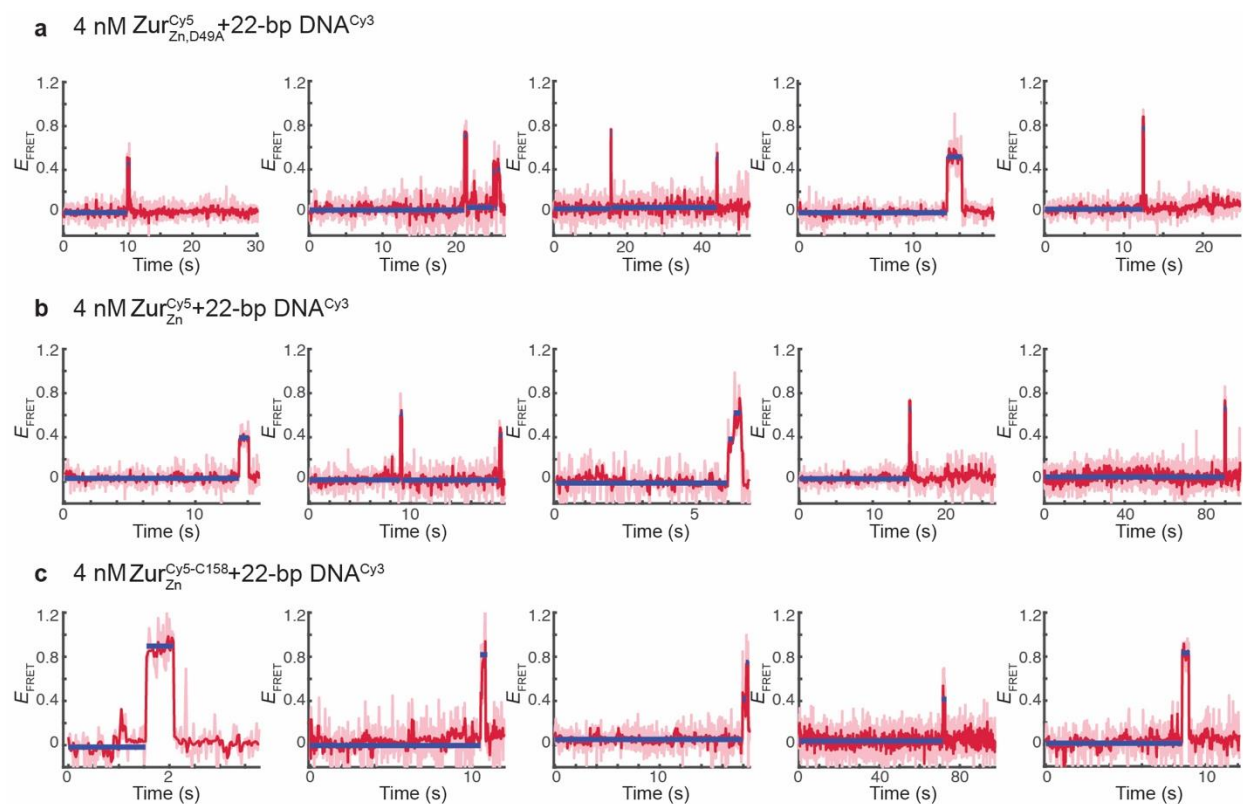
10

15



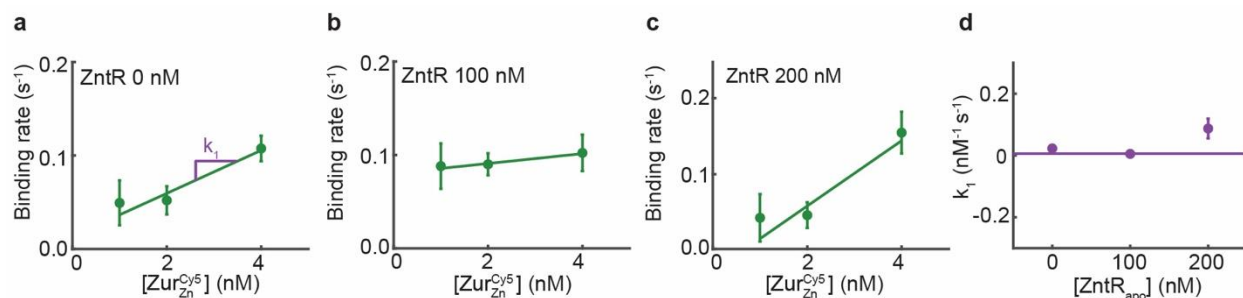
Supplementary Fig. 30 | Two-dimensional histogram of the lower vs. higher E_{FRET} state values from single-molecule E_{FRET} trajectories of an immobilized 22-bp truncated DNA^{Cy3} interacting with 4 nM of **a**, Zur^{Cy5}_{Zn,D49A} (Cy5 at C113), **b**, Zur^{Cy5}_{Zn} (Cy5 at C113), and **c**, Zur^{Cy5-C158}_{Zn}. Left and bottom: corresponding one-dimensional projections. Red dashed lines: Gaussian-resolved fits; black lines: overall fits. Source data are provided as a Source Data file.

20



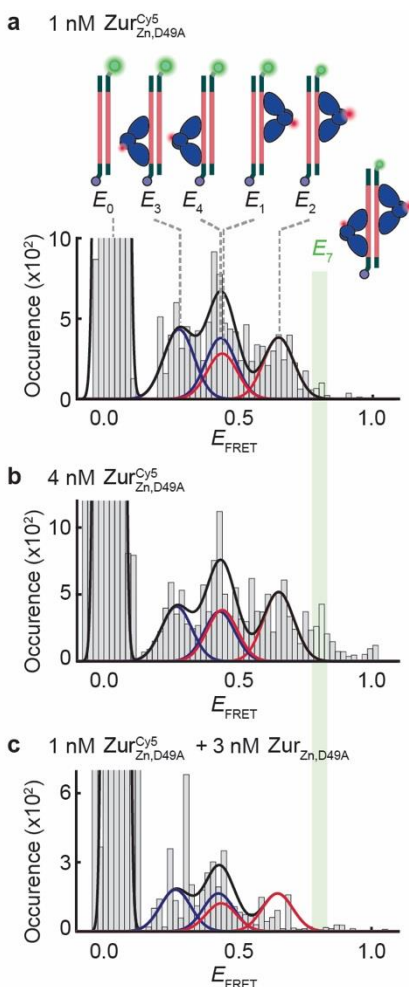
Supplementary Fig. 31 | Examples of single-molecule E_{FRET} trajectories of an immobilized 22-bp truncated DNA^{Cy3} interacting with 4 nM of **a**, $Zur_{Zn,D49A}^{Cy5}$ (Cy5 at C113), **b**, Zur_{Zn}^{Cy5} (Cy5 at C113), and **c**, $Zur_{Zn}^{Cy5-C158}$. Pink lines: raw data; red lines: after non-linear filtering; blue lines: mean value of each E_{FRET} state. Source data are provided as a Source Data file.

5



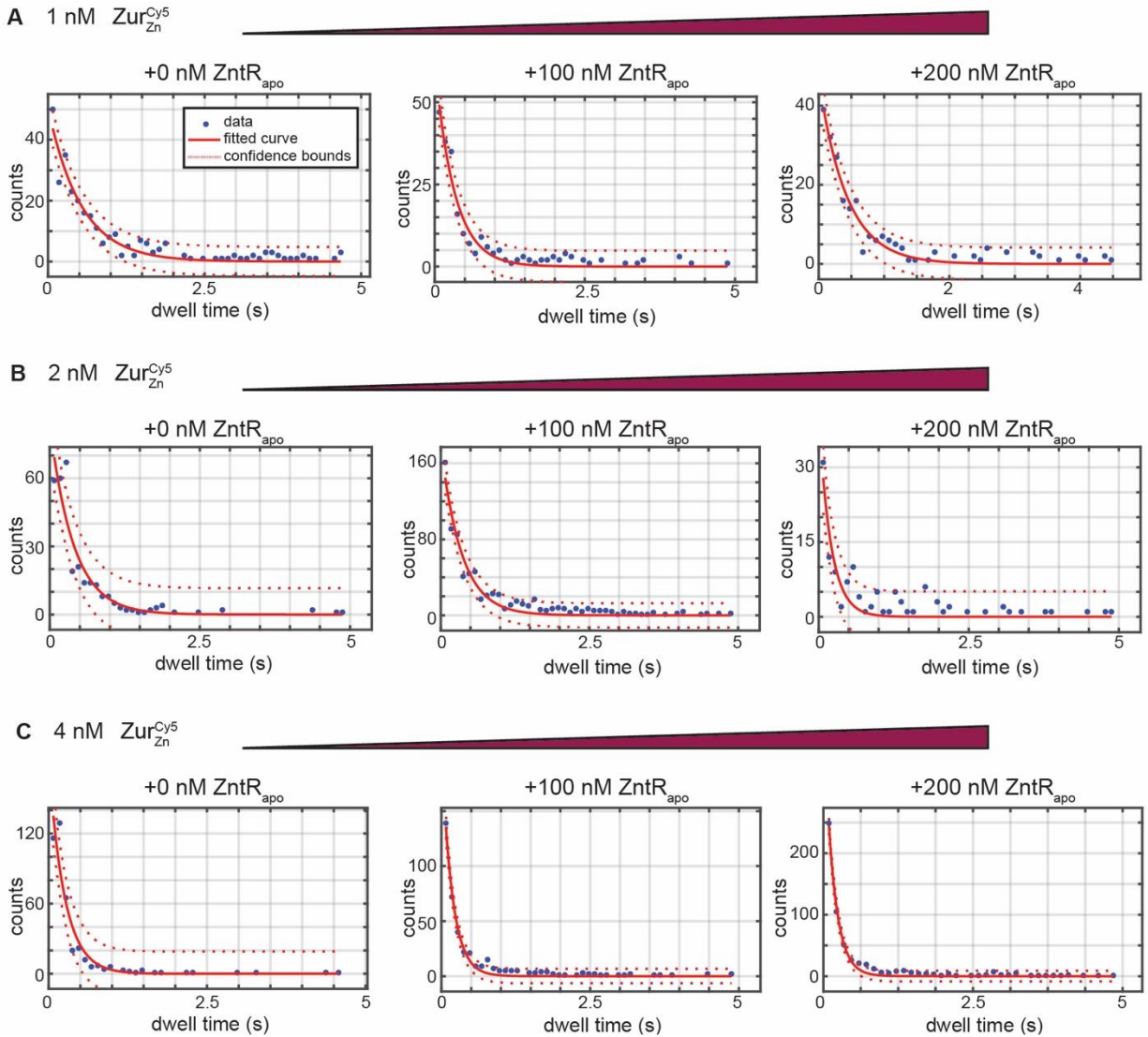
Supplementary Fig. 32 | Binding rate constant of Zur_{Zn}^{Cy5} (Cy5 at C113) on 31-bp DNA^{Cy3} is independent of ZntR_{apo} protein concentration. Binding rate constant (k_1) is the slope of the graph of binding rate vs. $[Zur_{Zn}^{Cy5}]$ in the presence of **a**, 0 nM, **b**, 100 nM, **c**, 200 nM of ZntR_{apo}. Error bars in (a-c) are 90% confidence bounds from exponential decay fitting shown in Supplementary Fig. 35. **d**, $[ZntR_{apo}]$ -independent binding rate constant (k_1) of Zur_{Zn}^{Cy5} . Lines indicate linear fit of each graph. Error bar is standard error of the fitting from (a-c). Source data are provided as a Source Data file.

10



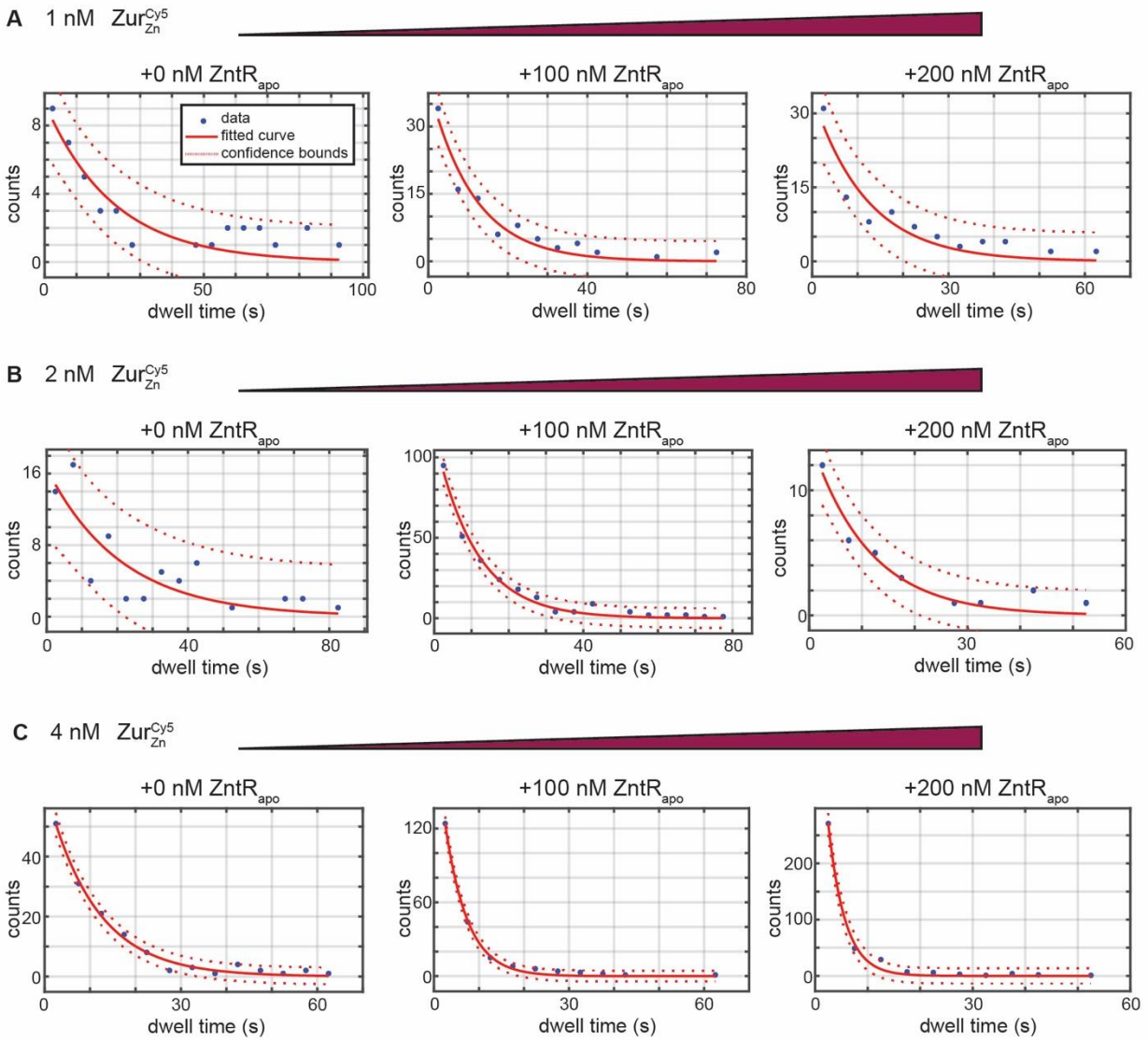
Supplementary Fig. 33 | An E_{FRET} peak for two $\text{Zur}_{\text{Zn,D49A}}^{\text{Cy5}}$ dimers bound to the 31-bp DNA (E_7 at ~ 0.8) disappears when 75% of the 4 nM $\text{Zur}_{\text{Zn,D49A}}^{\text{Cy5}}$ are swapped out to its unlabeled form, supporting that that this E_7 states results from a two-dimer-bound state on DNA.

a, Histogram of E_{FRET} trajectories of immobilized 31-bp DNA^{Cy3} interacting with $\text{Zur}_{\text{Zn,D49A}}^{\text{Cy5}}$ (1 nM). Each color corresponds to a $\text{Zur}_{\text{Zn,D49A}}^{\text{Cy5}}$ dimer at one of the two dyads of Zur binding box in two orientations (Red: E_1 and E_2 states at the proximal dyad site; blue: E_3 and E_4 states at the distal dyad site). Cartoon shows DNA-bound $\text{Zur}_{\text{Zn,D49A}}^{\text{Cy5}}$ at two binding sites in two orientations on DNA. Salt-bridge mutation (D49A) eliminates key inter-dimer interactions. **b**, Same as (a), but with $\text{Zur}_{\text{Zn,D49A}}^{\text{Cy5}}$ at 4 nM. E_7 state is shaded in green, which only appears when two $\text{Zur}_{\text{Zn,D49A}}^{\text{Cy5}}$ dimers are bound to the 31-bp DNA. **c**, Same as (b), but 75% of 4 nM $\text{Zur}_{\text{Zn,D49A}}^{\text{Cy5}}$ is swapped out into its unlabeled form, $\text{Zur}_{\text{Zn,D49A}}$; here the E_7 peak disappeared, supporting it was originally from two $\text{Zur}_{\text{Zn,D49A}}^{\text{Cy5}}$ dimer bound state. (a) and (b) are the same figures as Fig. 4a and b in the main text. Histograms are compiled from 405, 433, 180 E_{FRET} trajectories for (a-c), respectively. Source data are provided as a Source Data file.



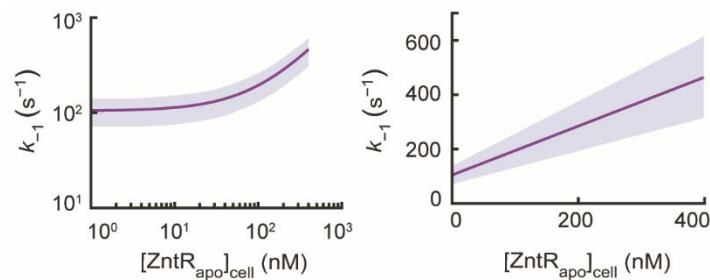
Supplementary Fig. 34 | The distributions of dwell time (i.e., all τ_{bound}) from $\text{Zur}_{\text{Zn}}^{\text{Cys5}}$ (Cy5 at C113) + 31-bp DNA^{Cys3} interactions using *in vitro* smFRET measurement as in Fig. 3b at a protein concentration of **a**, 1 nM, **b**, 2 nM, **c**, 4 nM in the presence of 0-200 nM ZntR_{apo} . The corresponding single exponential fits ($y = A \cdot \exp(-k_{\text{eff}} \cdot \tau)$) are shown in red solid lines. Red dashed lines are 90% confidence bounds. Rate constants are summarized in Supplementary Table 9. All bin sizes: 0.10 s. Distributions are compiled from (a) 287, 222, 212, (b) 314, 724, 118, (c) 404, 393, 564 of dwell times for 0, 100, 200 nm ZntR_{apo} , respectively. Source data are provided as a Source Data file.

5



Supplementary Fig. 35 | The distributions of $\tau_{unbound}$ from Zur_{Zn}^{Cy5} (Cy5 at C113) + 31-bpDNA^{Cy3} interactions using *in vitro* smFRET measurement as in Fig. 3b at a protein concentration of **a**, 1 nM, **b**, 2 nM, **c**, 4 nM in the presence of 0-200 nM $ZntR_{apo}$. The corresponding single exponential fits ($y = A \cdot \exp(-k_{off} \cdot t)$) are shown in red solid lines. Red dashed lines are 90% confidence bounds. Rate constants are summarized in Supplementary Table 9. All bin sizes: 5 s. Distributions are compiled from (a) 40, 95, 89, (b) 69, 26, 31, (c) 140, 208, 373 of dwell times for 0, 100, 200 nM $ZntR_{apo}$, respectively. Source data are provided as a Source Data file.

5



Supplementary Fig. 36 | Solid lines: Simulated dependence of k_{-1} of Zur_{Zn} on [ZntR_{apo}] using the physiological [Zur_{Zn}] = 150 ± 48 nM (average ± s.d.) and across ZntR_{apo}'s physiological concentration range of ~30 to ~400 nM, and using Eq. S43 and the rate constants obtained from *in vitro* FRET measurements (Supplementary Table 9). Colored band: simulated upper/lower bounds using the physiological Zur concentration range. Log-log scale (left) and linear-linear scale (right). Source data are provided as a Source Data file.

5

Supplementary References

1. Kim, J., Webb, A. M., Kershner, J. P., Blaskowski, S. & Copley, S. D. A versatile and highly efficient method for scarless genome editing in *Escherichia coli* and *Salmonella enterica*. *BMC Biotechnol.* **14**, 84 (2014).
- 10 2. Jung, W., Sengupta, K., Wendel, B. M., Helmann, J. D. & Chen, P. Biphasic unbinding of a metalloregulator from DNA for transcription (de)repression in Live Bacteria. *Nucleic Acids Res.* **48**, 2199–2208 (2020).
3. Chen, T.-Y. *et al.* Concentration- and chromosome-organization-dependent regulator unbinding from DNA for transcription regulation in living cells. *Nat. Commun.* **6**, 7445 (2015).
- 15 4. Pédelacq, J. D., Cabantous, S., Tran, T., Terwilliger, T. C. & Waldo, G. S. Engineering and characterization of a superfolder green fluorescent protein. *Nat. Biotechnol.* **24**, 79–88 (2006).
5. Guzman, L. M., Weiss, D. S. & Beckwith, J. Domain-swapping analysis of FtsI, FtsL, and FtsQ, bitopic membrane proteins essential for cell division in *Escherichia coli*. *J. Bacteriol.* **179**, 5094–5103 (1997).
- 20 6. Durisic, N., Laparra-Cuervo, L., Sandoval-Álvarez, Á., Borbely, J. S. & Lakadamyali, M. Single-molecule evaluation of fluorescent protein photoactivation efficiency using an *in vivo* nanotemplate. *Nat. Methods* **11**, 156–162 (2014).
7. Annibale, P., Scarselli, M., Greco, M. & Radenovic, A. Identification of the factors affecting co-localization precision for quantitative multicolor localization microscopy. *Opt. Nanoscopy* **1**, 9 (2012).
- 25 8. Chen, P. & Chen, T.-Y. MATLAB code package: iQPALM (image-based quantitative photo-activated localization microscopy). <https://doi.org/10.6084/m9.figshare.12642617.v1> (2020).
9. Burghard-Schrod, M., Altenburger, S. & Graumann, P. L. The *Bacillus subtilis* dCMP deaminase ComEB acts as a dynamic polar localization factor for ComGA within the competence machinery. *Mol. Microbiol.* **113**, 906–922 (2020).
- 30 10. Cai, L., Friedman, N. & Xie, X. S. Stochastic protein expression in individual cells at the single molecule level. *Nature* **440**, 358–362 (2006).
11. McNabb, D. S., Reed, R. & Marciniak, R. A. Dual luciferase assay system for rapid assessment of gene expression in *Saccharomyces cerevisiae*. *Eukaryot. Cell* **4**, 1539–1549 (2005).
- 35 12. Yu, J., Xiao, J., Ren, X., Lao, K. & Xie, X. S. Probing gene expression in live cells, one protein molecule at a time. *Science* **311**, 1600–1603 (2006).
13. Gilston, B. A. *et al.* Structural and mechanistic basis of zinc regulation across the *E. coli* zur regulon. *PLoS Biol.* **12**, e1001987 (2014).
- 40 14. Shin, J.-H. & Helmann, J. D. Molecular logic of the Zur-regulated zinc deprivation response in *Bacillus subtilis*. *Nat. Commun.* **7**, 12612 (2016).
15. Chandrangsu, P., Huang, X., Gaballa, A. & Helmann, J. D. *Bacillus subtilis* FolE is sustained by the ZagA zinc metallochaperone and the alarmone ZTP under conditions of zinc deficiency. *Mol. Microbiol.* **112**, 751–765 (2019).

16. Gao, W., Zhang, W. & Meldrum, D. R. RT-qPCR based quantitative analysis of gene expression in single bacterial cells. *J. Microbiol. Methods* **85**, 221–227 (2011).
17. Taniguchi, Y. *et al.* Quantifying *E. coli* proteome and transcriptome with single-molecule sensitivity in single cells. *Science* **329**, 533–538 (2010).
- 5 18. Kushner, S. R. mRNA decay in prokaryotes and eukaryotes: different approaches to a similar problem. *IUBMB Life* **56**, 585–594 (2004).
19. Khan, S., Brocklehurst, K. R., Jones, G. W. & Morby, A. P. The functional analysis of directed amino-acid alterations in ZntR from *Escherichia coli*. *Biochem. Biophys. Res. Commun.* **299**, 438–445 (2002).
- 10 20. Outten, C. E., Outten, F. W. & O’Halloran, T. V. DNA distortion mechanism for transcriptional activation by ZntR, a Zn(II)-responsive MerR homologue in *Escherichia coli*. *J. Biol. Chem.* **274**, 37517–37524 (1999).
21. Leliveld, S. R., Zhang, Y. H., Rohn, J. L., Noteborn, M. H. M. & Abrahams, J. P. Apoptin induces tumor-specific apoptosis as a globular multimer. *J. Biol. Chem.* **278**, 9042–9051 (2003).
- 15 22. Roy, R., Hohng, S. & Ha, T. A practical guide to single-molecule FRET. *Nat. Methods* **5**, 507–516 (2008).
23. Joshi, C. P. *et al.* Direct substitution and assisted dissociation pathways for turning off transcription by a MerR-family metalloregulator. *Proc. Natl. Acad. Sci. U. S. A.* **109**, 15121–15126 (2012).
24. Aitken, C. E., Marshall, R. A. & Puglisi, J. D. An oxygen scavenging system for improvement of dye stability in single-molecule fluorescence experiments. *Biophys. J.* **94**, 1826–1835 (2008).
- 20 25. Martell, D. J. *et al.* Metalloregulator CueR biases RNA polymerase’s kinetic sampling of dead-end or open complex to repress or activate transcription. *Proc. Natl. Acad. Sci. U. S. A.* **112**, 13467–13472 (2015).
26. Keller, A. M. *et al.* Dynamic multibody protein interactions suggest versatile pathways for copper trafficking. *J. Am. Chem. Soc.* **134**, 8934–8943 (2012).
27. Chung, S. H. & Kennedy, R. A. Forward-backward non-linear filtering technique for extracting small biological signals from noise. *J. Neurosci. Methods* **40**, 71–86 (1991).
28. Haran, G. Noise reduction in single-molecule fluorescence trajectories of folding proteins. *Chem. Phys.* **307**, 137–145 (2004).
- 30 29. Petrarca, P., Ammendola, S., Pasquali, P. & Battistoni, A. The *zur*-regulated ZinT protein is an auxiliary component of the high-affinity ZnuABC zinc transporter that facilitates metal recruitment during severe zinc shortage. *J. Bacteriol.* **192**, 1553–1564 (2010).
30. Campoy, S. *et al.* Role of the high-affinity zinc uptake *znuABC* system in *Salmonella enterica* serovar Typhimurium virulence. *Infect. Immun.* **70**, 4721–4725 (2002).
- 35 31. Pederick, V. G. *et al.* ZnuA and zinc homeostasis in *Pseudomonas aeruginosa*. *Sci. Rep.* **5**, 13139 (2015).
32. Ducret, V., Gonzalez, M. R., Leoni, S., Valentini, M. & Perron, K. The CzcCBA efflux system requires the CadA p-type ATPase for timely expression upon zinc excess in *Pseudomonas aeruginosa*. *Front. Microbiol.* **11**, 911 (2020).
- 40 33. Brocklehurst, K. R., Megit, S. J. & Morby, A. P. Characterisation of CadR from *Pseudomonas aeruginosa*: a Cd(II)-responsive MerR homologue. *Biochem. Biophys. Res. Commun.* **308**, 234–239 (2003).

34. Moore, C. M. & Helmann, J. D. Metal ion homeostasis in *Bacillus subtilis*. *Curr. Opin. Microbiol.* **8**, 188–195 (2005).
35. Gaballa, A. & Helmann, J. D. Identification of a Zinc-specific metalloregulatory protein, zur, controlling zinc transport operons in *Bacillus subtilis*. *J. Bacteriol.* **180**, 5815–5821 (1998).
- 5 36. Harvie, D. R. *et al.* Predicting metals sensed by ArsR-SmtB repressors: allosteric interference by a non-effector metal. *Mol. Microbiol.* **59**, 1341–1356 (2006).
37. Reyes-Caballero, H. *et al.* The metalloregulatory zinc site in *Streptococcus pneumoniae* AdcR, a zinc-activated MarR family repressor. *J. Mol. Biol.* **403**, 197–216 (2010).
- 10 38. Kloosterman, T. G., Van Der Kooi-Pol, M. M., Bijlsma, J. J. E. & Kuipers, O. P. The novel transcriptional regulator SczA mediates protection against Zn²⁺ stress by activation of the Zn²⁺-resistance gene *czcD* in *Streptococcus pneumoniae*. *Mol. Microbiol.* **65**, 1049–1063 (2007).
39. Baichoo, N. & Helmann, J. D. Recognition of DNA by Fur: a reinterpretation of the fur box consensus sequence. *J. Bacteriol.* **184**, 5826–5832 (2002).
- 15 40. De Pina, K., Desjardin, V., Mandrand-Berthelot, M.-A., Giordano, G. & Wu, L.-F. Isolation and characterization of the *nikR* gene encoding a nickel-responsive regulator in *Escherichia coli*. *J. Bacteriol.* **181**, 670–674 (1999).
41. Blaha, D. *et al.* The *Escherichia coli* metallo-regulator RcnR represses *rcnA* and *rcnR* transcription through binding on a shared operator site: insights into regulatory specificity towards nickel and cobalt. *Biochimie* **93**, 434–439 (2011).
- 20 42. Pinochet-Barros, A. & Helmann, J. D. *Bacillus subtilis* Fur is a transcriptional activator for the PerR-repressed *pfeT* gene, encoding an iron efflux pump. *J. Bacteriol.* **202**, e00697-19 (2020).
43. Zhao, Y. Y. *et al.* Identification of the genetic requirements for zinc tolerance and toxicity in *Saccharomyces cerevisiae*. *G3 Genes, Genomes, Genet.* **10**, 479–488 (2020).
- 25 44. MacDiarmid, C. W., Milanick, M. A. & Eide, D. J. Induction of the ZRC1 metal tolerance gene in zinc-limited yeast confers resistance to zinc shock. *J. Biol. Chem.* **278**, 15065–15072 (2003).
45. Wu, Y. H., Frey, A. G. & Eide, D. J. Transcriptional regulation of the Zrg17 zinc transporter of the yeast secretory pathway. *Biochem. J.* **435**, 259–266 (2011).
46. Ramos-Alonso, L., Romero, A. M., Martínez-Pastor, M. T. & Puig, S. Iron regulatory mechanisms in *Saccharomyces cerevisiae*. *Front. Microbiol.* **11** (2020).
- 30 47. Li, L. & Ward, D. M. Iron toxicity in yeast: transcriptional regulation of the vacuolar iron importer Ccc1. *Curr. Genet.* **64**, 413–416 (2018).
48. Li, L., Bagley, D., Ward, D. M. & Kaplan, J. Yap5 is an iron-responsive transcriptional activator that regulates vacuolar iron storage in yeast. *Mol. Cell. Biol.* **28**, 1326–1337 (2008).
- 35 49. Javer, A. *et al.* Short-time movement of *E. coli* chromosomal loci depends on coordinate and subcellular localization. *Nat. Commun.* **4**, 3003 (2013).
50. English, B. P. *et al.* Single-molecule investigations of the stringent response machinery in living bacterial cells. *Proc. Natl. Acad. Sci. U. S. A.* **108**, E365–E373 (2011).
51. Cunha, S., Woldringh, C. L. & Odijk, T. Restricted diffusion of DNA segments within the isolated *Escherichia coli* nucleoid. *J. Struct. Biol.* **150**, 226–232 (2005).
- 40 52. Mazza, D., Ganguly, S. & McNally, J. G. Monitoring dynamic binding of chromatin proteins in vivo by single-molecule tracking. *Methods Mol. Biol.* **1042**, 117–137 (2013).

53. Mehta, P. *et al.* Dynamics and stoichiometry of a regulated enhancer-binding protein in live *Escherichia coli* cells. *Nat. Commun.* **4**, 1997 (2013).
54. Gebhardt, J. C. M. *et al.* Single-molecule imaging of transcription factor binding to DNA in live mammalian cells. *Nat. Methods* **10**, 421–426 (2013).
- 5 55. Uphoff, S., Reyes-Lamothe, R., De Leon, F. G., Sherratt, D. J. & Kapanidis, A. N. Single-molecule DNA repair in live bacteria. *Proc. Natl. Acad. Sci. U. S. A.* **110**, 8063–8068 (2013).
56. Jiang, W. *et al.* A manganese(IV)/iron(III) cofactor in *Chlamydia trachomatis* ribonucleotide reductase. *Science* **316**, 1188–1191 (2007).
- 10 57. Zhang, M. *et al.* Rational design of true monomeric and bright photoactivatable fluorescent proteins. *Nat. Methods* **9**, 727–729 (2012).
58. Lee, S. H., Shin, J. Y., Lee, A. & Bustamante, C. Counting single photoactivatable fluorescent molecules by photoactivated localization microscopy (PALM). *Proc. Natl. Acad. Sci. U. S. A.* **109**, 17436–17441 (2012).
- 15 59. Outten, C. E. & O’Halloran, T. V. Femtomolar sensitivity of metalloregulatory proteins controlling zinc homeostasis. *Science* **292**, 2488–2492 (2001).
60. Changela, A. *et al.* Molecular basis of metal-ion selectivity and zeptomolar sensitivity by CueR. *Science* **301**, 1383–1387 (2003).
61. Clegg, R. M. [18] Fluorescence resonance energy transfer and nucleic acids. in *Methods in enzymology* vol. **211**, 353–388 (Academic Press, 1992).
- 20 62. Ha, T. *et al.* Initiation and re-initiation of DNA unwinding by the *Escherichia coli* Rep helicase. *Nature* **419**, 638–641 (2002).
63. Sarkar, S. K. *et al.* Engineered holliday junctions as single-molecule reporters for protein–DNA interactions with application to a MerR-family regulator. *J. Am. Chem. Soc.* **129**, 12461–12467 (2007).
- 25 64. Andoy, N. M. *et al.* Single-molecule study of metalloregulator CueR–DNA interactions using engineered holliday junctions. *Biophys. J.* **97**, 844–852 (2009).
65. Schuler, B., Lipman, E. A., Steinbach, P. J., Kulkell, M. & Eaton, W. A. Polyproline and the “spectroscopic ruler” revisited with single-molecule fluorescence. *Proc. Natl. Acad. Sci. U. S. A.* **102**, 2754–2759 (2005).
- 30 66. Sabanayagam, C. R., Eid, J. S. & Meller, A. Using fluorescence resonance energy transfer to measure distances along individual DNA molecules: corrections due to nonideal transfer. *J. Chem. Phys.* **122**, 061103 (2005).
67. Koushik, S. V., Blank, P. S. & Vogel, S. S. Anomalous surplus energy transfer observed with multiple FRET acceptors. *PLoS One* **4**, e8031 (2009).
- 35 68. Hadizadeh, N., Johnson, R. C. & Marko, J. F. Facilitated dissociation of a nucleoid protein from the bacterial chromosome. *J. Bacteriol.* **198**, 1735–1742 (2016).
69. Graham, J. S., Johnson, R. C. & Marko, J. F. Concentration-dependent exchange accelerates turnover of proteins bound to double-stranded DNA. *Nucleic Acids Res.* **39**, 2249–2259 (2011).
- 40 70. Giuntoli, R. D. *et al.* DNA-segment-facilitated dissociation of Fis and NHP6A from DNA detected via single-molecule mechanical response. *J. Mol. Biol.* **427**, 3123–3136 (2015).
71. Loparo, J. J., Kulczyk, A. W., Richardson, C. C. & Van Oijen, A. M. Simultaneous single-molecule

- measurements of phage T7 replisome composition and function reveal the mechanism of polymerase exchange. *Proc. Natl. Acad. Sci. U. S. A.* **108**, 3584–3589 (2011).
72. Geertsema, H. J., Kulczyk, A. W., Richardson, C. C. & van Oijen, A. M. Single-molecule studies of polymerase dynamics and stoichiometry at the bacteriophage T7 replication machinery. *Proc. Natl. Acad. Sci. U. S. A.* **111**, 4073–4078 (2014).
- 5 73. Ma, C. J., Gibb, B., Kwon, Y., Sung, P. & Greene, E. C. Protein dynamics of human RPA and RAD51 on ssDNA during assembly and disassembly of the RAD51 filament. *Nucleic Acids Res.* **45**, 749–761 (2017).
- 10 74. Lee, J. Y., Finkelstein, I. J., Crozat, E., Sherratt, D. J. & Greene, E. C. Single-molecule imaging of DNA curtains reveals mechanisms of KOPS sequence targeting by the DNA translocase FtsK. *Proc. Natl. Acad. Sci. U. S. A.* **109**, 6531–6536 (2012).
75. Gibb, B. *et al.* Concentration-dependent exchange of replication protein α on single-stranded DNA revealed by single-molecule imaging. *PLoS One* **9**, e87922 (2014).
- 15 76. Chen, T. Y., Cheng, Y. S., Huang, P. S. & Chen, P. Facilitated unbinding via multivalency-enabled ternary complexes: new paradigm for protein-DNA interactions. *Acc. Chem. Res.* **51**, 860–868 (2018).
77. Kamar, R. I. *et al.* Facilitated dissociation of transcription factors from single DNA binding sites. *Proc. Natl. Acad. Sci. U. S. A.* **114**, E3251–E3257 (2017).
- 20 78. Erbaş, A. & Marko, J. F. How do DNA-bound proteins leave their binding sites? The role of facilitated dissociation. *Curr. Opin. Chem. Biol.* **53**, 118–124 (2019).
79. Robinson, A. & van Oijen, A. M. Bacterial replication, transcription and translation: mechanistic insights from single-molecule biochemical studies. *Nat. Rev. Microbiol.* **11**, 303–315 (2013).
80. Spinks, R. R. *et al.* DnaB helicase dynamics in bacterial DNA replication resolved by single-molecule studies. *Nucleic Acids Res.* **49**, 6804–6816 (2021).
- 25 81. Wilkinson, E. M., Spenkelink, L. M. & van Oijen, A. M. Observing protein dynamics during DNA-lesion bypass by the replisome. *Front. Mol. Biosci.* **9** (2022).
82. Kong, M. & Greene, E. C. Mechanistic insights from single-molecule studies of repair of double strand breaks. *Front. Cell Dev. Biol.* **9** (2021).
- 30 83. Koşar, Z., Attar, A. G. & Erbaş, A. Facilitated dissociation of nucleoid-associated proteins from DNA in the bacterial confinement. *Biophys. J.* **121**, 1119–1133 (2022).
84. Duzdevich, D., Redding, S. & Greene, E. C. DNA dynamics and single-molecule biology. *Chem. Rev.* **114**, 3072–3086 (2014).
85. Kaniecki, K., De Tullio, L. & Greene, E. C. A change of view: homologous recombination at single-molecule resolution. *Nat. Rev. Genet.* **19**, 191–207 (2018).
- 35 86. Heidarsson, P. O. *et al.* Release of linker histone from the nucleosome driven by polyelectrolyte competition with a disordered protein. *Nat. Chem.* **14**, 224–231 (2022).
87. Bergqvist, S. *et al.* Kinetic enhancement of NF- κ B-DNA dissociation by I κ B α . *Proc. Natl. Acad. Sci. U.S.A.* **106**, 19328–19333 (2009).
- 40 88. Chen, W., Lu, W., Wolynes, P. G. & Komives, E. A. Single-molecule conformational dynamics of a transcription factor reveals a continuum of binding modes controlling association and dissociation. *Nucleic Acids Res.* **49**, 11211–11223 (2021).

89. Tsai, M.-Y., Zhang, B., Zheng, W. & Wolynes, P. G. Molecular mechanism of facilitated dissociation of Fis protein from DNA. *J. Am. Chem. Soc.* **138**, 13497–13500 (2016).
90. Chen, C. & Bundschuh, R. Quantitative models for accelerated protein dissociation from nucleosomal DNA. *Nucleic Acids Res.* **42**, 9753–9760 (2014).
- 5 91. Dahlke, K. & Sing, C. E. Facilitated dissociation kinetics of dimeric nucleoid-associated proteins follow a universal curve. *Biophys. J.* **112**, 543–551 (2017).
92. Paramanathan, T., Reeves, D., Friedman, L. J., Kondev, J. & Gelles, J. A general mechanism for competitor-induced dissociation of molecular complexes. *Nat. Commun.* **5**, 5207 (2014).

10